LBL-13863

LBL--13863

DE82 018519

LIGHT-PARTICLE EMISSION AS A PROBE OF THE ROTATIONAL DEGREES OF FREEDOM IN DEEP-INELASTIC REACTIONS

Lee G. Sobotka

Nuclear Science Division
Lawrence Berkeley Laboratory
University of California
Berkeley, CA 94720

DISTRIBUTION OF THIS DOCUMENT IS UNLIMITED

LIGHT PARTICLE EMISSION AS A PROBE OF THE ROTATIONAL DEGREES OF FREEDOM IN DEEP-INELASTIC REACTIONS

Table of Contents

LIGHT PARTICLE EMISSION AS A PROBE OF THE ROTATIONAL
DEGREES OF FREEDOM IN DEEP-INELASTIC REACTIONS

Lee Gordon Sobotka

Nuclear Science Division
Lawrence Berkeley Laboratory
University of California
Berkeley, CA 94720

Abstract

The emission of alpha particles in coincidence with the most deeply inelastic heavy-ion reactions has been studied for ^{181}Ta + ^{165}Ho at 1354 MeV laboratory energy and ^{nat}Ag + ^{84}Kr at 664 MeV. Alpha particle energy spectra and angular distributions, in coincidence with a projectile-like fragment, were acquired both in the reaction plane and out of the reaction plane at a fixed in-plane angle.

The in-plane data for both systems are employed to show that the bulk of the alpha particles in coincidence with the deep-inelastic exit channel can be explained by evaporation from the fully accelerated fragments. Average velocity diagrams, α-particle energy spectra as a function of angle in several rest frames, and α-particle angular distributions are presented.

The out-of-plane alpha particle angular distributions and the gamma-ray multiplicities are used to study the transfer and partitioning of angular momentum between the two fragments. For the ^{nat}Ag + ^{84}Kr system, individual fragment spins are extracted from the alpha particle angular distributions as a function of mass asymmetry while the sum of the fragment spins is derived from the gamma-ray

multiplicities. These data, together with the fragment kinetic energies, are consistent with rigid rotation of an intermediate complex consisting of two substantially deformed spheroids in near proximity. These data also indicate that some angular momentum fractionation exists at the largest asymmetries examined. Out-of-plane alpha particle distributions, gamma-ray multiplicities, fragment spins as well as the formalism for the spin evaluation at various levels of sophistication are presented.

I. INTRODUCTION

A. Background

Shortly after the advent of heavy-ion accelerators deeply in-
elastic reactions between heavy ions were discovered. These reactions
have properties intermediate between the well-studied limits of direct
reactions, which involve only a few nucleons and thus relatively few
single particle degrees of freedom, and compound nucleus reactions,
which result in the involvement of all the nucleons and their associ-
ated degrees of freedom. The exit channel of this new reaction mech-
anism is binary with the masses of the two fragments reminiscent of
the entrance channel masses. There is, however, substantial transfer
of energy, mass, and angular momentum between the two heavy ions. In
contrast with compound nucleus reactions, the degrees of freedom asso-
ciated with these transfers are not always totally equilibrated. In
fact, the degree of equilibration can to some extent be controlled by
the reaction parameters (such as the bombarding energy and entrance
channel mass asymmetry). Thus, these reactions provide a vehicle for
studying the relaxation processes. The study of these processes
provides information on the relevant degrees of freedom, which can in-
clude, in addition to nucleonic degrees of freedom, collective effects
such as nuclear shape changes. The brightest light at the end of the
tunnel of "deep inelastic studies" is then an improved understanding
of collective effects in nuclei. It is my hope and intent that this
thesis provides a small step in this direction.

B.   Deep Inelastic Reactions

To provide a background for this thesis a short summary of some of the experimental results concerning the relaxation of the collective degrees of freedom is presented here. (For a comprehensive report, several excellent reviews are available [Mo 76, Sc 77, Le 78, Mo 81c].) These degrees of freedom do not lend themselves to simple and differentiable definitions, but they can be grossly labeled as 1) the relative motion between the two heavy ions, 2) the fragment neutron-to-proton ratio, 3) angular momentum degrees of freedom, and 4) the mass asymmetry.

The relaxation of the first of these modes is quite obvious when studying HI reactions because the manifestation of this relaxation is a dramatic reduction in the relative velocity of the fragments. The reactions that lead to this dramatic reduction of relative velocity are now commonly called deep inelastic (DI) reactions and are typified by fragment kinetic energies close to the values expected from the repulsion of two charged spheroids, as is the case in fission. In truth, the asymptotic kinetic energies are influenced by several degrees of freedom, such as the fragment separation distance, angular momentum, neck, and fragment deformation degrees of freedom. To date, no clear picture of the behavior of these individual modes has been developed.

The relaxation time of the neutron-to-proton ratio is perhaps the shortest of the collective degrees of freedom mentioned above. Beautiful experimental studies [Ga 75, Ga 76, Le 78, Kr 80] have shown

that the N/Z ratio equilibrates during the very early stages of energy dissipation, perhaps even before any net mass transfer has occurred between the fragments.

The relaxation time of the angular momentum degrees of freedom is also relatively short, as compared to that of the mass asymmetry mode, and probably quite similar to the relaxation time of the relative motion. Similar relaxation times are expected since the angular momentum relaxation time depends upon the loss of tangential velocity (and thus upon the tangential component of the frictional force) while the relaxation time of the relative motion degree of freedom depends upon the loss of both the tangential and radial velocities (thus upon both components of the frictional force). However, it is not clear whether this relaxation time is always shorter than the interaction time in a DI reaction. Gamma-ray multiplicity (M_γ) studies of reactions induced by light heavy ions ($A \leq 40$) indicate that the equilibrium limit of rigid rotation of the dinuclear system has been reached [G1 77, Na 79]. For heavier projectiles, such as Kr, M_γ data do not provide direct evidence for rigid rotation [Al 78]. It has been suggested that rigid rotation is achieved but that the expected trend of M_γ with mass asymmetry is masked by an ℓ-wave fractionation with exit channel mass asymmetry [Al 78, Re 78].

The mass asymmetry degree of freedom has a relaxation time longer than the other modes mentioned above, as well as the interaction time for a DI reaction. The exit channel mass distributions are generally peaked around the entrance channel values [for example, Sc 77] rather

than the equilibrium values (which depend upon ℓ-wave and the total mass of the system but are generally at symmetry).

C. The Use of Light Particles

At energies of only a few MeV/nucleon above the interaction barrier, evaporation is the dominant mechanism for the production of light particles (LPs are commonly n, p, t, or α-particles). The energy spectra and angular distributions of these LPs contain information on the temperature (T) and spin (I) of the emitting nucleus. Thus insight into the thermal properties and angular momentum degrees of freedom can, and has been, obtained by studying the light particle emission associated with DI reactions.

Two excellent examples of the use of LPs for these purposes are the studies of Eyal et al. [Ey 78] and Babinet et al. [Ba 80]. In the former study [Ey 78] neutron emission in the reaction $^{166}Er + ^{86}Kr$ at 7.0 MeV/nucleon was measured for the DI component of the reaction. This study concludes that the equilibration of the excitation energy between the two exit channel nuclei occurs during the lifetime of the intermediate complex. This conclusion is supported by two experimental observations. The first of these is that the mean number of evaporated particles from the two reaction products indicates that the partition of the total dissipated energy between the two fragments is in proportion to their masses. Such a partition is required by the thermal equilibrium condition [Mo 81b]. The second experimental observation is that the temperatures of the two fragments (deduced from the neutron energy spectra) are the same, within the experimental uncertainties.

Detailed studies of the neutron emission from the systems ^{165}Ho + ^{56}Fe at 8.5 MeV/amu [Hi 79] and ^{197}Au + ^{63}Cu at 5.8 MeV/amu [Pe 77] reached the same conclusion.

In the second example [Ba 80], in- and out-of-plane α-particle angular distributions were measured for the DI component of the reaction ^{58}Ni + ^{40}Ar at 7.0 MeV/amu. In this study the out-of-plane α-particle emission from the target-like recoil nucleus was isolated by careful selection of the angle of the HI detector as well as the in-plane angle for the out-of-plane α-particle detectors. Individual fragment spins were extracted from the out-of-plane distributions as a function of mass asymmetry. The trend of these spins with mass asymmetry agreed with the rigid rotation predictions. This confirmed the conclusion of earlier M_γ work [Gl 77, Na 79] on similar systems that the rotational degrees of freedom equilibrate during the lifetime of the DI complex.

The studies mentioned above rely on the identification of the source of the LPs. Most studies, including the ones mentioned above, have concluded that the fully accelerated fragments are the sources of the LPs. This agrees with statistical model calculations that predict that the LP evaporation times are substantially longer than the heavy-ion interaction time, [Hi 79]. However, recent data on ^{40}Ar and ^{56}Fe induced reactions [Lo 80a, Lo 80b, Gu 81] indicate that under certain conditions, LP evaporation prior to scission of the intermediate complex can be substantial. The prescission LP emission process not only presents the tantalizing possibility of studying the

intermediate complex during its very short lifetime, but also provides information on the conditions required for prescission emission. This information could be used to test, and perhaps improve, statistical model calculations.

II. SCOPE OF THE PRESENT STUDY

A. $181_{Ta} + 165_{Ho}$

While no HI inclusive work for this system has been reported in
the literature, the systematics of DI HI reactions are sufficiently
well mapped out by previous inclusive work so that reliable predic-
tions can be made for the Ta + Ho system. The parameters that are
useful to compare this system to those previously studied are given in
Table 1.

The small value of the ratio $E_{c.m.}/B_{coul}$ ($E_{c.m.}$ is the bombarding
energy in the center of mass system and B_{coul} is the Coulomb barrier)
indicates that the interaction is strongly influenced by the Coulomb
potential and thus is peripheral and gentle. For such heavy systems
(total charge $Z_t = 138$) the evaporation residue cross section (σ_{ER}) is
expected to be zero and the fusion fission component is expected to be
small due to the gentle nature of the collision. (For such gentle
collisions one does not expect this intermediate complex to reach the
compact saddle shape of the compound nucleus.)

Other than the work reported in this thesis no LP studies on
systems as heavy as $181_{Ta} + 165_{Ho}$ have been done. However, such work
is interesting for several reasons. This system is heavier, has more
angular momentum, and probably has a larger intermediate complex than
any of the systems previously studied by LP techniques. Furthermore,
the reaction is simple because it is dominated by a single process
(DI). Because of these qualities the Ta + Ho system has the potential
for providing important information on the conditions needed for

prescission emission. The data relevant to the question of the emission source(s) is presented in Chapter V and discussed in Chapter VIII.

The α-particle data from the ^{181}Ta + ^{165}Ho system are used in this thesis to confirm results concerning the angular momentum degrees of freedom obtained from previous M_γ and γ-ray anisotropy work. A detailed study [McD 82] of γ-rays emitted in the DI reaction ^{165}Ho + ^{165}Ho at 8.5 MeV/amu provided evidence that the angular momentum degrees of freedom were equilibrated. Since the systems are similar, the out-of-plane α-particle data should be consistent with the results of the M_γ study. The measured α-particle out-of-plane distribution is presented in Chapter VI, and its consistency with the results of the γ-ray study is discussed in Chapter VIII.

B. $\underline{\text{nat}_{Ag} + {}^{84}\text{Kr}}$

Inclusive studies of the ^{nat}Ag + ^{84}Kr system have been performed at several bombarding energies by Schmitt et al. [Sc 78a, Sc 78b]. These studies found a pronounced relaxed component for all charge asymmetries. The charge distribution for the most relaxed events was very broad and appeared to peak at symmetry rather than at the entrance channel asymmetry. This slight drift toward symmetry (the entrance channel is near symmetry, see Table 2) can be interpreted as the DI complex diffusing along the mass asymmetry coordinate rather than evidence for a strong fusion-fission component. This interpretation is supported by the fact that the angular distributions for all asymmetries were forward peaked in excess of 1/sinθ (which would not be the case if the binary exit channel was the result of ordinary

fission.) Although no clear evidence for the relaxation of the mass asymmetry degree of freedom can be obtained for a system where the entrance channel is so close to symmetry, the inclusive Ag + Kr studies provide evidence for the relaxation of the relative motion degree of freedom.

As mentioned earlier, M_γ data for the $^{nat}Ag + ^{84}Kr$ system does not provide direct evidence for the relaxation of the angular momentum degrees of freedom. The explanation for this most likely rests on the fact that both the rolling limit and the rigid rotation limit (even with a constant ℓ-window) predict a weak dependence of the sum of the fragment spins on mass asymmetry near symmetry. Therefore, M_γ, which measures the sum of the spins, is a poor technique to address the question of whether rigid rotation is reached for systems where the experimentally accessible exit channels are near symmetry. In addition, the small difference between the predictions of the sum of the spins with mass asymmetry of rolling and rigid rotation, can be reduced by the ℓ-wave fractionation effect mentioned in Chapter I. Fortunately, the α-particle technique measures the spin of an individual fragment. For this quantity the rigid rotation limit, unlike rolling, predicts a strong dependence on mass asymmetry even at symmetry.

After demonstrating that α-particles emitted from the target-like fragment have been isolated (Chapter V), the out-of-plane distributions and spins extracted from these distributions as a function of mass asymmetry are presented in Chapter VI. Chapter VII compares these spins to various calculations and Chapter VIII contains a discussion concerning the relaxation of the angular momentum degrees of freedom.

III. EXPERIMENTAL

A. Design Goals

In order to accomplish the objectives outlined in the previous chapter, the two body kinematics must be determined for the deep-inelastic events. The experiments themselves were not kinematically complete; however, with the aid of assumptions that have been verified in previous experiments, the kinematics was reconstructed. (A detailed description of these assumptions will be presented in the next chapter.)

One of the heavy ion reaction products was detected near the classical grazing angle. This angle was chosen to maximize the ratio of the DI yield to the total reaction cross section, under the constraint of retaining a counting rate sufficient to perform the desired coincidence measurements. The beam direction and the direction of the detected heavy ion served to define a reaction plane for the two body kinematics.

The choice of α-particles as the light particle to be detected was motivated by two reasons. First, the amount of spin removed and spin information carried by the evaporated particle increases with its mass. Thus α-particles are substantially better than protons or neutrons in this regard. Evaporation of heavier particles is strongly suppressed due to the large Coulomb barriers for emission. For example, lithium ions were found to be suppressed by over a factor of ~400 relative to helium ions in the $^{181}Ta + ^{165}Ho$ experiment. The second reason is simply that the detection and identification of α-particles in the experimental energy range is an easy task using

ΔE-E solid state telescopes. The dimensions of the elements of these telescopes are such that the detectors are readily available and quite reliable.

If the only requirement of the experiment was to determine the spin of one fragment, then the tool with the greatest sensitivity would be sequential fission. This method of spin determination has been employed quite successfully by several groups [Wo 78, Ba 78, Pu 79, Dy 79, Ha 79, Ra 79, Le 81, Mo 82]. However, if information concerning the partitioning of angular momentum between the two exit channel nuclei is desired, then sequential fission is no longer the preferred probe. The reason for this is as follows. In order to determine the spin partition one needs the direct determination of either both of the spins or one of the spins and the sum of the spins. The former possibility presents a host of experimental complications, and though this method has been attempted, no results have appeared in the literature. The latter method can be accomplished by obtaining the sum of the spins from γ-ray multiplicity data, as is frequently done [Al 75, Le 79, Gl 77, Al 78, Ol 78, Ge 79, Na 79]. Unfortunately, if sequential fission occurs with a sufficiently high probability to make extraction of an individual spin experimentally feasible, then the relation between M_γ and the sum of the spins of the primary fragments is greatly obscured by the substantial amount of the intrinsic spin of the fissioning nucleus which is converted into orbital angular momentum of the fission fragments. This difficulty can be substantially reduced by employing the sequential emission of

light particles as the probe of the spin of one of the DI fragments.
Light particle emission generally converts a much smaller fraction of
the fragment's intrinsic spin into orbital angular momentum than does
sequential fission and thus the difficulties of relating γ-ray multi-
plicity data to the total spin are similarly reduced.

Before such spin studies can be undertaken, the emission source
of the α-particles must be determined by studying the correlation be-
tween heavy ions and α-particles in the reaction plane, see Fig. III.1.
For each of the systems coincidence α-particle energy spectra were
obtained over a broad range of angles.

The measured in-plane α-particle correlation can be used to locate
a region where the α-particles are predominantly due to evaporation
from a single source. The coincident out-of-plane α-particle distri-
butions were obtained at an in-plane angle in this region. From these
distributions the spin of the emitting nucleus was determined. In
choosing the in-plane angle for the out-of-plane measurements one must
take into account the transformation from the lab system (see Fig.
III.2) into the rest frame of the emitter (which for our studies was
the target recoil).

In Fig. III.3 contours of equal in- and out-of-plane angles in the
rest frame of the emitter (respectively, ϕ_{RF} and θ_{RF}) are plotted
as a function of the in- and out-of-plane lab angles (respectively,
ϕ_L and θ_L). This plot shows that a fixed in-plane angle of, say,
$\phi_L = 60°$, corresponds to an in-plane angle of about 90° from the
recoil in the rest frame. However, as one moves to an out-of-plane

lab angle of $\theta_L = 60°$, at the same in-plane angle ($\phi_L = 60°$), the in-plane angle in the recoil frame becomes $\phi_{RF} \sim 130°$. Also, observation of out-of-plane angles greater than 60° in the frame of the recoil are kinematically forbidden at an in-plane lab angle of 60°. If the in-plane distribution of alpha particles has a dependence on ϕ_{RF}, then the out-of-plane distributions at fixed ϕ_L (when ϕ_L is not equal to the recoil direction) could be quite complicated due to the mixture of many ϕ_{RF} angles. On the other hand, if there is no dependence on ϕ_{RF}, then all out-of-plane distributions would be identical except that the maximum accessible out-of-plane angle in the rest frame (θ_{RF}) measurable at fixed ϕ_L decreases as ϕ_L increases.

As will be shown in Chapter V, the α-particle spectra at angles equal to or larger than the target recoil direction showed no features that could not be attributed to evaporation from the target-like fragment. This fact, along with the considerations stated above, led us to choose the target recoil direction as the in-plane angle at which to obtain the out-of-plane α-particle distributions.

B. Beam, Target, and Detection Hardware

The ^{165}Ho and ^{84}Kr beams were obtained from the Lawrence Berkeley Laboratory SuperHILAC. Both in- and out-of-plane measurements were completed in one experimental run for the ^{165}Ho + ^{181}Ta system. However, the ^{84}Kr + ^{nat}Ag study required two runs, one for the in-plane and the other for the out-of-plane measurements.

The ^{181}Ta target was rolled to a thickness of 1.4 mg/cm^2, as determined by weight. The ^{nat}Ag targets were produced by evaporation

with thicknesses of 0.97 mg/cm^2 and 0.59 mg/cm^2 for the in- and out-of-plane runs, respectively. These targets were positioned by a holder that could rotate about two perpendicular axes, thus allowing a choice of target angle and tilt to minimize the energy loss of α-particles and heavy ions in the target.

The detection apparatus is schematically depicted in Fig. III.4. The three major components are the heavy ion detector(s), the α-particle telescopes, and the array of NaI scintillators used for the M_γ determination. For the ^{165}Ho + ^{181}Ta system, the projectile-like fragment was detected at 29° in a partially depleted 300 μm detector (Ortec, type A-023-150-300). This detector provides the angle (ϕ_Z) and energy of one of the two major fragments. The charge or mass of this fragment was not determined. A gas ionization ΔE-E telescope [Fo 74], for the in-plane run, and a solid state telescope (11.7 μm, 300 μm), for the out-of-plane run, were used in the ^{84}Kr + ^{nat}Ag experiments to detect the projectile-like fragment. These telescopes, placed at 26°, provided the angle (ϕ_Z), energy, and charge (Z) of the projectile-like fragment. Though the gas telescope provided superior Z resolution, a price was paid in reduced solid angle. These angles were 4.8 msr and 6.8 msr (corresponding to acceptance angles of ±2.2° and ±2.7°) for the gas and solid state telescopes, respectively.

On the opposite side of the beam (see Fig. III.4), an arc with both in- and out-of-plane arms was used to mount up to five light particle (LP) solid state ΔE-E telescopes (40 μm-5mm). The arc was

attached to a thin-walled domed lid, which, when placed on the scattering chamber, seated the foot of the arc into a cradle on an externally movable arm.

The arc was positioned with a transit and the error in the angle of any LP telescope was estimated to be no more than $0.5°$. These telescopes provided the angles (ϕ_L, θ_L), energy, and the atomic number of the light particles. The angles at which concidence data were obtained are listed in Tables 3 and 4 for the $^{181}Ta + ^{165}Ho$ and $^{nat}Ag + Kr$ experiments, respectively.

Outside of the scattering chamber, an array consisting or seven or eight 7.6 x 7.6 cm NaI detectors was utilized to measure the γ-ray multiplicity. These detectors were positioned above the reaction plane at an out-of-plane angle of $45°$ and at a distance of 23 cm from the target. This distance was sufficient to separate neutrons from γ rays by their time of flight [Ri 80]. These detectors were collimated down to a front face diameter of 5.0 cm with lead shielding. In the out-of-plane ^{84}Kr run, an additional NaI with a reduced solid angle was used to obtain the γ-ray energy spectrum.

C. Calibration

The beam energy was measured at regular time intervals during all the experiments. These measurements were made either with a calibrated solid-state detector and then applying a pulse height defect (PHD) correction [Mo 78b] or by use of a phase probe, which measures the beam velocity. The beam energies, were 664 ± 8 MeV for the ^{84}Kr beam and 1387 ± 15 MeV for the ^{165}Ho beam. The mean

interaction energies, calculated at the center of the target, are 650
MeV and 1354 MeV for the ^{84}Kr and ^{165}Ho beams, respectively.

All stopping E detectors and the associated electronics were
calibrated with a tail pulser, which had been absolutely calibrated
with a ^{212}Pb α-particle source. These calibrations were in close
agreement with elastic scattering measurements. For the ^{165}Ho run
elastic scattering measurements were performed at four bombarding
energies on a thin (0.525 mg) ^{197}Au target. By successively drop-
ping accelerating tanks, elastic scattering measurements at each ener-
gy yielded four energy calibration points, (beam energies of 8.5, 7.2,
5.9 and 4.6 MeV/amV corresponding to 8, 7, 6, and 5 tanks, respective-
ly) over a range of several hundred MeV.

For the Kr runs the HI ΔE detectors and electronics were
calibrated by determining the energy lost in these detectors by
elastically scattered heavy ions. This was done by measuring the
energy deposited in the E detector with and without the ΔE detector
present. The calibration for the solid state ΔE used for the out-
of-plane Kr run was checked with a calibrated pulser.

The energy calibration for both elements of all the LP detectors
were obtained by use of a calibrated tail pulser. The solid angles of
these telescopes were measured with a ^{241}Am source of known activity
and the relative efficiencies were checked with a ^{212}Pb source. The
measured solid angles agreed to within ±3% of the geometric solid
angle. These solid angles are reported in Tables 3 and 4.

Absorbers ranging from 10.1 mg/cm^2 Ta to 1 mg/cm^2 Au were
placed in front of the LP telescopes to reduce the rates of heavy

ions, X rays, and low energy electrons striking these counters (see Tables 3 and 4). The absorber thicknesses were determined either by α-particle energy loss measurements or by weight. The detection threshold for α-particles was approximately 10 MeV, primarily due to the thickness of the first element of the telescope rather than to the absorbers.

The detection efficiency of each of the 7.6 cm x 7.6 cm NaI detectors was determined by γ-γ techniques. The efficiency at 570 keV was determined using the decay of ^{207}Bi (EC $\rightarrow$ 1063 KeV γ $\rightarrow$ 570 keV γ $\rightarrow$ G.S. ^{207}Pb) while the decay of ^{60}Co was used to determine the efficiency at 1173 keV (β- $\rightarrow$ 1173 keV γ $\rightarrow$ 1332 keV γ $\rightarrow$ G.S. ^{60}Ni).

The time-to-amplitude converters (TACs) between the heavy ion and α-particle channels and the heavy ion and γ-ray channels (see section D of this chapter) were calibrated from the SuperHILAC beam micro-structure (RF frequency 70 MHz) or by use of an Ortec 462 time calibrator.

D. Electronics and Logic

The logic necessary to select the desired information from the signals produced by the various elements (19 or 20 separate detectors are involved) is outlined in Figs. III 5, 6 and 7. The high level logic, which shows the relationships between the various sets of detectors (i.e., the HI, LP and γ-ray detectors), is shown in Fig. III.5. Lower level logic for the ΔE-E telescopes (for HI or LP detection) and the NaI Halo (for γ-ray detection) are shown in Fig. III.5 and 6, respectively. All electronic modules required to execute this logic scheme were NIM standard.

As can be seen from Fig. III.5 double (Z, LP), triple, higher order (Z, LP, X_γ) coincidence events, as well as scaled down Z and LP events created a Master Gate. This gate allowed the individual parameters of the event, if they passed their respective gates (see Fig. III.5), to be digitized by a multiplexer, ADC system developed at LBL. These events were then recorded on magnetic tape in an event-by-event format by a Modcomp IV computer. The off-line treatment of this data is the subject of the next chapter.

IV. DATA ANALYSIS

A. General Method

The earlier Kr experiments were analyzed on a PDP-15 computer, while the later Ho experiment was analyzed on a Modcomp IV computer. The codes required for the complete analysis of these data were developed on both machines; however, the logic and definition of each step in the analysis process reached a higher level in the later Modcomp scheme, which is shown in Fig. IV.1. The only substantive difference between the analyses of the ^{84}Kr and ^{165}Ho and experiments involved the identification of the atomic number of the detected HI for the former case.

Figure IV.1 shows the logic employed in the analysis of both types of singles data as well as of the coincidence data. Each arrow corresponds to a program designed to take the data, in the form described in the box above the arrow, and make an event-by-event transformation into the form given in the box below the arrow. As can be seen from this flow chart, the event-by-event nature of the data is retained throughout. This procedure allows one to ferret out failures in specific elements of our experimental apparatus that occurred in the course of the experiments and thus to eliminate the data or apply appropriate corrections. In addition, errors due to coding or logic can be easily found and corrected.

B. Specifics

1) Charge Identification

Charge identification of the projectile-like fragment in the ^{84}Kr + ^{nat}Ag experiment was accomplished by constructing large ΔE

versus E intensity plots (see Fig. IV.2). Construction of these plots
with a low threshold permits the identification of the projectile Z
from slit scattering from collimators in front of the detector and
collimators upstream in the beam line. The atomic numbers were then
assigned to the resolved intensity bands ($Z < 40$) by counting up or
down from $Z = 36$. The regions of $\Delta E-E$ space corresponding to heavier
elements, where no bands were resolved, were obtained by extrapolating
the trends seen for the resolved bands. The boundaries of the regions
in the $\Delta E-E$ space corresponding to individual atomic numbers were
described by fourth order polynomials. The coefficients of these
polynomials were written on disk for use by subsequent programs. (An
interactive program MARCM has been written for this purpose. Versions
of this program exist on both the PDP-15 and the Modcomp IV computers.)

In the $^{nat}Ag + {}^{84}Kr$ experiments α-particles were identified
using a procedure identical to the one described above for selecting
heavy ions. Delta E-E maps such as the one shown in Fig. IV.3 were
used to define the two-dimensional α-particle region. Since the
software for the heavy-ion Z gating was not required for the $^{165}Ho +$
^{181}Ta experiment, it was more expedient to employ a standard soft-
ware particle identifier function (PI) to select α-particles. A PI
spectrum is shown in Fig. IV.4. The presence of charge 3 particles
suggests the intriguing possibility of using these particles for spin
determination. However, from the relative probabilities shown in the
PI spectrum, it is clear that such a project would be an ambitious
undertaking.

2) Heavy Ion Mass Assumptions

In the Kr experiments, the masses of both fragments are determined from the charge of the projectile-like fragment by requiring charge and mass conservation and by assuming that the neutron-to-proton ratio is equilibrated. Thus, for a given mass asymmetry, the charge asymmetry is that which minimizes the sum of the liquid drop energies. This procedure is suggested by a great number of studies [for example, Ga 75, Le 78, Kr 80], which show that the isospin degree of freedom is relaxed even during the early stages of energy dissipation. For the near symmetric systems (such as ^{84}Kr + ^{nat}Ag), similar results are obtained whether one uses this assumption or the more common one of equal N/Z ratios in the two fragments. However, for asymmetric systems or for the asymmetric exit channels of symmetric reactions, significant errors can be introduced by the latter assumption [Kr 80].

In the case of the ^{165}Ho + ^{181}Ta experiment, it was assumed that the primary mass of the detected fragment (before particle evaporation) was that of the beam particle (165 amu) and that the primary mass of the undetected fragment was 181 amu. This choice is motivated by several considerations. The first of these is the bias towards detecting the projectile-like fragment when a HI is detected at 29°. This bias can be understood by examining the Wilczynski plots [Wi 73] (contour diagrams of $d^2\sigma/d\Omega/dE_3$) for the similar systems; ^{208}Pb + ^{110}Pd, ^{208}Pb + ^{170}Er [Re 81] and ^{136}Xe + ^{207}Bi [Sc 77]. These plots not only show that the deflection function does not exhibit negative angle scattering, but also that when the bombarding energy of

these systems is high enough so that the reactions are not dominated by coulomb effects (as is the case with ^{208}Pb + ^{170}Er at 1180 MeV, $E_{c.m.}/B_{coul} = 1.04$), then the cross section, independent of energy loss, is focused into an angular region near the classical grazing angle. (This could be the result of a deflection function where the quasi-elastic and DI rainbows $(\frac{d\theta}{dl} = 0)$ occur at the same scattering angle.) This suggests that, for the ^{165}Ho + ^{181}Ta system at 1354 MeV $(E_{c.m.}/B_{coul} = 1.6$, which is the same value as the ^{136}Xe + ^{209}Bi), the projectile-like and target-like fragments will be focused into angular regions close to their respective laboratory grazing angles. Since the grazing angle of the target is more than 30° behind that of the projectile a strong selection on projectile-like fragments should be provided by placing the HI detector at the projectile grazing angle.

The other important justification for using the entrance channel masses as the primary exit channel masses is that for each of the similar heavy systems mentioned above the mass and charge distributions of the exit channel projectile-like fragment are well described by gaussian distributions centered on the entrance channel values. Even though the mass assumption employed is the most appropriate under the restriction that no charge or mass information is obtained directly from the present experiment, it must be considered as a zeroth order approximation because the variances of the charge and mass distributions mentioned above can be quite large $(\sigma_Z^2 > 100$ for the largest energy losses).

3) Radiation Damage Corrections

In the course of these experiments the HI detectors were exposed to approximately 10^8 particles/cm^2. This dose of very heavy ions produces significant damage in the Si detectors [So 81b]. One of the most obvious observables, which reflects this damage, is the loss of pulse height for elastic scattering. The correlation between the pulse height (for elastic scattering) versus dose is shown in Fig. IV.5 for a sample of detectors exposed to Kr, Xe, and Ho ions.

To correct for this pulse height loss, the slope of the energy calibration was increased as a function of dose. This procedure was carried out in increments of approximately 1-5 10^6 HI/cm^2. To prevent the radiation damage from distorting the Z-distribution, the location of an event in ΔE-E space was corrected to the dose level where the two-dimensional Z regions were defined.

4) Pulse Height Defect

The detected energy of the heavy ion was corrected for the pulse height lost due to charge recombination in the solid state detector. This pulse height defect (PHD), which is quite large for the highly ionizing HIs, was calculated following the prescription of Moulton et al. [Mo 78b].

5) Absorber and Target Energy Loss Corrections

The energies of all detected particles were corrected for the energy lost in absorbers and in the target. For the detected HI, these correction were done after the PHD correction. (For the α-particle detectors there is no PHD correction by definition.) The values of dE/dx were calculated by the method of Rattazzi et al.

[Ra 80]. The stopping powers predicted by this formulation are within 10% of those given in the tables of Hubert et al. [Hu 78]. The correction due to the presence of absorbers was done first, followed by the correction for the energy lost by the ion traversing one-half of the target thickness at the angle of observation.

6) Evaporation Corrections

Since the fragment energies are measured after particle evaporation, the fragment kinetic energies must be corrected for the energy lost in the evaporation process. The only significant correction to the DI fragment's mean kinetic energy due to evaporation arises from the lost mass. This correction was done by the iterative method described below. After the fragment energy is corrected back to the center of the target, the direction and energy of the undetected fragment are calculated with the mass assumptions described previously. The excitation energy (E^*) was calculated from the reaction Q-value. This excitation energy was then divided between the two fragments proportionally to their masses, as suggested by the results of several studies [Ey 78, Hi 79, Pe 77], and the lost mass of the detected fragment taken to be $E^*/12$. The pre-evaporative mass is then used to recalculate the energy (same velocity, see [Mo 78a]), which is the starting point of the next iteration. Two iterations are sufficient for the lost mass to converge within 1 amu.

The effect of this correction can be seen in Fig. IV.6 where corrected and uncorrected E_3 (detected fragment) and total kinetic energy (TKE, in the lab system) spectra are shown. As is expected, this correction shifts both spectra to slightly higher energies.

7) Coincidence Requirements

Coincidence events were selected by setting a gate around the peak in the TAC spectra corresponding to two different detectors (HI and α-particle or HI and γ-ray, see Fig. III.5) firing during the same beam burst. Random gates were set around neighboring beam bursts. However, these random corrections were generally insignificant as can be seen in the TAC spectra shown in Figs. IV.7 ($Z-\alpha$) and IV.8 ($Z-\gamma$). (The SuperHILAC beam microstructure frequency is approximately a factor of 10^3 larger than the fastest counting rates, therefore the probability that uncorrelated particles are detected in the same beam burst is small.)

The trailing edge of the real peak of the $Z-\gamma$ TAC (see Fig. IV.8) is primarily due to neutrons. Though the distance between the target, and the NaI detectors is insufficient to resolve the small neutron peak, the great majority of these relatively scarce Z-neutron events did not make a tight gate around the peak.

8) Rest Frame Transformations

As can be seen from the flow chart, Fig. IV.1, the α-particle in- and out-of-plane angles and the α-particle energy were transformed into the rest frame of the unobserved fragment. In addition, the solid angle Jacobian was calculated and written on tape. Subsequent sorting yielded energy spectra and angular distributions in the frame of the target recoil. In a similar manner transformations to other rest frames, such as the system center of mass, were also performed.

V. THE SOURCE OF ALPHA PARTICLE EMISSION

A. 181_{Ta} + 165_{Ho}

The singles HI energy spectrum is shown in Fig. V.la. At this
angle (29°) there are strong elastic (EL) and quasi-elastic (QE)
components that contribute to the peak above 1000 MeV. At lower
energies the DI component is spread out over several hundred MeV.
While the peak due to EL and QE scattering is dominant in singles
mode, it is strongly suppressed when a coincidence between an
α-particle and the heavy ion is required, as shown in Fig. V.lb.
(Actually the suppression is greater than it appears by the direct
comparison of parts a and b of Fig. V.1 due to the fact that part b is
not random corrected. When this correction is made there are essen-
tially no coincidences in the QE and EL region, region 1 in part b of
Fig. V.1.)

The laboratory energy spectra for α-particles in coincidence with
a heavy ion, with an energy in the DI region (the sum of gates 2, 3,
and 4 in Fig. V.lb), are shown in Figs. V.2 and V.3. Figure V.2 shows
these spectra for in-plane α-particle detection angles from 30° to 115°
from the beam axis; while Fig. V.3 displays the out-of-plane spectra
from 0° to 60° out of the reaction plane, at an in-plane angle of 55°.

The major features of these spectra can be summarized as
follows. The in-plane spectra show that the peak energy of the main
component is rather constant up to approximately 60°; however, as one
proceeds to more backward angles the peak energy monotonically
decreases with increasing angle. The out-of-plane spectra show a

steady decrease in the peak energy as the out-of-plane angle is increased. Finally, the most revealing feature of these spectra is the presence of two separate peaks at the most forward angle (30°). While examination of the data in this form does not lead to any firm conclusions concerning the emission source(s), the two peaks at forward angles suggests the tentative conclusion that there are at least two emission sources.

In order to determine these emission sources, the experimentally extracted root-mean-square velocity (v_α^{rms}) of the α-particles are plotted in Fig. V.4a. Also shown on this figure are the velocity vectors for the detected projectile-like fragment (gated on the deep-inelastic events), the calculated velocity of the undetected fragment, and the velocity of the system center of mass. As this figure shows, the α-particle velocities are centered around the end of the velocity vector of the target-like fragment. This agrees with the assumption that the α-particles are emitted from the fully accelerated target-like fragment. In addition, the low energy component seen at 30° can be attributed to emission from the projectile-like fragment. This component is not seen at more backward angles because it drops below the detection threshold, which is shown by the dashed arc in Fig. V.4.

Further evidence for fragment emission can be obtained by determining the Q-value dependence of v_α^{rms}. In Fig. V.4b the average vector diagram for three different Q-value bins are plotted (all in the deep-inelastic region, corresponding to regions 2, 3, and

4 in Fig. V.1b) along with the corresponding v_α^{rms}. A systematic motion of the locus of v_α^{rms} is seen that can only be explained by a source that has a Q-dependent velocity. This trend is explained by the change of the velocity of the target-like fragment with Q value, as shown in Fig. V.4b.

These vector diagrams indicate that the bulk of the α-particles are emitted from the target-like fragment. However, a small discrepancy with this picture can be seen if the α-particle energy spectra are examined in the rest frame of the target-like fragment. If the strong component observed in the laboratory energy spectra is the result of evaporation from the target-recoil nucleus, then the α-particle spectra in the recoil frame should have the same spectral shape at all angles. These spectra are shown in Fig. V.5 as a function of in-plane angle in the laboratory. The spectra are quite similar in shape and have peak energies of ~18 MeV, with the exception of the most forward angle data. While the spectra are quite uniform at backward angles, the most forward data show both a higher average α-particle energy and an increased yield. This can be seen in Fig. .6 where the average α-particle energy for emissions from the target-like fragment (the projectile-like emissions were removed by a low energy threshold) and the in-plane distribution are shown as a function of in-plane angle in the frame of the target-like fragment. The target-like fragment's recoil direction is arbitrarily taken as 0 degrees. The in-plane angular distribution is given in terms of the differential multiplicity [Ho 77]

$$\frac{dM_\alpha}{d\Omega_\alpha} = \frac{(\int dE_{HI} \ d\dot{E}_\alpha \ Y_C)_{DI}}{(\int dE_{HI} \ Y_S)_{DI} \ d\Omega_{Lab}} \quad , \tag{1}$$

where Y_C and Y_S are the coincident (corrected by the solid angle Jacobian, $\frac{d\Omega Lab}{d\Omega R.F.}$) and singles yields and $d\Omega_{Lab}$ is the α-particle detector's solid angle.

These data suggest that the target-like fragment is responsible for the bulk of emissions at angles equal to or larger than the recoil direction. However, there does seem to be an additional component that contributes at forward angles.

B. $^{nat}Ag + ^{84}Kr$

In Fig. V.7a the inclusive secondary charge distribution (after particle evaporation) measured at $\phi_{lab} = 26°$ is shown. This charge distribution increases monotonically as the Z-value increases toward symmetry, as has been observed in previous inclusive studies [Sc 78a, Sc 78b].

The fragment total kinetic energies (TKE) calculated by the procedure described in the previous chapter are shown in part b of Fig. V.7. A strong DI component is observed that is well separated from the quasi-elastic component. Since we were interested in α-particle emission from fully relaxed collisions, only $Z-\alpha$ coincidences that satisfied the gate shown in Fig. V.7b were analyzed. The high-energy shoulder above the elastic peak is due to a small amount of a heavy target contaminant that adds a negligible contribution to the DI region of the TKE spectra.

Representative singles α-particle energy spectra are shown in
Fig. V.8a for three lab angles. An increase in the complexity of the
spectral shape is observed as the lab angle decreases from 90° to
30°. This is not unexpected if the main source of α-particles is the
fully accelerated fragments. (This would be the case if there was no
prescission emission because the measured evaporation residue cross
section for this system is less than 50 mb [Br 76]). For this case
(fragment emission), the only emission source that should signifi-
cantly contribute at backward angles is the target-like recoil, while
at forward angles both fragments, with a large variety of velocities,
can act as emission sources. A coincidence with a DI fragment simpli-
fies the α-particle spectra as shown in Fig. V.8b. These energy spec-
tra, which are generated by requiring a coincidence with a fragment
having $26 \leq Z \leq 40$ and TKE in the DI region, are shown for the same
angles as part a. At 90° the singles and coincidence spectra are
similar. This confirms our expectation that at this backward angle
the bulk of the α-particles are emitted from the target-like recoil.
At 60°, the coincidence spectrum again shows only one component,
whereas the singles spectrum shows an additional low energy component.
At the most forward angle, the singles spectrum is quite complex,
whereas the coincidence spectrum can be interpreted in terms of a
strong component from the target recoil and a weak one from the
detected fragment. This latter component has a lower energy in the
lab system because it results from the backward emission from a fast-
moving source, as was the case for the ^{181}Ta + ^{165}Ho system.

The integrals of the α-particle energy spectra are shown in Fig. V.9 as a function of lab angle for both the singles a) and coincidence b) data. The singles angular distribution shows a strong forward peaking. This anisotropy is primarily due to the multiplicity of forward moving emission sources. The DI and Z-α coincidence requirements decrease the forward peaking. This is the result of the substantial reduction of strongly forward peaked components, such as emission from the projectile-like fragment.

As was done for the ^{181}Ta + ^{165}Ho data, a figure superimposing the V_α^{rms} on the average vector velocity diagram has been constructed. As can be seen from Fig. V.10 the trend of the data at angles equal to or larger than the recoil angle agree with the predictions [Ri 81, Al 81] based on emission from the target recoil. However, at forward angles the α-particle velocities are somewhat larger than expected for pure target-like fragment emission. To gain confidence that the main component in the coincidence spectra results from the statistical evaporation from the target-like DI product and to try to understand the apparent discrepancy with this picture seen at forward angles, the energy spectra must be examined in the rest frame of the target-like fragment.

Unlike the ^{181}Ta + ^{165}Ho analysis, the rest frame transformation for the ^{nat}Ag + ^{84}Kr system was done as a function of mass asymmetry. The assumptions and procedure for this transformation have been described in the previous chapter. A two-dimensional plot of the calculated laboratory recoil angle as a function of the atomic number of

the detected fragment is shown in Fig. V.11b. For reference a plot of the TKE as a function of charge of the detected fragment is given in Fig. V.11a in the same format as part b. The cluster of intensity at large TKE values and recoil angles of ~70° with Z of 36 ± 1 is attributable to elastic events. The DI component (see part a) shows a gradual increase in TKE as the system becomes more symmetric. For a deep-inelastic reaction the TKE is approximately the sum of the coulomb energy and the orbital rotational energy of the dinuclear complex. The above TKE dependence results from the fact that the dominant coulomb term reaches a maximum for the symmetric dinuclear system.

Figure V.11b shows that for the DI component the recoil angle varies with mass asymmetry from approximately 10° for the lightest detected fragments to 50° for symmetric divisions. For the region $26 \leq Z \leq 40$, the cross-section-weighted average recoil angle is $\phi_L \sim 40°$ with a FWHM of 16°. The evaporation correction amounts to 7° for $Z = 36$.

Several α-particle spectra in the recoil rest frame are shown in Fig. V.12 for representative in- and out-of-plane angles. These spectra were obtained by requiring a coincidence with projectile-like fragments ($26 \leq Z \leq 40$) having a TKE in the DI window. With the exception of the forward angle data, the spectral shape is independent of angle in this rest frame. This shape is evaporation-like with a peak energy of approximately 13 MeV.

The uniformity of these spectra as a function of angle strongly suggests that the bulk of these α-particles are emitted from the fully accelerated target-like fragment. This conclusion is also supported by the examination of the above data in the center of mass of the compound system (Fig. V.13). A shift in the peak position to higher energies is observed as one moves to larger angles implying that the true source must be moving in some direction with a large ϕ_L. In fact, the magnitude of the shift in the peak seen in Fig. V.13 can be readily understood if the rest frame is that of the target recoil.

The two most forward angles (30° and 42°, see Fig. V.12) contain a weak low-energy component, attributable to backward emission from the fast-moving projectile-like fragment. The only feature in these spectra that is not understood in terms of evaporation from excited nuclei is the excess of higher energy α-particles (above 15 MeV in the rest frame of the recoil, corresponding to a lab energy of ~40 MeV) observed at the most forward angle (30°).

These high-energy α-particles are correlated with an increase in the in-plane yield at forward angles. Figure V.14a shows the energy integrated in-plane α-particle angular distribution expressed as a differential multiplicity. The weak low-energy component from the projectile-like fragment, which is seen in the most forward data, has been subtracted out. The data exhibit very little angular dependence for the eight most backward angles. This is consistent with isotropic in-plane emission from the target-like fragment. However, again as

in the ^{181}Ta + ^{165}Ho case, a substantial increase above the average of these backward angles (dashed line) is seen for the two most forward angles.

The results from this study concerning the source of α-particles for both systems can be summarized by two statements. First, the bulk of the α-particles detected at angles equal to or larger than the target recoil angle, which are in coincidence with a projectile-like fragment deflected into an angular region around the grazing angle, are emitted from the fully accelerated target-like fragment. Second, there does seem to be a contribution of α-particles at forward angles that is not readily explained by emission from the fully accelerated fragments. However, this study did not focus on forward angle measurements; thus, insufficient data were acquired to determine the source of these α-particles.

VI. SPIN DETERMINATION

A. Gamma-ray Multiplicity.

As is often done, the sum of the fragment spins has been extracted from γ-ray multiplicity data, [Al 75, Le 79, Gl 77, Al 78, Ol 78, Ge 79, Na 79]. The γ-ray multiplicity data consist of the relative probabilities that N γ-rays will be detected in an array of γ-ray detectors. In the present experiments seven or eight NaI detectors were employed for this purpose. An example of a spectrum of these probabilities (N-fold spectrum) is shown in Fig. VI 1 (the logic for generating this parameter is shown in Fig. III 7). The algorithm described by Sarantities et al. [Sa 76] was employed to calculate M_γ from an N-fold spectrum.

The sum of the fragment spins was calculated from the relation, $I_L + I_H = 2(M_\gamma - 6) + I_p$. These spins as a function of exit channel mass asymmetry for the $^{nat}Ag + ^{84}Kr$ system are listed in Table 5. The corrections (I_p) for the angular momentum removed by the evaporated neutrons and α-particles were calculated following the prescription of Blau and Moretto [Bl 81]. These corrections averaged 28% and are therefore essential for a quantitative comparison between the spins derived from M_γ and the spins derived from the out-of-plane α-particle angular distributions, which are the subject of the remainder of this chapter.

B. The Data: out-of-plane α-particle distributions.

Since the bulk of the α-particles emitted at angles near or behind the recoil angle are emitted from the target-recoil fragment,

the out-of-plane angular distributions of α-particles in this angular region contain information on the spin of the target-like fragment.

1. ^{181}Ta + ^{165}Ho

For the ^{181}Ta + ^{165}Ho system data were acquired at an in-plane laboratory angle of 55° which is close to, but behind the average recoil angle ($\phi_4^L = 47°$). The measured α-particle energy spectra as a function of out-of-plane angle are shown in Fig. VI 2 (the in-plane angle is 55° for all of the spectra). The angle from the normal to the reaction plane* ($\theta' = 90 \theta$) varies from 90° (in-plane) to 30°. The most out-of-plane spectra, 60° out of the reaction plane ($\theta' = 30°$), corresponds to ~ 90° out-of-plane in the rest frame of the target recoil. Therefore, the entire 0°-90° range is covered by the data shown in Fig. VI 2.

The integrals of the spectra shown in Fig. VI.2 are shown in Fig. VI.3 as solid circles. This figure clearly indicates the decrease in yield as the out-of-plane angle increases (or as the angle from the normal to the reaction plane decreases) with an in- to out-of-plane anisotropy (yield in-plane/yield out-of-plane) of ~ 1.4. Such a focusing of the α-particles into the reaction plane is of course expected for an object spinning about an axis parallel to the normal to the reaction plane. The upturn in the angular distribution at the most out-of-plane point ($\theta' \sim 9°$) is inconsistent with this expectation. This discrepency (~ 10% from a smooth curve drawn through the other points) is considerably larger than the statistical error (approximately the size of the points) and therefore must be

attributed to a systematic effect. It is possible that this discrepancy could be due to a small (10%) contamination of the main evaporative component from the target-like nucleus by emissions from the projectile-like fragment. A contamination of this magnitude to the low energy portion of the most out-of-plane spectrum would not significantly distort the spectral shape.

2. $^{nat}Ag + ^{84}Kr$

The out-of-plane angular distribution for the $^{nat}Ag + ^{84}Kr$ system is shown on Fig. V.14b. The in-plane angle for these data is $\phi_4^L = 41°$ which is the average recoil direction for the analyzed data (TKE in the DI window and $26 \leq Z_3 \leq 40$). In contrast to the in-plane angular distributions (Fig. V.14a), the out-of-plane yield decreases smoothly with increasing out-of-plane angle, exhibiting an anisotropy of approximately 2.

In Fig. VI.4a angular distributions for six Z-bins are shown. (Here the distributions are labeled by the charge of the emitting fragment.) A gradual sharpening of the angular distributions as the charge of the emitter increases is evident. Since the anisotropy of the out-of-plane angular distributions of sequentially emitted particles should increase with the spin of the emitter, this observation tentatively indicates that the fragment spin increases with the mass asymmetry.

Because the γ-ray multiplicity reflects the sum of the spins of both fragments, it is of interest to see how sensitive the α-particle angular distributions are to the γ-ray multiplicity. In part b of

Fig. VI.4 angular distributions are shown for the same Z bins as shown
in part a, but with the additional requirement that two or more γ rays
be in coincidence with the α-particle and the DI fragment. This re-
quirement was imposed by putting a gate on the N-fold parameter, Fig.
VI.1. In the mass region covered by this study, the γ-ray multipli-
city is linearly related to the sum of the spins of the two fragments
[Na 79, St 79]. Thus, requiring an increasing number of γ-rays to be
in coincidence with Z–α events should bias the fragment's spin distri-
bution towards larger values and result in a greater focusing of the
angular distribution into the reaction plane.[**] This effect is
clearly seen when parts a and b of Fig. VI.4 are compared.

C. Formalism.

The formalism developed by Moretto, Blau and Pacheco [Mo 75, Mo
81a] has been used to analyze the out–of–plane α-particle angular
distributions. This formalism is based on the transition state
concept [for example, Ha 58 and Gl 41] and treats sequential fission
and sequential light particle emission within the same framework.
This method [Mo 81a] has been used in the analyses of both types of
data (sequential fission [Mo 82, Le 81] and the α-particle [So 81a]).
To facilitate comparison with other studies which employ different
formalisms, this section describes the formalism of Moretto et al. at
several levels of sophistication.

For the description of angular distributions using the transition
state model, the rotational energy at the critical decay shape (the
shape where the decay process becomes irreversible, the saddle point

shape in the case of fission) must be known. This energy can be
written as

$$E_{rot} = \frac{\hbar^2}{2\mathcal{J}_\perp} (I^2 - K^2) + \frac{\hbar^2}{2\mathcal{J}_\parallel} K^2 \qquad . \tag{2}$$

The quantities in this expression are shown in Fig. VI.5 where the
critical shape for light particle emission is schematically depicted.
The total angular momentum is I and its projection onto the separation
axis is K. The moments of inertia $\mathcal{J}_\perp$ and $\mathcal{J}_\parallel$ are related to the
rotations about the axes perpendicular and parallel to the separation
axis. This implies that the probability that the saddle configuration
has any given K value is proportional to

$$e^{-\left[\frac{\hbar^2}{2\mathcal{J}_\perp} (I^2 - K^2) + \frac{\hbar^2}{2\mathcal{J}_\parallel} K^2 \right] / T} \tag{3}$$

where T is the nuclear temperature. Using the transition state
assumption [Ha 58] that the final K-distribution is determined by the
K values which characterize the nucleus at the critical decay shape,
the particle decay width can be written [Mo 75, Mo 81a] as

$$\Gamma \alpha e^{-\left[\frac{\hbar^2 I^2}{2T} \left(\frac{1}{\mathcal{J}_\perp} - \frac{1}{\mathcal{J}_c} \right) \right]} e^{-\left[\frac{\hbar^2 K^2}{2T} \left(\frac{1}{\mathcal{J}_\parallel} - \frac{1}{\mathcal{J}_\perp} \right) \right]} \tag{4}$$

where the rotational energy and moment of inertia of the compound
nucleus are $\hbar^2 I^2 / 2\mathcal{J}_c$ and $\mathcal{J}_c$, respectively.

Equation 4 can be rewritten as

$$\Gamma \propto e^{-\left[\frac{\hbar^2 I^2}{2T}\left(\frac{1}{\mathcal{J}_\perp} - \frac{1}{\mathcal{J}_c}\right)\right]} e^{-\frac{K^2}{2K_0^2}} \tag{5a}$$

where

$$K_0^2 = \frac{\mathcal{J}_{eff}T}{\hbar^2} = \frac{T}{\hbar^2}\left(\frac{1}{\mathcal{J}_\parallel} - \frac{1}{\mathcal{J}_\perp}\right)^{-1} \qquad . \tag{5b}$$

Thus this statistical mechanic: approach predicts a Gaussian distribution for the projection (K) of the angular momentum on the heavy-ion evaporated particle separation axis. The variance of this distribution is given by the parameter K_0^2.

The angular distribution of the evaporated particles is obtained by expressing the angle (α) between the total angular momentum I, and the separation axis (y axis, see Fig. VI.5) with unit vector $\hat{n}$, in terms of the polar angles ϕ' and θ'.

$$K = I \cdot \cos\alpha = I \cdot \hat{n} = I_y \sin\theta' \cos\phi' + I_x \sin\theta' \sin\phi' + I_z \cos\theta'. \tag{6}$$

If the direction of the angular momentum is fixed, we may choose our coordinate system such that $I_x = I_y = 0$ and $I_z = I$. Under this condition of total alignment of the angular momentum, the angular distribution is given by

$$\omega^{(1)}(\theta') \propto \exp\left(\frac{-I^2\cos^2\theta'}{2K_0^2}\right) \exp\left(\frac{I^2\sin^2\theta'}{2K_0^2}\right) \qquad . \tag{7}$$

This relation can also be derived from the Ericson and Strutinski [Er 58] formalism by integra·ing over the distributions of orbital angular momenta and energy of the emitted particles [Dφ]. This expression has been employed in the analysis of previously reported deep-inelastic [Ba 80] and compound nucleus data [Ca 80].

Since there is good evidence for rather large misalignments of the fragment spins in deep-inelastic reactions [Ch 80, McD 82], this effect should be included in the angular distribution formalism. If the spin alignment of one fragment is described by Gaussian distributions in the Cartesian components of the angular momentum with variances σ_x^2, σ_y^2, and σ_z^2, then the light particle decay width is given by [Br 79, Mo 81]

$$\Gamma\ (\theta',\phi') \propto \exp\left[\frac{-I^2\hbar^2}{2T}\left(\frac{1}{\mathcal{J}_1}-\frac{1}{\mathcal{J}_c}\right)\right]\frac{1}{S(\theta',\phi')}\ \exp\left[\frac{-I^2\cos^2(\theta')}{2S^2(\theta',\phi')}\right] \quad (8a)$$

with

$$S^2(\theta',\phi') = K_0^2 + \sigma_y^2\ \cos^2\phi'\ \sin^2\theta' + \sigma_x^2\ \sin^2\phi'\sin^2\theta' + \sigma_z^2\ \cos^2\theta' \quad (8b)$$

which gives a form similar to equation 7 for the angular distribution,

$$\omega^{(2)}(\theta',\phi') \propto \frac{1}{S(\theta',\phi')}\ \exp\left[\frac{-I^2\cos^2\theta'}{2S^2(\theta',\phi)}\right] \quad . \quad (9)$$

By fitting equation 9 to an out-of-plane distribution one can extract the root-mean-square spin of the primary spin distribution biased by the angular momentum dependence of α-particle emission.

To obtain the correct form for the angular distribution of light particles evaporated from nuclei which have a distribution of spins, one must integrate the form for the angular distribution for a given spin over the spin distribution of the parent nucleus. This integration is important not only because the shape of the angular distribution changes with spin, but also because competition between various possible ejectiles can significantly change with angular momentum. Thus spins evaluated from one expression derived without this integration can only be related to the distribution of spins leading to that particular particle decay. However, integration over the spin distribution weighted by the angular momentum dependence of the emission probably leads to spins that are related to the primary spin distribution.

This integration is of the form,

$$\omega_\nu(\theta',\phi') = \int_{I_{min}}^{I_{max}} P(I) \; \frac{\Gamma_\nu(I,\theta',\phi')}{\Gamma_T(I)} \; dI \qquad . \qquad (10)$$

In this expression,

$\omega_\nu(\theta',\phi')$ = the angular distribution of particle ν,

$P(I)$ = the spin distribution,

$\Gamma_\nu(I,\theta',\phi')$ = the decay width of particle ν as a function of angular momentum and angle,

$\Gamma_T(I)$ = the total decay width as a function of angular momentum.

Since it is reasonable to expect that the fragment spin distribution will reflect the entrance channel angular momentum distribution, one can take the formalism a step farther by folding the angular distribution function with the fragment spin distribution. If the fragment's spin distribution is taken to be of the form 2I and bound by I_{min} and I_{max}, then the angular distribution is given by

$$\omega_\alpha(\Theta',\phi') = \int_{I_{min}}^{I_{max}} 2I \ \frac{\alpha^{(I,\Theta',\phi')}}{\Gamma_T} \ dI \qquad . \qquad (11)$$

This expression depends upon the relative magnitude of the alpha and neutron total decay widths. These widths can be determined from experimental data or the ratio,

$$\frac{\Gamma_\alpha}{\Gamma_n} = \Delta e^{I^2\beta} \qquad (12a)$$

$$\text{where } \Delta = \frac{1}{2} \exp \ \left[- (BE_\alpha + CB_\alpha - BE_n)/T\right] \text{ and} \qquad (12b)$$

$$\beta = \frac{\hbar}{2T} \left(\frac{1}{\mathcal{J}_n} - \frac{1}{\mathcal{J}_\perp}\right) \qquad . \qquad (12c)$$

In the expression for Δ, BE_α and CB_α are the α-particle binding energy and Coulomb barrier for α-particle emission, while BE_n is the neutron binding energy. The parameter β accounts for the change in the relative α/n decay widths as a function of angular momentum. This parameter depends upon the moment of inertia of the residual nucleus after neutron emission, $\mathcal{J}_n$, as well as $\mathcal{J}_\perp$ and the nuclear

temperature (T). If the ratio Γ_α/Γ_n is small, then $\Gamma_T \approx \Gamma_n$ and the integral in equation 11 can be evaluated, with the analytical result,

$$\omega^{(3)}(\theta',\phi') \propto (e^{-I_{min}^2 A} - e^{-I_{max}^2 A})/S(\theta',\phi')A \tag{13a}$$

$$\text{where } A = \frac{\cos^2\theta'}{2S^2(\phi',\theta')} - \beta \qquad . \tag{13b}$$

If Γ_α is not much smaller than Γ_n then the integral in equation 11 can be solved for $\Gamma_T = \Gamma_n + \Gamma_\alpha$ to yield the more complicated expression given below:

$$\omega^{(4)}(\theta',\phi') \propto \left(Q_{min} e^{-I_{min}^2 A} - Q_{max} e^{-I_{max}^2 A}\right) \Big/ S(\theta',\phi') \tag{14a}$$

where

$$Q_i = \ln(e^{-\beta I_i^2} + \Delta)/2\beta + \frac{I_i^2}{2} + \frac{1}{2A} + \frac{A}{\beta} \sum_{n=1}^\infty \frac{(-i\Delta)^n e^{nI_i^2\beta}}{2n(A-n\beta)} \qquad . \tag{14b}$$

The derivation of this expression is provided in Appendix A.

Each of the four forms of the angular distribution (Eqs. 7, 9, 13, and 14) depend upon some of the following parameters: I_{rms}, I_{min}, I_{max}, T, $\hbar_{eff}$, β, σ_y^2, σ_x^2, σ_z^2, and Δ. While some of these parameters can be extracted from the experimental data, others can be calculated from reasonable models. The determination of these parameters, the

sensitivity of the angular distribution to these parameters, as well as the results of calculations using each of the forms $\omega^{(1)}$ through $\omega^{(4)}$ are discussed in the next section.

D. Alpha-particle Results
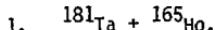
1. $^{181}\text{Ta} + ^{165}\text{Ho}$.

The choice of parameters for the analysis of the out-of-plane distribution from the $^{181}\text{Ta} + ^{165}\text{Ho}$ experiment is greatly simplified by a number of experimental observables. To start with, the α-particle multiplicity is small and therefore Γ_α/Γ_n is much less than 1. Under this condition, Eq. 14 reduced to Eq. 13. Furthermore, since the evaporation residue cross section is small or negligible, I_{min} is approximately 0, which reduces the first term in Eq. 13 to unity.

For asymmetric systems there is both experimental [Dy 79, Le 81, Mo 82] and theoretical [Br 79, Sc 82] work that suggests the variances σ_x^2, σ_y^2 and σ_z^2 are not equal. On the other hand, in-plane sequential fission angular distributions for near symmetric systems do not exhibit large anisotropies for DI events, indicating that the in-plane widths (σ_x and σ_z) are not significantly different. This result supports the equilibrium model developed by Moretto and Schmitt [Mo 80] and Schmitt and Pacheco [Sc 82], which predicts $\sigma_x^2 \sim \sigma_y^2 \sim \sigma_z^2$ for near symmetric systems. This model derives some additional support from its ability to reproduce the γ-ray anisotropies measured by McDonald et al. [McD 82]. In this work the continuum γ-ray multiplicity and anisotropy were measured for the $^{165}\text{Ho} + ^{165}\text{Ho}$ at 8.5 MeV/amu system. These

measured quantities along with the spin per fragment, extracted from the M_γ data, are shown in Fig. VI.6 for three angles. Though γ-ray anisotropies are insensitive to the differences in the in-plane widths, and to first order insensitive to σ_z, they are sensitive to the misalignment (which is related to the magnitude of the in-plane spin component).

If the simplification suggested by the equilibrium model is employed the parameter S is no longer a function of angle, i.e., $S^2 = K_0^2 + \sigma^2$. Using this simplification, which is supported by experimental data, the most sophisticated form for the angular distribution reduces to,

$$
\omega\ (\theta')\ \alpha \left(1 - e^{-I_{max}^2 A} \right) \Big/ SA \qquad . \tag{15}
$$

The angular dependence is contained in the parameter A (Eq. 13b).

Though the experimental data do not suggest further simplifications in the form of the angular distribution, they do provide information on the remaining parameters. The ^{165}Ho + ^{165}Ho study [McD 82] suggests values for both I_{max} and σ^2. Since the values of ℓ_{max} are almost identical for the ^{165}Ho + ^{165}Ho and the ^{181}Ta + ^{165}Ho systems (the slightly larger interaction radius of the later system is compensated by a lower average energy in the center of the target) the spin of an individual fragment deduced from the M_γ work of McDonald et al. can be used to estimate Imax. For the ^{165}Ho + ^{165}Ho system the average primary spin per fragment when one of the fragments is detected near the grazing angle is ~ 33ħ. (See the center

plot in the collage of plots in Fig. VI.6.) Since I_{max} in Eq. 15 is
the maximum spin of a triangular distribution, it can be estimated
from the average experimental spin,

$$I_{max} = \frac{3}{2} I \sim 49.5 \qquad . \tag{16}$$

As mentioned earlier, the $^{165}Ho + ^{165}Ho$ data were successfully
reproduced with the model of Moretto and Schmitt [Mo 80]. This model
predicts that for a symmetric system,

$$\sigma^2 \sim T\mathcal{J} \tag{17}$$

where $\mathcal{J}$ is the moment of inertia of one of the two fragments. In the
present analysis the moment of inertia of a spherical fragment with
the mass of the target was used, ($\mathcal{J} \sim 83 \ \hbar^2/MeV$). The temperature
can be calculated from the average energy available for thermal
excitation from,

$$E^* = aT^2 \tag{18a}$$

with the level density parameter $a = A/8 \ MeV^{-1}$ and

$$E^* = E_{loss} - E_{rot} \qquad . \tag{18b}$$

The small correction ($\leq 4\%$) for the energy involved in rotation of the
fragments was calculated using rigid rotation predictions. The result

is a temperature of $2.5 \pm .1$ MeV. The error is due to the uncertainty
in the detected fragment's mass which results in an uncertainty in
E_{loss}.

To check the Q-value deduced temperature, an independent value
was extracted from the tail of the α-particle energy spectra.
(Actually, the temperature deduced from the α-particle spectra should
be slightly lower than the value deduced from the Q-value due the
α-particle binding energy and translational energy that are removed by
the emission process. These energies, which should be subtracted from
the right hand side of Eq. 18b, are much less than E_{loss} and change
T less than the error introduced by the mass uncertainty mentioned
above.) The α-particle energy spectra, Fig. VI.a, not only provide
information on T but also on $\mathcal{J}_{eff}$. This is due to the fact that the
critical decay shape not only determines the relevant moments of iner-
tia (Eq. 5b) but also the Coulomb barrier and thus the mean energies.
Thus by adjusting the critical decay shape so that the energy spectra
are reproduced, $\mathcal{J}_{eff}$ can be calculated from the values of $\mathcal{J}_{\parallel}$ and $\mathcal{J}_{\perp}$
for this configuration, see Fig. VI.5.

The α-particle energy spectrum was calculated using the formalism
described in Mo 75. This formalism models the critical decay shape by
the equilibrium configuration of the rotating fragment, α-particle
complex in a spheroid-sphere model. Shape polarization and fluctua-
tions about the equilibrium shape, which has a ratio of axes of ~ 1.1,
were taken into account. The polarization and fluctuations contribute
both to "sub-barrier" emission and to harder tails than would

otherwise be present. By adjusting the surface separation ($S = 1$ fm) and radius parameter ($r_0 = 1.5$ fm) the spectrum superimposed on each of the five out-of-plane spectra shown in Fig. VI.1 was calculated. The close agreement between the data and the calculation (which uses a temperature of 2.5 MeV) in the region of the peak and in the slope in the high energy tail corroborates the Q-value deduced temperature. The calculation does not reproduce the data in the low energy region, ($\leq$ 15 MeV) because the formalism does not explicitly include barrier penetration. In addition, the very low energy portion of the spectra may contain some projectile-like emissions. This type of contamination would be most serious for the most out-of-plane spectrum because the average lab energy of the main component drops to only 15 MeV above the threshold, making it difficult to identify a still lower energy contaminant.

From the geometry and parameters given above the values of $\mathcal{A}_{\perp}$ and $\mathcal{A}_{\parallel}$ and thus $\mathcal{A}_{eff}$ were calculated. To calculate $\mathcal{A}_n$ (needed for β, see Eq. 12c), the residual nucleus after neutron emission was taken to be spherical.

Using the parameters described above, the out-of-plane distribution shown in Fig. VI.3 (solid line) was calculated using Eq. 15. The calculation agrees quite nicely with the data with the exception of the most out-of-plane point, which as mentioned earlier is probably subject to a systematic error.

The calculated shape of the α-particle out-of-plane angular distribution is quite sensitive to the parameters I_{max} and K_0^2 but is insensitive to the other parameters. The insensitivity to the

magnitude of the misalignment can be seen by comparing the relative magnitudes of σ^2 and K_0^2. In this case $\sigma^2/K_0^2 \sim 1/7$; thus the inclusion of σ^2 changes S^2 by only 14%. Since the shape of the angular distribution is roughly constant for a fixed value of I_{max}/S, increasing I by $\sim$ 7% compensates for the inclusion of σ^2. Because of this insensitivity, no effort was made to make further refinements concerning spin misalignments. Such refinements, which can include the effects of deformation and unequal misalignments, may be important for sequential fission work were $\sigma^2 \sim K_0^2$.

The sensitivity of the calculation to the two most important parameters I_{max} and K_0^2 is illustrated in Fig. VI.3. The dashed lines indicate a 10% change in either of the parameters. Explicitly, the upper dashed line is the result of a 10% decrease in I_{max} or approximately a 10% increase in K_0. Since these curves systematically disagree with the data it is clear that, for example, the average spin can be estimated to better than 10% if K_0^2 is known. Perhaps the most important result from the ^{181}Ta + ^{165}Ho study is that the formalism described in part B of this chapter, when coupled with input parameters extracted from experimental data, does an admirable job of reproducing the out-of-plane distribution.

2. ^{nat}Ag + ^{84}Kr.

As was mentioned in Section VI B, the sharpening of the angu'·r distributions as the charge of the emitter increases (Fig. VI.4) tentatively indicates that the spin of the heavy fragment increases with mass asymmetry. The word "tentatively" was used because the shape of the distribution depends upon several parameters in addition

to the spin. However, as we have just seen in the previous subsection the shape of the out-of-plane distribution is most sensitive to the parameters I_{max} and K_0^2. Thus, to determine whether the tentative conclusion is correct all one needs to know is the trend of K_0^2 with asymmetry of the DI exit channel.

As the mass asymmetry of the sequential decay channel (in this case HI $-\alpha$) increases, K_0^2 increases. This is due to the fact that the relative contribution of the light fragment (α-particle) to $\perp$ decreases as does the polarization of the major fragment (see Fig. VI.5). Thus $\mathcal{J}_\perp$ tends to a value near $\mathcal{J}_\parallel$ as the sequential decay asymmetry increases and K_0^2 becomes quite large, (see Eq. 5b). Since we are studying emissions from the larger of the two DI fragments, the mass asymmetry of the sequential α-decay channel increases with increasing asymmetry of the DI exit channel. Thus to get the trend seen in Fig. VI.4, not only must the average spin increase with mass asymmetry, but it must increase faster than K_0 does.

To quantitatively extract spins from the out-of-plane distributions values for K_0^2 must be known. Unfortunately, the energy spectra for the individual Z bins do not have sufficient statistics to obtain accurate values of K_0^2 for each asymmetry. Due to this difficulty the angular distributions shown in Fig. VI.3 have been fit to all four forms of the angular distribution with various sets of parameters. The methods for the calculation of the parameters (most importantly K_0^2) are described below. These fits indicate that while there is some ambiguity concerning the absolute magnitude of the spins (because of uncertainty of K_0^2) the trend with mass asymmetry is well established.

The root-mean-square spin values for the heavy fragment, extracted as a function of exit channel charge asymmetry, are shown in table 5. The errors listed in this table represent only the statistical error. The columns correspond to different levels of sophistication in the formalism used to extract the spins. The temperatures used to calculate K_0^2 were calculated using Eq. 18. However, the excitation energy (E*) was corrected for the difference in binding energy between the entrance and exit mass asymmetries. This small correction employed liquid drop energies and the equilibrated masses (see Chapter III). The temperatures calculated with this procedure varied from 2.75 (most asymmetric bin) to 2.95 (symmetric bin), which are in close agreement with the value of 2.9 MeV which was extracted from the unbinned α-particle energy spectra shown in Fig. V.12.

The spins in columns a and b both result from fitting equation 7 to the out-of-plane distributions. These two sets of spins differ only in the method used to calculate K_0^2. To generate the spins in the first column, the critical shape for decay of the α-particle-residual nucleus system is that of two touching spheres. With this model the moments of inertia are given by

$$\mathcal{J}_{\parallel} = \mathcal{J} \; ; \mathcal{J}_{\perp} = \mathcal{J} + \mu d^2 = \mathcal{J} + \mu (r_0 M^{1/3} + R_\alpha)^2 \quad . \tag{19}$$

Here, is the moment of inertia of the residual nucleus and is equal to 2/5 MR^2. The radius of the α-particle was taken to be, R_α = 2.53 fm and r_0 = 1.225 fm.

The trend of these extracted spins agrees with the predictions of rigid rotation of the deep-inelastic complex which consists of two touching spheroids. However, the magnitudes do not agree with the results from γ-ray multiplicity work. Both previous work [Al 78] and the present study obtained values for M_γ of less than 25 for all measured asymmetries. A comparison of the total spins obtained from the M_γ data (column g) with the individual spins (column a) extracted with equation 7 assuming a spherical critical shape for α-particle decay clearly indicates that the use of this configuration results in an overestimate of the fragment spin.

For the second column in table 5 the critical shape was taken as the equilibrium configuration of the rotating fragment-α complex in a spheroid-sphere model [Mo 75]. This configuration is more extended along the separation axis than two touching spheres (ratio of axes is ~ 1.1). This results in a reduced value of K_0^2 and in smaller spin values. This reduction in K_0^2 improves the agreement between the spin values extracted from the M_γ data and the α-particle distributions. This improved picture of the α-particle-residual nucleus system is used in the subsequent formulations of the angular distribution.

The spin misalignment is introduced by means of eq. 9. Due to the predicted insensitivity of the α-particle distributions on this misalignment and the near symmetry of the system, the simplifying assumption $\sigma_x \sim \sigma_y \sim \sigma_z$ was used. The values of σ^2 (as a function of mass asymmetry) were calculated with Eq. 17 assuming spherical

fragments and $r_0 = 1.225$ fm. The inclusion of misalignment increases the spins by 2 to 3$\hbar$ (Table 5, compare columns b and c). The importance of the misalignment on the extracted spin value can again be related to the relative magnitude of σ^2 and K_0^2. In this case $\sigma^2/K_0^2 \sim 1/4$; thus, including σ^2 changes S^2 by $\sim 25\%$ and therefore the fragment spin by only $\sim 10\%$. (The ratio σ^2/K_0^2 is larger than in the previous case primarily due to the decreased mass asymmetry of the sequential decay. This asymmetry, however, is still sufficiently large so that the distributions are quite insensitive to σ^2.)

The spins contained in the next two columns of table 5 (d and e) are obtained from the spin-integrated forms of the angular distribution, respectively equations 13 and 14. The lower limit of integration, I_{min}, was estimated from the lowest ℓ-wave, ℓ_{min}, leading to a nonevaporation residue event and then assuming rigid rotation of the intermediate complex. The value of ℓ_{min} was calculated from the evaporation residue cross section [Br 76] in conjunction with the sharp cutoff approximation.*** The parameter Δ was estimated from the total α-particle multiplicity considering the contribution to this multiplicity from second chance emissions. The spins from these integrated forms (columns d and e) agree within 5% of those obtained from the unintegrated form (column c).

As expected the spin of the heavy fragment increases with increasing mass asymmetry. The spins in column e are plotted in Fig. VI.7. These spins are compared to several model calculations in the next chapter, but before proceeding with this comparison it is

interesting to see the effect of gating on high M_γ events. Also shown in Fig. VI.7 are the spins extracted (eq. 14) from the distributions (Fig. VI.4b) generated with the requirement of at least two coincident γ-rays. As can be seen by comparing the closed circles (no γ-ray requirement) to the open circles (≥ 2 γ-rays) that the effect of gating on high M_γ events is to increase the average spin per fragment by approximately $2\hbar$.

VII. SPIN CALCULATIONS

It is convenient to know the predictions of some simple friction models when one is trying to use data to elucidate the process by which orbital angular momentum is converted into intrinsic fragment spin. (In this regard, the interested reader m·.y wish to consult the reviews Le 79, Bo 77.) Two possible friction forces, which can create intrinsic spin, are sliding friction and rolling friction. In the contrived situation that only sliding friction is acting, the two nuclei roll on each other. However, if rolling friction is present the nuclei will eventually stick and rotate rigidly. When both frictional forces are present one can envision that the nuclei behave in a fashion analogous to what happens when a ball is thrown down a smooth plane (such as in bowling). At first the two surfaces slide over each other; after a time, the rolling limit is reached. After a further passage of time the equilibrium limit of rigid limit is reached (a situation which plagues small children when they bowl for the first time).

A. Rolling.

For the case of rolling friction a simple relationship between the angular momentum induced in each nucleus and the moment arms or radii can be derived [Le 79, Bo 77],

$$\frac{I_1}{I_2} = \frac{R_1}{R_2} \tag{20}$$

where $I_{1,2}$ are the induced fragment spins and $R_{1,2}$ are the radii
of the two nuclei. This relation (Eq. 20) is valid when the frictional
force acts only at the point of contact, as in the sliding stage and
rolling limit, but need not be true with more complicated frictional
forces.

Combining Eq. 20 with the rolling condition that the peripheral
velocities of the two fragments must be equal and utilizing rigid
sphere moments of inertia, results in the relation

$$I_1 + I_2 = \frac{2}{7} I_{tot} \qquad , \qquad (21)$$

where I_{tot} is the total angular momentum of the system. Equations
20 and 21 imply that in the rolling limit the individual fragment
spins are only weakly dependent on mass asymmetry ($R \propto A^{1/3}$) and
that the sum of the fragment spins is a fixed fraction of the total
angular momentum and thus independent of mass asymmetry.

B. Rigid Rotation.

The sticking condition is specified by the condition that the
angular velocities of the two fragments $(\omega_{1,2})$ and the angular
velocity of relative motion (ω_{rel}) are all equal

$$\omega_1 = \omega_2 = \omega_{rel} \qquad \cdot \qquad (22)$$

This equality leads to the partition of angular momentum in proportion
to the relevant moment of inertia,

$$I_i = I_{tot} \frac{\mathcal{J}_i}{\mathcal{J}_1 + \mathcal{J}_2 + \mathcal{J}_{rel}} \qquad (23)$$

where i = 1, 2, or rel.

Thus,

$$I_1 : I_2 : I_{rel} = \mathcal{J}_1 : \mathcal{J}_2 : \mathcal{J}_{rel} \qquad .$$

In those expressions $\mathcal{J}_1$, $\mathcal{J}_2$, and $\mathcal{J}_{rel}$ are the moment of inertia for fragment 1, the moment of inertia for fragment 2, and the moment of inertia for relative motion, respectively. Therefore, in the rigid limit an individual fragment's spin is strongly dependent on its mass. This dependence in the case of spherical rigid body moments of inertia is roughly $I \propto A^{5/3}$ $(\mathcal{J} = 2/5MR^2)$. Equation 23 can also be used to predict the sum of the fragment spins, $I_1 + I_2$. This sum has a minimum for symmetric masses, $(A_1 = A_2, \mathcal{J}_1 = \mathcal{J}_2)$ at $I_1 + I_2 = 2/7 \ I_{tot}$, when the complex is modeled by two touching spheres with rigid body moments of inertia.

For comparison, the predictions of both rolling and rigid rotation for the individual fragment spin and the sum of the spins is shown in Fig. VII.1. This figure clearly illustrates that the predictions of the two limits are quite similar in both magnitude and slope for the sum of the spins near symmetry. On the other hand, the two predictions for the dependence of an individual fragment's spin on mass asymmetry strongly differ at symmetry.

C. Rigid Rotation plus Angular Momentum Fractionation.

Gamma-ray multiplicity studies of several Kr reactions conducted by Aleonard et al. [Al 78] gave results that were inconsistent with the simple rigid rotation model described above, see Fig. VII 2. Rather than give up the equilibrium limit of rigid rotation which had been verified for lighter systems and implied by the relaxed kinetic energies, it was suggested [Al 78, Re 78] that there was an ℓ-wave fractionation with mass asymmetry. This fractionation would produce a bias in the ℓ-wave distribution which populates a given mass asymmetry such that the larger the asymmetry the lower the average ℓ-wave. Since the average ℓ-wave would decrease with asymmetry, the fragment spins would not show the expected increase with asymmetry even if the dinuclear complex was rotating rigidly, see Fig. VII 2.

The theoretical justification of an ℓ-wave fractionation is twofold. First, long interaction times and thus low ℓ-waves are needed to populate large asymmetries. The second justification is due to the fact that the potential energy as a function of mass asymmetry depends strongly on angular momentum. A perspective plot of a potential energy surface, which is similar to those for the Kr reactions, is shown in Fig. VII 3. This figure illustrates that for most asymmetries the potential energy slopes toward symmetry, and that the slope increases with angular momentum. Therefore, large asymmetries tend to be populated by low ℓ-waves. Calculations of the equilibrium ℓ-wave distributions populating each asymmetry can be done using the formulae of Moretto and Schmitt [Mo 80] or by using a

diffusion model (in the long interaction time limit) [Ri 78]. Calculations for the $^{nat}Ag + ^{84}Kr$ system using a diffusion model [Sc 80] indicate that, for example, the mean ℓ-wave value populating $Z_3 = 26$ is ~ 80% of the value populating $Z_3 = 36$.

D. Calculations versus Data.

The rolling limit predicts a change of only ~ 2.5$\hbar$ over the asymmetry region shown in Fig. VI 7. Since the observed change is more than four times this value, it is clear that the rolling limit (infinite sliding friction but no rolling friction) provides a poor description of actual frictional forces. On the other hand, the rigid rotation calculation (solid line in Fig. VI 7) does an admirable job of reproducing the experimental data with the exception of the most asymmetric points. These asymmetric points, where the measured spins fall below the rigid rotation calculation, suggest the influence of ℓ-wave fractionation on the fragment spins for the most asymmetric exit channels.

The dashed line in Fig. VI 7 is a rigid rotation calculation where the total angular momentum (I_{tot}) for each asymmetry is taken as the mean ℓ-wave populating that asymmetry as determined by a diffusion model in the long time limit [Sc 80]. The fact that the data fall between the rigid rotation calculation with a constant ℓ-wave window and the calculation just described suggests that there is ℓ-wave fractionation, but that this effect is not as strong as the equilibrium calculation would imply.

VIII. DISCUSSION OF RESULTS

A. Emission Source.

One conclusion of this study, that the bulk of the α-particles are evaporated from the fully accelerated DI fragments, is consistent with most of the published work for low energy HI reaction [for example: Ba 80, Ey 78, Hi 79, Ku 80, Pe 77]. However, for systems that are quite similar (in terms of energy over the Coulomb barrier, total mass and angular momentum) to $^{nat}Ag + ^{84}Kr$ at 664 MeV, several studies [Lo 80a, Lo 80b, Gu 81] have found a large prescission component. This apparent disagreement can almost be reconciled by one experimental difference between the published studies of Logan et al. and the studies reported in this thesis or the other studies mentioned above. In the coincidence work of Logan et al. a bias towards the detection of LPs in coincidence with fusion-fission events is introduced by the detection of the HI at angles much larger than the grazing angle. On the other hand, in the present work (and most others [Bu 80, Ey 78, and Hi 79]) a bias towards the detection of LPs on coincidence with DI events is introduced by the detection of the HI near or forward of the grazing angle. Since the lifetime of the compound nucleus is longer than that for the DI intermediate, one would expect a larger prescission component from the former.

The explanation of the difference in the experimental results must be more subtle than the one provided above. This is evident from the study of $^{197}Au + ^{63}Cu$ at 365 MeV [Pe 77] and the study of $^{nat}Ag + ^{86}Fe$ at 480 MeV [Gu 81]. In the former case most of the

neutrons detected in coincidence with a projectile-like fragment, detected far behind the grazing angle, were determined to be evaporated from the fully accelerated fragments. In the latter case, most of the α-particles detected in coincidence with a projectile-like fragment, detected near the grazing angle, were determined to be prescission. At the present time, the explanation of the different conclusions concerning the emission source of the bulk of the LPs is unclear.

It is not appropriate to dwell on the high energy component in the α-particle spectra, which is seen at forward angles, due to the rather meager data in the present study concerning these emissions. Nevertheless, a few comments are in order. Perhaps the most important comment is that the data for both the $^{nat}Ag + ^{84}Kr$ system and the $^{181}Ta + ^{165}Ho$ system are not inconsistent with a small admixture of emissions from the center of mass system Such emissions would be more forward focused and would have a larger average energy in the forward direction than emissions from the target recoil (for example, see Fig. V 4). Thus, a small admixture of evaporation of the composite system can greatly perturb the forward angle data. Since the data are insufficient to either prove or disprove the presence of this component one must at least consider non-equilibrium mechanisms.

Beginning with the work of Britt and Quinton [Br 61], numerous studies with light heavy ions (A < 40] have found an excess of energetic LPs in the forward direction that could not be attributed to compound nucleus decay. Recently, there has been some success in

explaining these LPs by an incomplete fusion or massive transfer mechanism [Si 79, In 77, Zo, 78, We 78, Su 78, In 79, Ya 79, and Wi 80]. However, this success does not extend to reactions with projectiles with $A \geq 40$ ($\geq ^{40}Ar$) where direct emissions do not become evident unless one is working near the energy limits of the present day non-relativistic Heavy-Ion accelerations. For example, the $^{166}Er + ^{86}Kr$ system has been studied at incident energies of both 602 MeV [Ey 78] and 1020 MeV [Ts 81]. At the lower energy no evidence for non-equilibrium neutron emission was found while at the higher energy (the present limit of the GSI l''''LAC) the data suggested a small (10%) non-equilibrium component. It is interesting to note that the ratios of the center of mass energy over the coulomb barrier ($E_{c.m.}/B_{coul}$) for these two energies bracket the value for the $^{nat}Ag + ^{86}Kr$ system at 664 MeV, ($E_{c.m.}/B_{coul} = 1.6$, 2.0, and 2.7 for the $^{166}Er + ^{86}Kr$ at 602 MeV, $^{nat}Ag + ^{84}Kr$ at 664 MeV, and $^{166}Er + ^{86}Kr$ at 1020 MeV, respectively.

B. Fragment Spins.

The results concerning angular momentum transfer for the $^{nat}Ag + ^{84}Kr$ reaction are summarized in Fig. VIII 1b. In the lower portion of this figure individual spins extracted from the α-particle distributions as described previously are shown (solid circles). Above this are plotted the sum of the spins of both fragments as determined by two independent methods. In the first method rigid rotation is invoked to determine the spin of the light fragment (I_L) from the value of I_H extracted from the out-of-plane

α-particle distributions. In the second method, the sum of the spins is derived from the M_γ data. The data presented in Fig. VIII 1b provide strong evidence that the lifetime of the intermediate complex is sufficient for the equilibrium limit of rigid rotation to be reached. This result is in agreement with the results for lighter systems. In addition, these data suggest an ℓ-wave fractionation effect for the largest mass asymmetries investigated, an effect predicted by diffusion model calculations.

It should be noted that large fragment deformations are needed in order to obtain quantitative agreement between the data and the rigid rotation calculations. Much stronger evidence for large deformation of the DI complex is derived from the fragment kinetic energies. The fragment energies for two equally deformed spheroids is given by

$$E_L = \frac{M_H}{M_L + M_H} \left(\frac{Z_L Z_H}{d} F + \frac{\ell_{rel}^2}{2\mu d^2} \right) \quad . \tag{24}$$

where the Coulomb correction factor (F), the distance between centers (d), and the relative angular momentum (ℓ_{rel}) are deformation dependent.

In Fig. VIII 1a the experimental fragment kinetic energies, corrected for evaporation, are compared to calculations for several deformations. The calculations are for equally deformed spheroids separated by 1 fm. In this model, a ratio of axes (C/A) of about 2 is needed to reproduce the data, indicating that the nuclei are substantially deformed. This result is supported by numerous studies

[Re 81, and references therein] involving nuclei in the region between
the magic numbers $Z = 40$ and $Z = 50$. These studies indicate that
these nuclei are quite soft and deform easily. In the work of Rehm et
al. this softness was used to explain the unusually large mass and
charge transfer in the system $^{208}Pb + ^{110}Pd$ at energies close to
the Coulomb barrier.

IX. SUMMARY

The in- and out-of-plane α-particle distributions in coincidence with deep-inelastic projectile-like fragments have been measured for the reactions $^{nat}Ag + {}^{84}Kr$ at 664 MeV and $^{181}Ta + {}^{165}Ho$ at 1354 MeV. At angles equal to or larger than the target recoil direction, the α-particle energy spectra and angular distributions are well described by evaporation from a fully accelerated target-like recoil nucleus.

In contrast to the isotropic in-plane distributions, the out-of-plane distributions are anisotropic and have been employed to investigate the relaxation of the angular momentum degrees of freedom. The results of the $^{181}Ta + {}^{165}Ho$ experiment corroborate the conclusions of previous γ-ray studies concerning the magnitude of the spin transferred to the fragments. Fragment spins as a function of mass asymmetry were extracted for the $^{nat}Ag + {}^{84}Kr$ system. These spins, along with those extracted from a simultaneous γ-ray multiplicity measurement, have been used to study the transfer of orbital angular momentum into intrinsic spin and its partitioning within the dinuclear complex. These data provide unambiguous evidence for rigid rotation of the intermediate complex. Furthermore, large deformations are indicated by three sources: fragment kinetic energies, spins extracted from the out-of-plane α-particle distributions, and those deduced from γ-ray multiplicity data.

APPENDIX A. LIGHT PARTICLE ANGULAR DISTRIBUTION

$$\text{WHEN } \Gamma_T = \Gamma_n + \Gamma_\alpha$$

The large Coulomb barriers for charged particle emission is very heavy ion reactions as well as the observed large neutron multiplicities, suggest that a reasonable first order approximation to the total decay width is,

$$\Gamma_T = \Gamma_n \qquad \bullet \qquad \qquad \text{A1.}$$

This assumption leads to the analytical result given in VI C and derived in Mo 81a. However, due to the high temperatures and large spins involved in deep-inelastic heavy ion reactions α-particle emission can become an important mode of decay. Thus a better estimate of the total decay width is,

$$\Gamma_T = \Gamma_n + \Gamma_\alpha \qquad \bullet \qquad \qquad \text{A2.}$$

Since the derivation of the angular distribution expression with this approximation has not as yet appeared in the literature, it will be reproduced here in detail.

Following Mo 75, the ratio of the α-particle decay width to the neutron decay width is

$$\frac{\Gamma_\alpha}{\Gamma_n} \approx \frac{1}{2} e^{-\left(BE_\alpha + CB_\alpha - BE_n\right)/T} e^{-\left(RE_\alpha - RE_n\right)/T} \qquad . \qquad \text{A3.}$$

where

BE_α = The α-particle binding energy

CB_α = The Coulomb barrier for α-particle emission

BE_n = The neutron binding energy

RE_α = The rotational energy at the critical shape for α-decay

RE_n = The rotational energy at the critical shape for neutron
   decay

T   = The nuclear temperature.

Expression A3 can be rewritten as,

$$\frac{\Gamma_\alpha(I)}{\Gamma_n(I)} = A\ e^{\frac{-I^2}{2T}\left(\frac{1}{\mathcal{J}_\perp} - \frac{1}{\mathcal{J}_n}\right)} = \Delta\ e^{I^2\beta} \qquad\qquad A4.$$

In this expression Δ is given by, ****

$$\Delta = \frac{1}{2}\ e^{-(BE_\alpha + CB_\alpha - BE_n)/T} \qquad . \qquad\qquad A5.$$

The parameter that accounts for the charge in the relative decay widths as a function of angular momentum is β and expressed in terms of the relevant moments of inertia is,

$$\beta = \frac{1}{2T}\left(\frac{1}{\mathcal{J}_n} - \frac{\cdot}{\mathcal{J}_\perp}\right) \qquad \text{where}$$

$\mathcal{A}_{\perp}$ = the moment of inertia perpendicular to the decay axis for the critical shape for α-particle decay (see Fig. VI 5) and

$\mathcal{A}_n$ = the moment of inertia of the daughter nucleus after neutron decay.

Including the angular dependence for α-particle decay (Eq. 8)

$$\frac{\Gamma_\alpha(I,\theta,\phi)}{\Gamma_n(I)} \propto \frac{\frac{1}{S(\theta,\phi)} e^{-\frac{I^2}{2T}\left(\frac{1}{\mathcal{A}_\perp} - \frac{1}{\mathcal{A}_c}\right)_e} e^{-(I^2\cos^2\theta)/2S^2(\theta,\phi)}}{e^{-\frac{I^2}{2T}\left(\frac{1}{\mathcal{A}_n} - \frac{1}{\mathcal{A}_c}\right)}}$$

$$\propto \frac{1}{S(\theta,\phi)} e^{-(I^2\cos^2\theta)/2S^2(\theta,\phi)} e^{I^2\beta} \qquad\qquad \text{A6.}$$

In general S is a function of the polar and azimuthal angles θ and ϕ, however these dependencies are lost when the variances σ_x, σ_y and σ_z are all equal, see Section VI B. For the sake of readability these dependencies will not be explicitly indicated.

Using A4 and A6 we have,

$$\frac{\Gamma_\alpha(I,\theta,\phi)}{\Gamma_n(I) + \Gamma_\alpha(I)} = \frac{\Gamma_\alpha(I,\theta,\phi)/\Gamma_n(I)}{1 + \Gamma_\alpha(I)/\Gamma_n(I)} \qquad\qquad \text{A7.}$$

$$\propto \frac{1}{S} \frac{e^{-(I^2\cos^2\theta)/2S^2} e^{I^2\beta}}{\left[1 + \Delta\, e^{I^2\beta}\right]} \qquad\qquad .$$

The angular distribution is then given by (see Eq. 10),

$$\omega\ (\theta,\phi) \propto \int_{\frac{1}{S}_{min}}^{I_{max}} \left(2Ie^{-(I^2\cos^2\theta)/2S^2}\ e\ I^2\beta\right) \Big/ \left(1 + {_\Delta e}^{I^2\beta}\right)\ dI,$$

$$\propto \frac{1}{S} \int_{I_{min}}^{I_{max}} \frac{I\ e^{-I^2A}}{\left(1 + {_\Delta e}^{I^2\beta}\right)}\ dI \qquad A8.$$

where $A = \dfrac{\cos^2\theta}{2S^2} - \beta$.

Integrating expression A8 by parts yields,

$$\omega(\theta,\phi) \propto \frac{1}{S} \left\{ \frac{-e^{-I^2A}}{2\beta}\ \ln\ \left(e^{-I^2\beta} + {_\Delta}\right)\Big/_{I_{min}}^{I_{max}} \qquad A9. \right.$$
$$\left. \int \frac{IA}{\beta}\ e^{-I^2A}\ \ln\ \left(e^{-I^2\beta} + {_\Delta}\right)\ dI \right\}$$

Part of the integral in expression A9 can be integrated to yield

$$\omega(\theta,\phi) \propto \frac{1}{S} \left\{ \left[\frac{-e^{-I^2A}}{2\beta}\ \ln\ \left(e^{-I^2\beta} + {_\Delta}\right)\ - \frac{1}{2}\frac{e^{-AI^2}}{A}\ (1 - AI^2)\right]\Big/_{I_{min}}^{I_{max}} \right.$$
$$\left. -\int \frac{AI}{\beta}\ e^{I^2A}\ \ln\ \left(1 + {_\Delta e}^{BI^2}\right)dI \right\}$$

The remaining integral can be solved by making an expansion about small Δ and integrating the expansion term by term.

$$\omega(\theta,\phi) \propto - \frac{e^{-I^2 A}}{S} \left\{ \frac{\ln(e^{-I^2 \beta} + \Delta)}{2\beta} + \frac{I^2}{2} + \frac{1}{2A} + \frac{A}{\beta} \sum \frac{(-\Delta)^n e^{-I^2 n\beta}}{2n(A - n\beta)} \right\} \Bigg/ \begin{matrix} I_{max} \\ \\ I_{min} \end{matrix}$$

In the limit of no α-particle emission ($\Delta \to o$) this expression reduces to,

$$\omega(\theta,\phi) \propto - \frac{e^{-I^2 A}}{SA} \Bigg/ \begin{matrix} I_{max} \\ \\ I_{min} \end{matrix}$$

which is the same as that derived previously (Mo 81a and Eq. 13) for the case where $\Gamma_T \approx \Gamma_n$.

-72-

ACKNOWLEDGMENTS

During my graduate student years at Berkeley I have had the
pleasure of working with many excellent scientists. It would be
enough to have to thank these individuals for the scientific knowledge
that they have fed me, but I also have received sustenance from our
close and hopefully lasting friendships.

Among these individuals Professor Luciano Moretto deserves
special thanks, not only for his persevering guidance over my graduate
career but also for his extemporanous lessons on everything from
Tacitus to my native language.

Dr. Gordon Wozniak also deserves special mention for his
instruction in experimental Nuclear Physics which included teaching,
by example, the semi-infinite patience needed to debug our experiments.

I also need to acknowledge Dr. Chin Chan Hsu, for we collaborated
on much of the work reported in this thesis. It was his finely tuned
sense of humor that oiled the collaboration. I would also like to
mention Mr. Jim Hunter, Dr. Rick Schmitt, Dr. Dick McDonald, Mr.
Alberto Pacheco and Prof. Dave Morrissey for their help in various
phases in the work reported in this thesis as well as enricning my
graduate student years with their friendship.

FOOTNOTES

* The "out-of-plane" notation at first may appear confusing but is actually quite simple. The true out-of-plane angle is either θ_L or θ_{RF} for the laboratory and target recoil rest frames, respectively. Similarly, the angle from the normal is either θ'_L, θ'_{RF}, or just θ' (used throughout the formalism section when the correct rest frame is assumed).

** Due to the angular distributions of stretched E2 and E1 γ radiation, to obtain the maximum bias of the spin distribution it is desirable to place γ-ray multiplicity detector array in the reaction plane. Unfortunately, experimental limitations did not allow us to get any closer to the reaction plane than 45°. However, at any angle, the requirements of a large number of coincident γ rays should bias the fragment's spin distribution towards large values.

*** It turns out that the extracted spin values are quite insensitive to I_{min}. The spins extracted using the procedure to calculate I_{min} described in the text and those extracted with $I_{min} = 0$ are equal within statistical error.

**** If the Weisskopf [We 37] formulation of the particle decay width is used the only difference is a constant factor in the expression for Δ.

REFERENCES

Al 75   R. Albrecht, W. Dunnweber, G. Graw, H. Ho, S.G. Steadman, and J.P. Wurm, Phys. Rev. Lett. $\underline{34}$, 1400 (1975).

Al 78   M.M. Aleonard, G.J. Wozniak, P. Glassel, M.A. Deleplanque, R.M. Diamond, L.G. Moretto, R.P. Schmitt, and F.S. Stephens, Phys. Rev. Lett. $\underline{40}$, 622 (1978).

Al 81   J. M. Alexander, private communication.

Ba 78   B. B. Back and S. Bjornholm, Nucl. Phys. $\underline{A302}$, 343 (1978).

Ba 80   R. Babinet, B. Cauvin, J. Girard, J.M. Alexander, T.H. Chiang, J. Galin, B. Gatty, D. Guerreau, and X. Tarrago, Z. Physik $\underline{A295}$, 153 (1980).

Bl 81   S.K. Blau and L.G. Moretto, Nucl. Phys. $\underline{A359}$, 477 (1981).

Bo 77   R. Bock, B. Fischer, A. Gobbi, K. Hildenbrand, W. Kohl, U. Lynen, I. Rode, H. Stelzer, G. Auger, J. Galin, J. M. Lagrange, B. B. Back, and R. Albrecht, Noklionika $\underline{22}$ 529 (1977).

Br 61   H. Britt and A. R. Quinton, Phys. Rev. $\underline{124}$, 877 (1961).

Br 76   H.C. Britt, B.H. Erkkila, P.D. Goldstone, R.H. Stokes, F. Plasil, R.L. Ferguson, and H.H. Gutbrod, Proceedings of the Symposium on Macroscopic Features of Heavy-Ion Collisions, Report ANL/PHY 76-2, 1976 (unpublished), p. 491.

Br 79   R.A. Broglia, G. Pollarolo, C.H. Dasso, and T. Dossing, Phys. Rev. Lett. $\underline{43}$, 1649 (1979).

Ca 80   C.L. Catchen, M. Kaplan, J.M. Alexander and M.F. Rivet, Phys. Rev. $\underline{C21}$, 940 (1980).

Ch 80   P.R. Christensen, F. Folkmann, Ole Hansen, O. Nathan,
         N. Trautner, V. Videbaek, S.Y. Van Der Werf, H.C. Britt,
         R.P. Chestnut, H. Freiesleben and F. Puhlhofer, Nucl. Phys.
         A349, 217 (1980).

Dø   T. Døssing, unpublished.

Dy 79   P. Dyer, R.J. Puigh, R. Vandenbosch, T.D. Thomas, M.S.
         Zisman, and L. Nunnelley, Nucl. Phys. A322, 205 (1979).

Er 58   T. Ericson and V. Strutinski, Nucl. Phys. 8, 284 (1958).

Ey 78   Y. Eyal, A. Gavron, I. Tserruya, Z. Fraenkel, Y. Eisen,
         S. Wald, R. Bass, G. R. Gould, G. Kreyling, R. Renfordt,
         K. Stelzer, R. Zitzmann, A. Gobbi, U. Lynen, H. Stelzer,
         I. Rode, and R. Bock, Phys. Rev. Lett. 41, 625 (1978).

Fo 74   M. Fowler and R.C. Jared, Nucl. Instr. Meth. 124, 341 (1974).

Ga 75   B. Gatty, D. Guerreau, M. Lefort, X. Tarrayo, J. Galin,
         B. Cauvin, J. Girard, and H. Nifenecker, Nucl. Phys. A253,
         511 (1975).

Ga 76   J. Galin, B. Gatty, D. Guerreau, M. Lefort, X. Tarrayo,
         R. Babinet, B. Gauvin, J. Girard, and H. Nifenecker,
         Z. Physik A278, 347 (1976).

Ge 79   C. Gerschel, M.A. Deleplanque, M. Ishihara, C. Ngo,
         N. Perrin, J. Peter, B. Tamain, L. Valentin, D. Paya,
         Y. Sugiyama, M. Berlanger, and F. Hanappe, Nucl. Phys. A317,
         473 (1979). .

Gl 41   S. Glasstone, K. J. Laialer, and H. Eyring, The Theory of
         Rate Processes, McGraw-Hill, New York, 1941.

Gl 77   P. Glässel, R.S. Simon, R.M. Diamond, R.C. Jared, I.Y. Lee,
        L.G. Moretto, J.O. Newton, R. Schmitt, and F.S. Stephens,
        Phys. Rev. Lett. 38, 331 (1977).

Gu 81   D. Guerreau, D. Logan, M. S. Zisman, J. M. Alexander, E.
        Duek, and M. Kaplan, preprint 1981.

Ha 58   I. Halpern, V.M. Strutinsky, Proc. U.N. Int. Conf. Peaceful
        Uses At. Energy, 2nd, 15 p. 408, pl 1513. United Nations,
        New York (1958).

Ha 79   D.V. Harrach, P. Glässel, Y. Civelekoglu, R. Manner, and
        H.J. Specht, Phys. Rev. Lett. 42, 1728 (1979).

Hi 79   D. Hilscher, J. R. Birkelund, A. D. Hoover, W. U. Schroder,
        W. W. Wilcke, R. J. Huizenga, A. C. Mignerey, K. L. Wolf, H.
        F. Breuer, and V. E. Violu, Jr., Phys. Rev. C20 576 (1979).

Ho 77   H. Ho, R. Albrecht, W. Dunnweber, G. Graw, S.G. Steadman,
        J.P. Wurm, D. Disdier, V. Rauch and F. Scheibling, Z. Physik
        A283, 235 (1977).

Hu 78   F. Hubert, A. Fleury, R. Bimbot, and D. Gardes, Report of
        the Institut de Physique Nucleaire Universite Paris-sud,
        IPNO-RC-7807 (1978).

In 77   T. Inamura, M. Ishihara, T. Fukuda, T. Shimoda, and
        H. Hirutu, Phys. Lett. 68B, 51 (1977).

In 79   T. Inamura, T. Kojima, T. Namura, T. Suyitate, and
        H. Utsunamiya, Phys. Lett. 84B, 71 (1979).

Kr 80   J.V. Kratz, W. Bruchle, H. Gaggeler, M. Schadel,
        K. Summerer, and G. Wirth, Z. Physic. A296, 141 (1980).

Ku 80   W. Kuhn, R. Albrecht, H. Damjantschitsch, H. Ho, R.M.
         Ronningen, J. Slemmer, J.P. Wurm, I. Rode, and
         F. Scheibling, Z. Physik A298, 95 (1980).

Le 78   M. Lefort and C. Ngô, Ann. Phys. (Paris) 3. 5 (1978).

Le 79   M. Lefort and C. Ngô, Rivista Del Nuovo Cimento 2, 1 (1979).

Le 81   C. LeBrun, J.F. Lecolley, F. Lefebvres, M. L'Haridon,
         A. Osmont, J.P. Patry, and J.C. Steckmeyer, and R. Chechick,
         6th Session d'etudes Biennale de Physique Nucleaire, Aussis,
         France, 2-6 Feb. 1981.

Lo 80a   D. Logan, M. Rajagopalan, M.S. Zisman, J.M. Alexander,
         M. Kaplan, and L. Kowalski, Phys. Rev. C22, 104 (1980).

Lo 80b   D. Logan, H. Delagrange, M.F. Rivet, M. Rajagopalan, J.M.
         Alexander, M. Kaplan, M.S. Zisman, and E. Duek, Phys. Rev. C
         22, 1080 (1980).

McD 82   R. J. McDonald, A. J. Pacheco, G. J. Wozniak, H. H. Bolotin,
         L. G. Moretto, C. Schück, S. Shin, R. M. Diamond, and F. S.
         Stephens, Nucl. Phys. A373 (1982).

Mo 75   L.G. Moretto, Nucl. Phys. A247, 211 (1975).

Mo 76   L.G. Moretto and R. Schmitt, J. Phys. 37, (1976) C5-109 and
         references therein.

Mo 78a   J.B. Moulton, thesis, University of California at Berkeley,
         Lawrence Berkeley Laboratory report LBL-7717 (1978).

Mo 78b   J.B. Moulton, J.E. Stephenson, R.P. Schmitt, and G.J.
         Wozniak, Nucl. Inst. Meth. 157, 325 (1978).

Mo 80   L.G. Moretto and R.P. Schmitt, Phys. Rev. C21, 204 (1980).

Mo 81a   L.G. Moretto, S.K. Blau, and A.J. Pacheco, Nucl. Phys. A364,
         125 (1981).

Mo 81b   D. J. Morrissey and L. G. Moretto, Phys. Rev. C23, 1835
         (1981).

Mo 81c   L. G. Moretto and R. P. Schmitt, Rep. Pro. Phys. 44, 533
         (1981).

Mo 82   D. J. Morrissey et al., to be published.

Na 79   M.N. Namboodiri, J.B. Natowitz, P. Kasiraj, R. Eggers,
         L. Adler, P. Gonthier, C. Cerruti, and S. Simon, Phys. Rev.
         C20, 982 (1979).

Ol 78   A. Olmi, H. Sann, D. Pelte, Y. Eyal, A. Gobbi, W. Kohl,
         U. Lynen, G. Rudolf, H. Stelzer, and R. Bock, Phys. Rev.
         Lett. 41, 688 (1978).

Pe 77   J. Peter, M. Berlanger, C. Ngô, B. Tamain, B. Lucas,
         C. Mazur, M. Ribrag, and C. Signarbieux, Z. Phys. A283, 413
         (1977).

Pu 79   R. J. Puigh, P. Dyer, R. Vandenbosch, T. D. Thomas,
         L. Nunnelley, and M. S. Zisman, Phys. Lett. 86B, 24 (1979).

Ra 79   M. Rajagopalan, L. Kowalski, D. Logan, M. Kaplan, J.M.
         Alexander, M.S. Zisman, and J.M. Miller, Phys. Rev. C19, 54
         (1979).

Ra 80   G.U. Rattazzi, R.P. Schmitt, G.J. Wozniak, and L.G. Moretto,
         Lawrence Berkeley Laboratory Report LBL-9711, 130 (1980)
         unpublished.

Re 78   R. Regimbart, A.N. Bekami, G.J. Wozniak, R.P. Schmitt, J.S.
         Sventek, and L.G. Moretto, Phys. Rev. Lett. 41, 1355 (1978).

Re 81   K. E. Rehm, H. Essel, P. Sperr, K. Hartel, P. Kienle, H. J.
         Korner, R. E. Segel, and W. Wagner, Nuc. Phys. A366 477
         (1981).

Ri 80   L.W. Richardson, G.J. Wozniak, M.R. Maier, and L.G. Moretto,
         Nucl. Instr. and Meth. 173, 485 (1980).

Ri 81   M. F. Rivet, D. Logan, J. M. Alexander, E. Duek, M. S.
         Zisman, and M. Kaplan, preprint (1981).

Sa 76   D. G. Sarantites, J. H. Barker, M. L. Halbert, D. C.
         Hensley, R. A. Dayras, E. Eichler, N. R. Johnson, and S. A.
         Gronemeyer, Phys. Rev. C14, 2138 (1976).

Sa 78   D.G. Sarantites, L. Westerberg, M.L. Halbert, R.A. Dayras,
         D.C. Hensley, and J.H. Barker, Phys. Rev. C18, 774 (1978).

Sc 77   W.U. Schroder and J.R. Huizenga, Ann. Rev. Nucl. Sci. 27,
         465 (1977), and references therein.

Sc 78a   R.P. Schmitt, thesis, University of California at Berkeley
         (1978), Lawrence Berkeley Laboratory report LBL-7168 (1978).

Sc 78b   R.P. Schmitt, P. Russo, R. Babinet, R. Jared, and L.G.
         Moretto, Nucl. Phys. A279, 141 (1976).

Sc 80   R. P. Schmitt, private communication.

Sc 82   R. P. Schmitt and A. J. Pacheco, Nucl. Phys. In press.

Si 79   K. Siwek-Wilczynska, E.H. duMarchie van Voorthuysen, J. van
         Popta, R.H. Siemssen, and J. Wilczynski, Phys. Rev. Lett.
         42, 1599 (1979).

So 81a   L.G. Sobotka, C.C. Hsu, G.J. Wozniak, D. J. Morrissey, and
          L.G. Moretto; Nuc. Phys. A371 510 (1981).

So 81b   L.G. Sobotka, G.J. Wozniak, R.J. McDonald, and L.G. Moretto,
          Lawrence Berkeley Laboratory report LBL-13366 (1981).

St 79   F.S. Stephens, Lawrence Berkeley Laboratory report
          LBL-10356, published in the Proceedings of the Varenna
          Conference, Varenna, Italy (1979).

Ts 81   I. Tserruya, A. Breskin, R. Chechik, Z. Fraenkel, C. Wald,
          R. Bock, M. Dakowski, A. Gobbi, H. Sann, R. Basę.
          G. Kreyling, R. Renfordt, K. Stelzer, and U. Arlt, Bull. Am.
          Phys. Soc. 8 1123 (1981).

We 37   V. Weisskopf, Phys. Rev. 52, 295 (1937).

We 78   L. Westerberg, D.G. Sarantites, D.C. Hensley, R.A. Dayras,
          M.L. Halbert, and J.H. Barker, Phys. Rev. C18, 796 (1978).

Wi 73   J. Wilczynski, Phys. Lett. 47B, 484 (1973).

Wi 80   J. Wilczynski, K. Siwek-Wilczynska, J. van Driel,
          S. Gonggrijp, D.C.J.M. Hagemann, R.V.F. Janssens, J.
          Lukasiak, and R.H. Siemssen, Phys. Rev. Lett. 45, 606 (1980).

Wo 78   G.J. Wozniak, R.P. Schmitt, P. Glassel, R.C. Jared,
          G. Bizard, and L.G. Moretto, Phys. Rev. Lett. 40, 1436
          (1978).

Ya 79   H. Yamada, D.R. Zolnowski, S.E. Cala, A.C. Kahler,
          J. Pierce, and T.T. Sugihara, Phys. Rev. Lett. 43, 605
          (1979).

Zn 78   D.R. Zolnowski, H. Yamada, S.E. Cala, A.C. Kahler, and T.T.
          Sugihara, Phys. Rev. Lett. 41, 92 (1978).

Table 1.

Parameters of the Reaction

$$^{181}_{73}\text{Ta} + {}^{165}_{67}\text{Ho} \text{ at 1354 MeV}^*$$

C.M. Energy		708.	(MeV)
Coulomb Energy		450.	(MeV)
$E_{c.m.}/B_{coul}$		1.6	
Lab. Grazing Angles (θ_{gr})	projectile	29.	(deg.)
	target	62.	(deg.)
ℓ_{max}		513.	($\hbar$)
ℓ_{rms}		362.	($\hbar$)
Mass Asymmetry $\dfrac{M_H}{M_H + M_L}$		0.52	
Moment of Inertia ratio $\dfrac{\mathcal{J}_H}{\mathcal{J}_L + \mathcal{J}_H}$		0.54	

* These values were calculated assuming spherical fragments where the

distance between fragment centers is given by:

1.225 $(A_L^{1/3} + A_H^{1/3})$ + 2 fm.

Table 2.

Parameters of the Reaction

$$^{nat}_{47}Ag + {}^{84}_{36}Kr \text{ at 664 MeV}^{\star}$$

CM Energy		373.	(MeV)
Coulomb Energy		185.	(MeV)
$E_{c.m.}/B_{coul}$		2.0	
Lab. Grazing Angles (θgr)	projectile	22.	(deg.)
	target	70.	(deg.)
ℓmax		274.	(h)
ℓrms		194.	(h)
Mass Asymmetry $\dfrac{M_H}{M_L + M_H}$		0.56	
Moment of Inertia ratio $\dfrac{\mathscr{I}_H}{\mathscr{I}_L + \mathscr{I}_H}$		0.60	

* These values were calculated assuming spherical fragments where

the distance between fragment centers is given by:

1.225 $(A_L{}^{1/3} + A_H{}^{1/3})$ + 2 fm.

Table 3.

181   165
Ta +   Ho (1354 MeV)
Coincidence Data

In-plane				Out-of-plane		
Angle ϕ_L/θ_L (deg)	Absorber material (mg/cm^2)	Solid angle (msr)		Angle ϕ_L/θ_L (deg)	Absorber material (mg/cm^2)	Solid angle (msr)
30./90.	Ta 8.2	5.8		55./90.	Ta 8.2	5.8
45./90.	Ta 9.1	5.8		55./75.	Ta 8.4	5.8
55./90.	Ta 8.2	5.8		55./60.	Ta 8.6	5.8
60./90.	Ta 8.6	5.8		55./45.	Ta 9.1	5.8
70./90.	Ta 8.2	5.8		55./30.	Ta 8.2	5.8
75./90.	Ta 8.4	5.8				
85./90.	Ta 9.1	5.8				
100./90.	Ta 8.6	5.8				
*105./90.	Ta 8.2	5.8				
115./90.	Ta 8.4	5.8				
*145./90.	Ta 8.2	5.8				

In-plane data from out-of-plane experimental runs.

* These data are subject to large errors due to the steep angle
  between the target and the detector and therefore, are not
  presented in this thesis.

Table 4.

$$\text{nat}_{Ag} + {}^{84}Kr \ (664 \ MeV)$$
Coincidence Data

	In-plane			Out-of-plane	
Angle Θ_L/ϕ_L (deg)	Absorber material (mg/cm^2)	Solid angle (msr)	Angle Θ_L/ϕ_L (deg)	Absorber material (mg/cm^2)	Solid angle (msr)
30.0/0.0	Ta 8.5	7.0	41.0/ 4.1	Ta 10.1	13.4
35.0/0.0	Ta 8.5	7.0	41.0/14.1	Ta 10.1	13.4
45.0/0.0	Ta 8.5	6.9	41.0/29.1	Ta 10.1	13.4
50.0/0.0	Ta 8.5	6.9	41.0/39.1	Ta 10.1	13.4
60.0/0.0	Ta 8.5	6.9	41.0/54.1	Ta 10.1	13.4
65.0/0.0	Ta 8.5	6.9	41.0/64.1	Ta 10.1	13.4
75.0/0.0	Au 4.6	6.7			
80.0/0.0	Au 4.6	6.7			
90.0/0.0	Au 1.0	6.6			
95.0/0.0	Au 1.0	6.6			

Table 5.

Z_L	Z_H	$I_H(\hbar)$					$I_L + I_L$ $(\hbar)$	
		a (1)	b (1)	c (2)	d (3)	e (4)	f (4)	g M_γ
26	67	39.8±0.9	27.3±0.6	29.6±0.7	28.4±0.3	29.2±0.2	36.8±0.3	38.7±2.0
29	54	38.0±0.6	26.5±0.4	28.9±0.5	27.7±0.2	28.5±0.3	38.2±0.5	39.9±2.0
32	51	33.7±0.6	24.1±0.4	26.6±0.4	25.4±0.2	26.2±0.2	37.7±0.4	40.8±2.0
35	48	30.3±0.5	22.1±0.4	24.6±0.4	23.6±0.2	24.3±0.2	38.0±0.4	39.2±2.0
38	45	26.3±0.5	19.4±0.4	22.0±0.4	21.0±0.2	21.5±0.2	37.8±0.4	35.4±2.0
41	42	21.4±0.7	16.2±0.5	18.6±0.6	17.9±0.2	18.3±0.2	36.1±0.4	36.7±2.0

a. Spherical K_0^2

b. Equilibrium K_0^2

c. Equilibrium K_0^2, misalignment

d. Equilibrium K_0^2, misalignment, integration over spin distribution with $\Gamma_T = \Gamma_n$

e. Same as d, but with $\Gamma_T = \Gamma_n + \Gamma_\alpha$

f. Calculated from column e assuming rigid rotation

g. Calculated from experimental gamma multiplicities

Figure Captions

Fig. III.1. The general relationships of the velocity vectors for
in-plane emission are shown. The measured quantities are
E_3^L, ϕ_3^L, (Z_3), E_5^L, ϕ_5^L, and Z_5, which are the
laboratory energy, angle, and charge (for the ^{84}Kr
experiments) of the projectile-like fragment and the
laboratory energy, angle, and charge of the light
particle, respectively.

Fig. III.2. Similar to Fig. III.1; however, the light particle
(subscript 5) is emitted out-of-plane with respect to the
plane containing the heavy ions and the beam direction.
The angles from the normal to the reaction plane
correspond to θ' in the text.

Fig. III.3. The correlation between the in- and out-of-plane angles
for the detection of a light particle in the lab system
(ϕ_L, θ_L) and the angles in the rest frame of the
moving source (ϕ_{RF}, θ_{RF}) is shown. The in-plane lab
angle is me sured from the recoil angle rather than the
beam direction. In this figure the velocity of the
moving source, the target-like fragment, is 1.44 cm/ns.
This was calculated from the kinetic energy or the
projectile-like fragment utilizing two body kinematics.
The velocity of the α-particle in the emittor's frame is
2.55 cm/ns, calculated from the expected most probable
emission energy.

Fig. III.4. Schematic view of the experimental setup. This figure depicts the Z-telescope, with its in-plane angle ϕ_Z; light particle telescopes with in- and out-of-plane lab angles ϕ_L and θ_L respectively; and the array of NaI detectors with an out-of-plane angle of $45°$.

Fig. III.5. High level Z-α-γ coincidence logic.

Fig. III.6. Low-level telescope logic indicating NIM electronics. BA/LS-biased amp and linear stretcher, CFD-constant fraction discriminator, FPO-fast pick off, GDG-gate and delay generator, LA-linear amp, LG-linear gate, MG-master gate, MPX-multiplexer input, SCA-single channel analyzer, SD-2^N scale down, TAC-time to amplitude converter.

Fig. III.7. Same as Fig. III.6 but for the NaI halo logic.

Fig. IV.1. Analysis flow chart for z-α-γ experiments. Each arrow (labeled by a lower case letter) represents a code that transforms the event-by-event data, in the form indicated in the box at the tail of the arrow, to the form indicated in the box at the tip of the arrow. The last step (i) is a sorting code that creates spectra.

Fig. IV.2. Delta E-E intensity map for fragments detected at 26° (lab) in the reaction $^{nat}Ag + ^{84}Kr$ at 664 MeV. The elastic and DI reaction products are clearly visible. Intensity bands for individual elements can be distinguished up to $Z \sim 40$.

Fig. IV.3. Same as Fig. IV.2 but for light particles. The strong Z
            = 2 band dominates the map. A faint Z = 3 band is also
            visible at larger ΔE values.

Fig. IV.4. Software generated ᵖarticle Identification spectrum (PI)
            for light particles emitted in the reaction ^{181}Ta +
            ^{165}Ho at 1354 MeV. The generating function is
            proportional to $(\Delta E/A + E)^P - E^P$ with A = 10.7, P =
            1.73, and ΔE and E are in channel numbers. The peaks
            corresponding to atomic numbers 1, 2, and 3 are indicated.

Fig. IV.5. Radiation damage in Si(Au) surface barrier detectors
            produced by various heavy ions. Detector number,
            voltage, and least squares fit of the rate of pulse
            height loss are indicated. The latter quantity is in
            units of pulse height/10^6 ions/cm^2.

Fig. IV.6. The energy of the detected fragment (E_3) and the
            calculated total kinetic energy (TKE) both before and
            after an evaporation correction. See the text for a
            description of the TKE calculation and the evaporation
            correction.

Fig. IV.7. Spectrum of the time of flight difference for the
            detection of a heavy ion (Z) and a light particle
            (usually an α-particle). The prompt peak is enhanced by
            more than a factor of 100 over the random coincidences
            between particles originating from different beam
            bursts. (The SuperHILAC microstructure has a 14 ns
            period.)

Fig. IV.8.   Same as Fig. I   but for coincidences between a heavy
              ion (Z) and a gamma ray (γ).

Fig. V.1.   a) Singles energy spectrum of heavy ions detected at 29°
              (lab) in the reaction ^{181}Ta + ^{165}Ho at 1354 MeV.   The
              EL and DI components are seen.

              b) Same as part a, but with the additional requirement
              that an α-particle be in coincidence with the heavy ion.
              Four Q-value gates are indicated. Region 1 corresponds
              to the elastic region and is predominantly random
              coincidences. The DI region is defined by the sum of
              regions 2, 3, and 4.

Fig. V.2.   In-plane coincident laboratory α-particle energy spectra
              for the ^{181}Ta + ^{165}Ho system. In-plane laboratory
              angles are indicated.

Fig. V.3.   Out-of-plane coincident laboratory α-particle energy
              spectra for the ^{181}Ta + ^{165}Ho system. Out-of-plane
              laboratory angles are indicated.

Fig. V.4   a) Velocity diagram for the ^{181}Ta + ^{165}Ho (1354 MeV)
              system. The open circles are the rms velocities
              extracted from the coincident laboratory α-particle
              energy spectra. The solid circles indicate the rms
              velocities of the two separate peaks that appear in the
              most forward data. The full large rings indicate the
              loci of expected α-particle velocities [Ri 81, Al 81] for
              the three different rest frames. For the target-like

fragment, the locus of velocities for a 10% reduction in the expected average emission energy is indicated by a partial ring. The detection threshold is shown as a dashed arc. The letters P and T stand for projectile-like and target-like, respectively.

b) The velocity diagrams for three different Q-bins (all in the deep-inelastic region). The rms α-particle velocities for each bin are indicated. The smallest energy loss bin is indicated by triangles (bin 2 in Fig. V.1b) and the largest energy loss data by squares (bin 4 in Fig. V.1b). The three partial rings are drawn to guide the eye. They have the same radius and are centered on the three different recoil velocities.

Fig. V.5.   For the ^{181}Ta + ^{165}Ho system, the α-particle energy spectra in the rest frame of the target-like fragment are shown. The dashed lines are drawn to guide the eye. The in-plane laboratory angles are provided for reference.

Fig. V.6.   a) In-plane α-particle angular distribution in the rest frame of the target-like fragment is shown for the ^{181}Ta + ^{165}Ho system. The distribution is given in differential multiplicity, see text. The in-plane angle of $\phi_{RF}=0°$ corresponds to the recoil direction with negative angles towards the beam. The open circle is the in-plane point for the out-of-plane distribution (see Fig. VI.2). The horizontal error bars are estimates of

the error in the angle between the target recoil fragment and the α-particle, due to the uncertainty in the primary mass of the detected heavy ion.

b) Average α-particle energies in the frame of the target recoil.

Fig. V.7   a) Singles charge distribution of projectile-like fragments detected at $\phi_Z = 26°$, in the reaction $^{nat}Ag + ^{84}Kr$ (664 Mev).

b) Singles total kinetic energy spectrum in the lab system integrated over the Z-values shown in part a. Also shown is the deep-inelastic gate (DI).

Fig. V.8   a) Singles alpha-particle energy spectra in the lab system for three representative in-plane angles, $^{nat}Ag + ^{84}Kr$ system (see text).

b) Coincidence alpha-particle energy spectra in the lab system for the same angles as part a, see text.

Fig. V.9   a) Singles α-particle angular distribution in the lab system for the $^{nat}Ag + ^{84}Kr$ system.

b) Coincidence in-plane α-particle angular distribution in the lab system.

Fig. V.10.   Same a; Fig. V.4a, but for the $^{nat}Ag + ^{84}Kr$ system.

Fig. V.11.   a) Intensity plot of the lab total kinetic energy vs charge of the projectile-like fragment for Z-α coincidence events in the $^{nat}Ag + ^{84}Kr$ system.

b) Intensity plot of the calculated lab recoil angle of the undetected fragment vs charge of the projectile-like fragment.

Fig. V.12.   Coincidence alpha-particle energy spectra in the rest frame of the target recoil for the $^{nat}Ag + ^{84}Kr$ system. Both in- and out-of-plane angles are shown.

Fig. V.13.   Alpha-particle energy spectra in the center-of-mass of the overall system for three in-plane angles for the $^{nat}Ag + ^{84}Kr$ system. These angles correspond to center-of-mass angles of 49°, 86° and 118°.

Fig. V.14.   Alpha-particle angular distributions in the rest frame of the target-like fragment in terms of the differential multiplicity. For this figure the charge of the projectile-like fragment satisfied the condition $26 \leq Z \leq 40$. The small contribution from the projectile-like fragment emission that is observed at forward angles (see Fig. V.12) has been subtracted.
a) In-plane distribution. The angle $\phi_{RF} = 0^O$ corresponds to the recoil lab direction. The dashed line is an average of the eight points for angles larger than the recoil direction.
b) Out-of-plane distribution. The solid line is a fit to the data (see chapter VI).

Fig. VI.1. The N-fold spectra. The peak at channel 40 corresponds
to scaled down 0-folds (HI singles events). The next 7
peaks are one folds (one peak for each of the seven
NaI's). The five peaks at channel numbers >250 peaks
with increasing channel numbers and decreasing intensity
correspond to the 2, 3, 4, 5 and 6 folds, respectively.

Fig. VI.2. Out-of-plane α-particle energy spectra in the rest frame
of the target-like fragment for the system ^{181}Ta +
^{165}Ho. The key indicates the out-of-plane and in-plane
laboratory angles as measured from the normal to the
reaction plane and from the beam, respectively. The
solid curves are the same for all spectra and are the
result of an evaporation calculation described in Chapter
VI. The dashed lines are drawn to guide the eye.

Fig. VI.3. The out-of-plane α-particle distribution for the
^{181}Ta + ^{165}Ho system. The size of the data points
indicates the magnitude of the statistical errors. The
solid line is a calculation, which is described in
chapter VI.

Fig. VI.4. The out-of-plane alpha-particle angular distributions for
the ^{nat}Ag + ^{84}Kr system as a function of out-of-plane
angle for several Z-bins. Each bin is 3 Z units wide and
is labeled by the median Z value. The distributions
without any coincidence γ-ray requirement a) are
expressed in units of differential multiplicity, whereas
the distributions with two or more coincident γ rays b)

are normalized to those in a) at 90° for the same Z bin.
The solid lines are fits to the data (see chapter VI).

Fig. VI.5.   Schematic of the critical decay shape for light particle
emission. The total angular momentum (I) and its
projection on the separation axis (K) are indicated. The
moments of inertia $\mathscr{I}_\perp$ and $\mathscr{I}_\parallel$ are those perpendicular and
parallel to the separation axis. In the present notation
the y axis is the separation axis. This is the most
common convention (for example Ba 78, Pu 79, and Mo 82).
However, the references Mo 75 and Mo 81a have employed
the opposite convention, that the x-axis coincides with
the recoil direction.

Fig. VI.6.   Comparisons among the data at 23°, 27°, and 31° as a
function of reaction Q-value for the ^{165}Ho + ^{165}Ho at
8.5 MeV/amu system [McD 81]. The top row represents
$M_\gamma(90°)$ (filled circles), $M_\gamma(0°)$ (open circles), and
the angle integrated γ-ray multiplicity $\langle M_\gamma \rangle$ for
$E_\gamma > 0.3$ MeV (solid line). The center row shows the
spin per fragment after neutron emission (solid line)
derived from $\langle M_\gamma \rangle$ and the spin prior to neutron
emission (dashed line). The bottom row shows the γ-ray
anisotropy for the region $0.6 < E_\gamma < 1.2$ MeV.

Fig. VI.7.   Spins extracted from the out-of-plane α-particle
            distributions (Fig. VI.3) with (open circles) and without
            (solid circles) the requirement of at least two
            coincident γ rays. Error bars are shown when they exceed
            the size of the symbol and indicate only the statistical
            error. The rigid rotation prediction for deformed
            spheroids with a ratio of axis of 2 and a separation of 1
            fm is shown by the solid line. The dashed line is a
            rigid rotation calculation including the effects of
            angular momentum fractionation, see text.

Fig. VII.1. The predictions for the sum of the spins ($I_1 + I_2$,
            solid lines) and an individual spin (I_1 dashed lines) as
            a function of mass asymmetry for both the rolling and
            rigid rotation limits. The calculation utilizes
            spherical rigid body moments of inertia. The arrow
            indicates the initial asymmetry in the $^{nat}Ag + ^{84}Kr$
            experiment.

Fig. VII.2. M_γ vs Z_3 for the DI component of the reactions ^{86}Kr
            + ^{165}Ho, and $^{86}Kr + ^{nat}Ag$. The solid lines
            correspond to the rigid rotation limit for two touching
            spheres. The dashed lines correspond to the rolling
            limit.

Fig. VII.3. Two perspectives of the potential energy surface for
            $^{56}Fe + ^{56}Fe$ with $0 \leq \ell \leq 50\hbar$. Spherical moments of
            inertia and rigid rotation are assumed.

Fig. VIII.1. a) Center-of-mass energies as a function of the charge of
the light fragment. The width of the symbols indicate
the uncertainty in the primary charge (before
evaporation). The curves are calculations for two
equally deformed spheroids separated by 1 fm and are
labeled by the ratio of axes. b) Plotted are: the spin
of the heavy fragment extracted from the α-particle
distributions (solid circles), the sum of spins
calculated from α-particle data (squares), and M_γ data
(open circles). The sizes of the solid symbols indicate
the statistical error only.
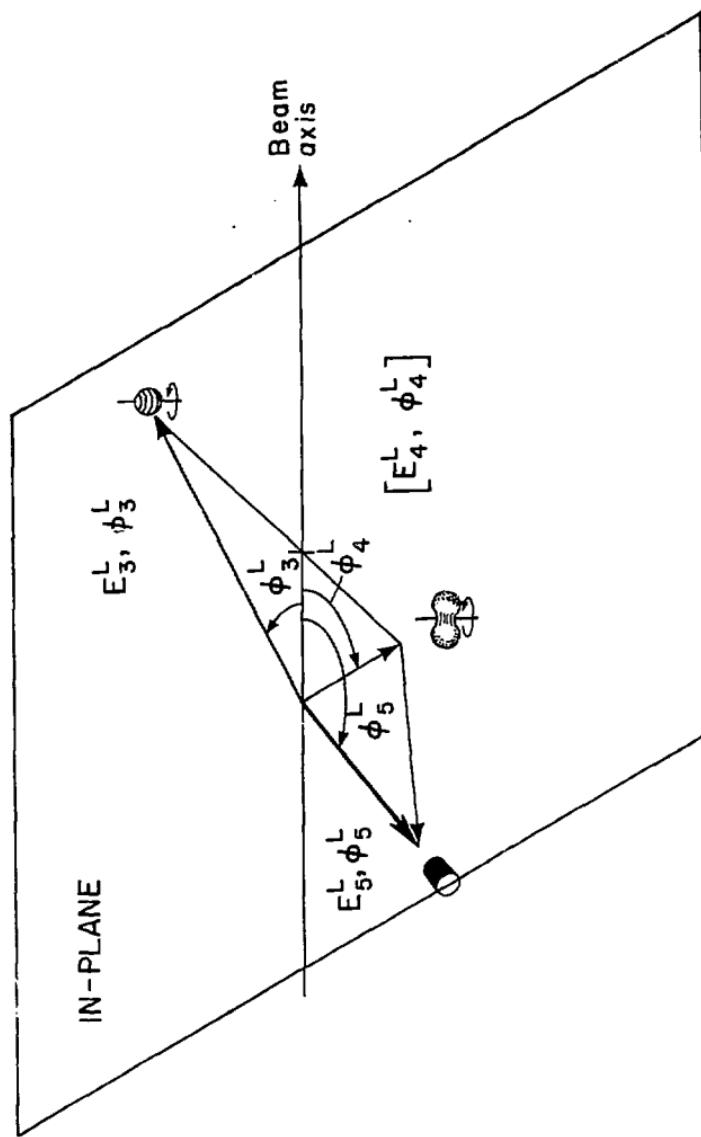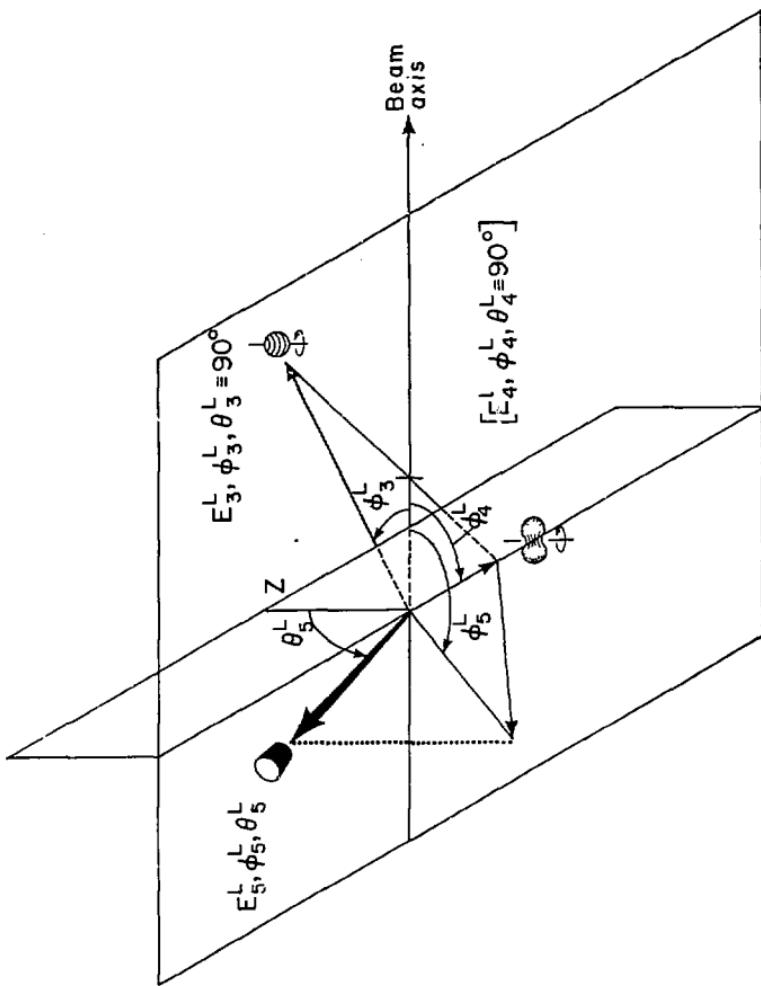
Fig. III.1

XBL-812-172

Fig. III.2

$^{nat}Ag + {}^{84}Kr$ (664 MeV)

θ_L (deg.)

ϕ_L from recoil (deg.)
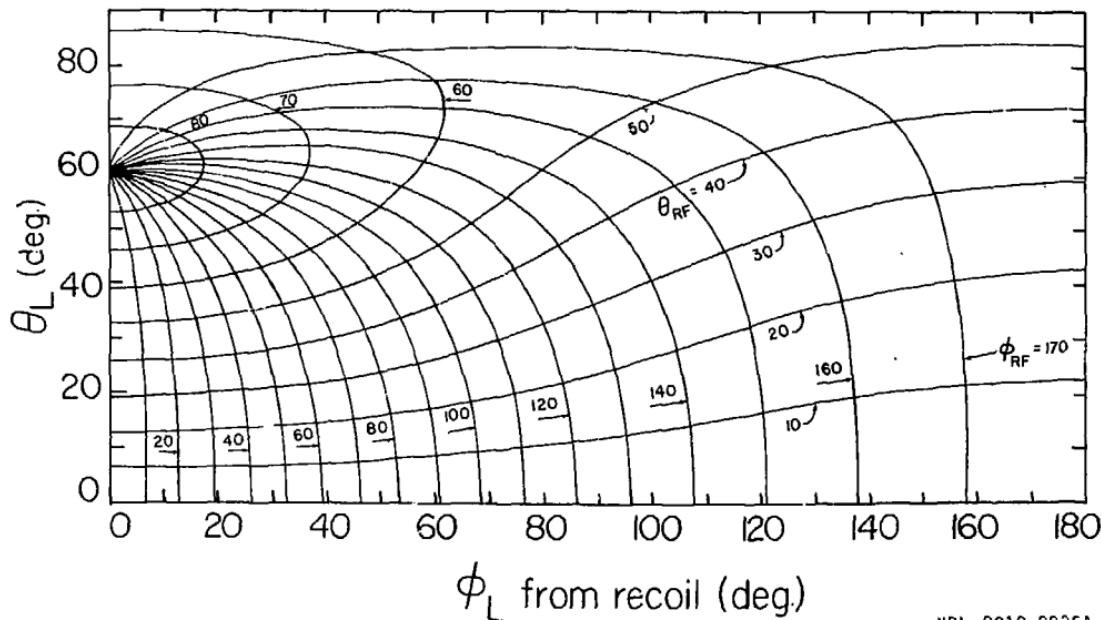
XBL 8010-2236A

Fig. III.3
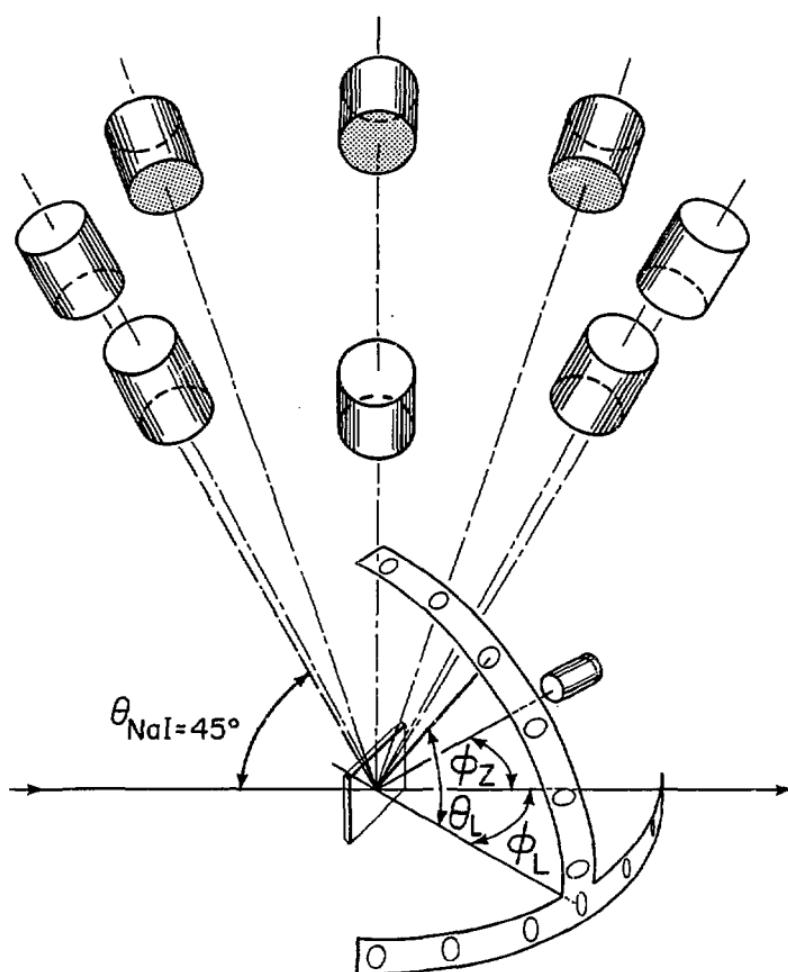
XBL 8010-2227A

Fig. III.4

Fig. III.5

XBL 218-2428A
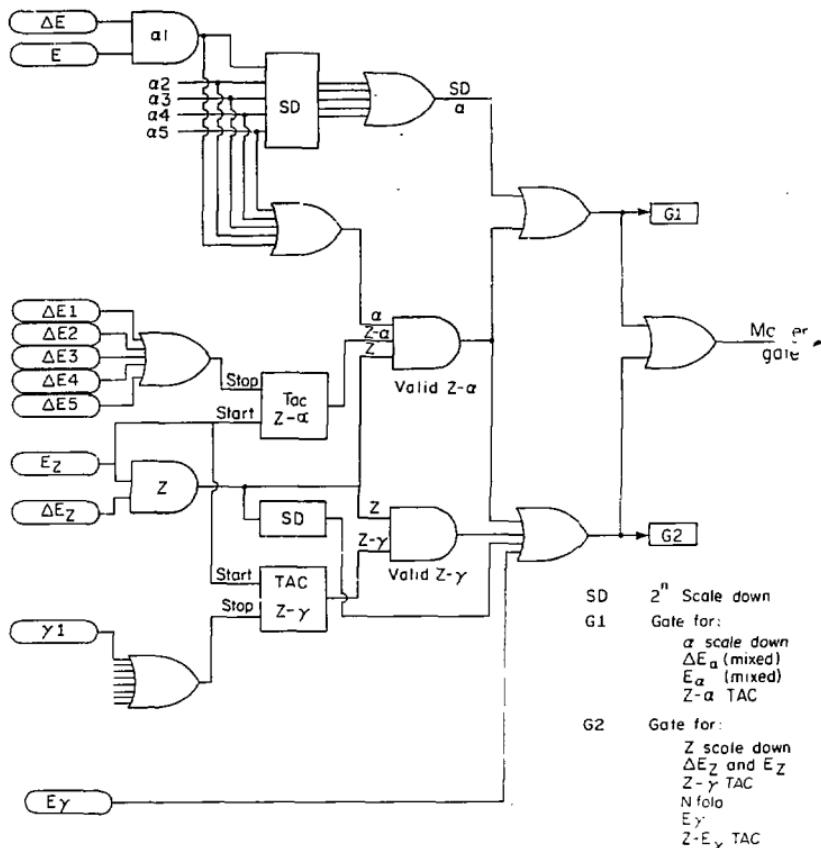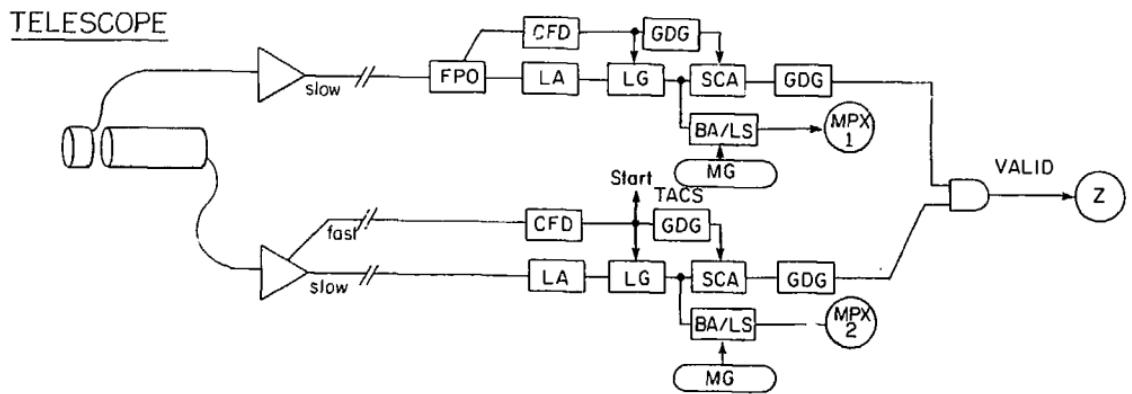
Fig. III.6

Fig. III.7
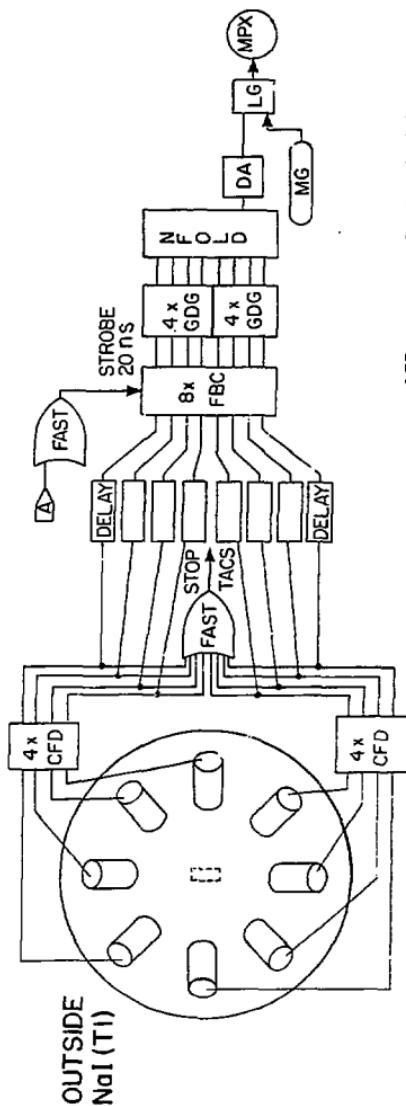
XBL 8012-2583A

CFD - constant fraction discriminator
DA - delay omp
FBC - fast binary coincidence
GDG - gate and delay generator
LG - linear gate
MPX - multiplexor input
A   - from particle logic

Analysis Flow Chart for
Z-α-γ Experiments[†]
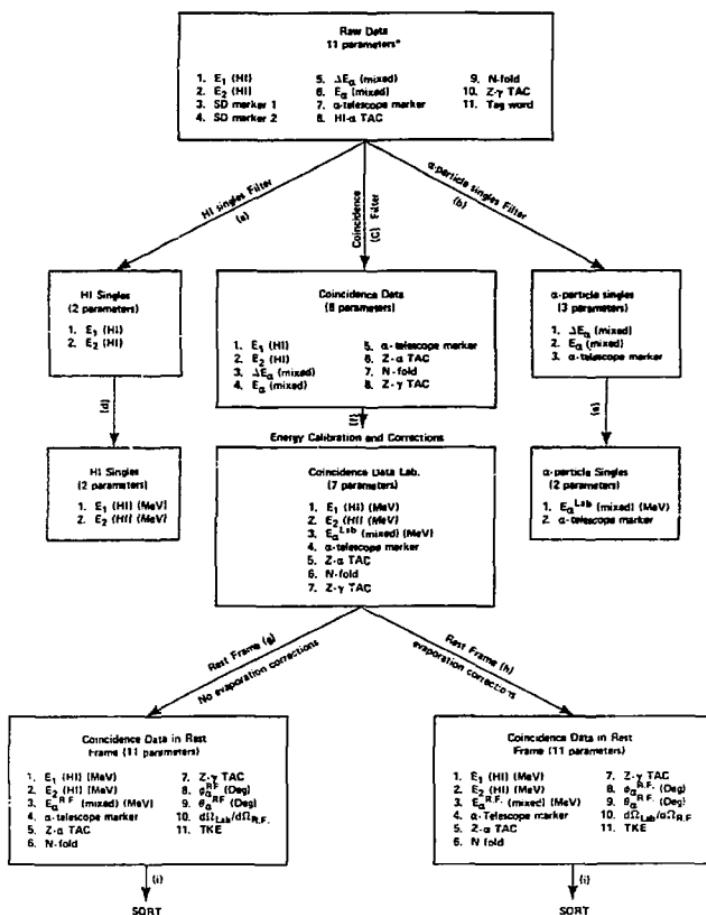
† This schema employed for ^{181}Ta + ^{165}Ho (1354 MeV) experiment.
* There were several additional parameters that were used to test a BGO
  detector. Since these parameters were not directly involved in the Z-α-γ
  experiment, they have been omitted from the flow chart.

XBL 819-2482

Fig. IV.1

^{nat}Ag + ^{84}Kr (664 MeV)

Fig. IV.2

XBL 812-2150

nat Ag + ^{84}Kr (664 MeV)

Li

α

E

ΔE

Fig. IV.3

XBL 812-2151
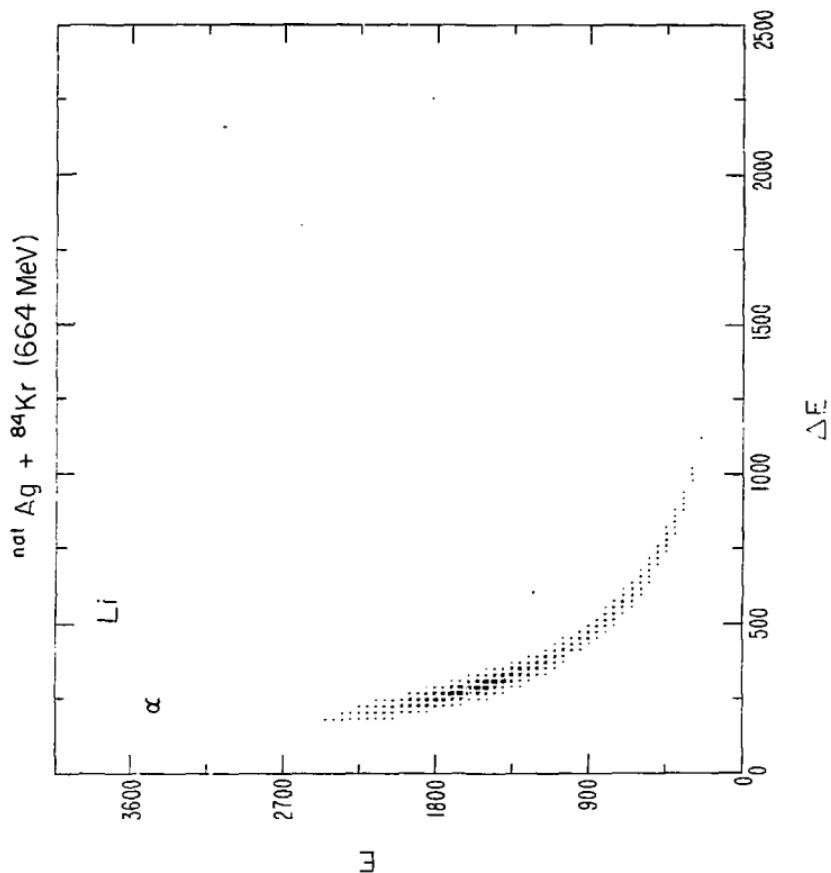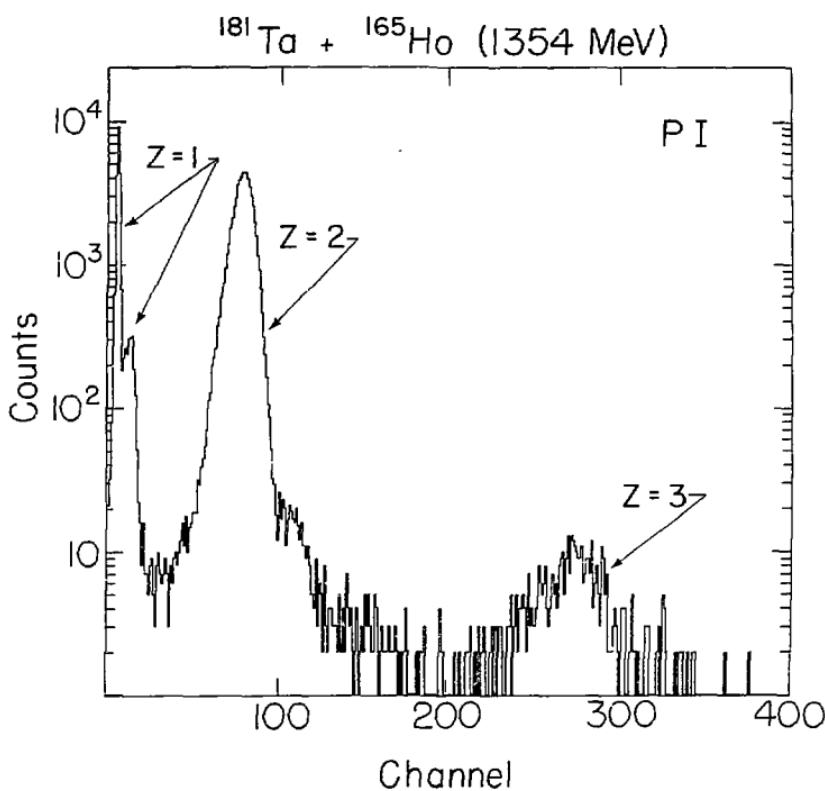
Fig. IV.4
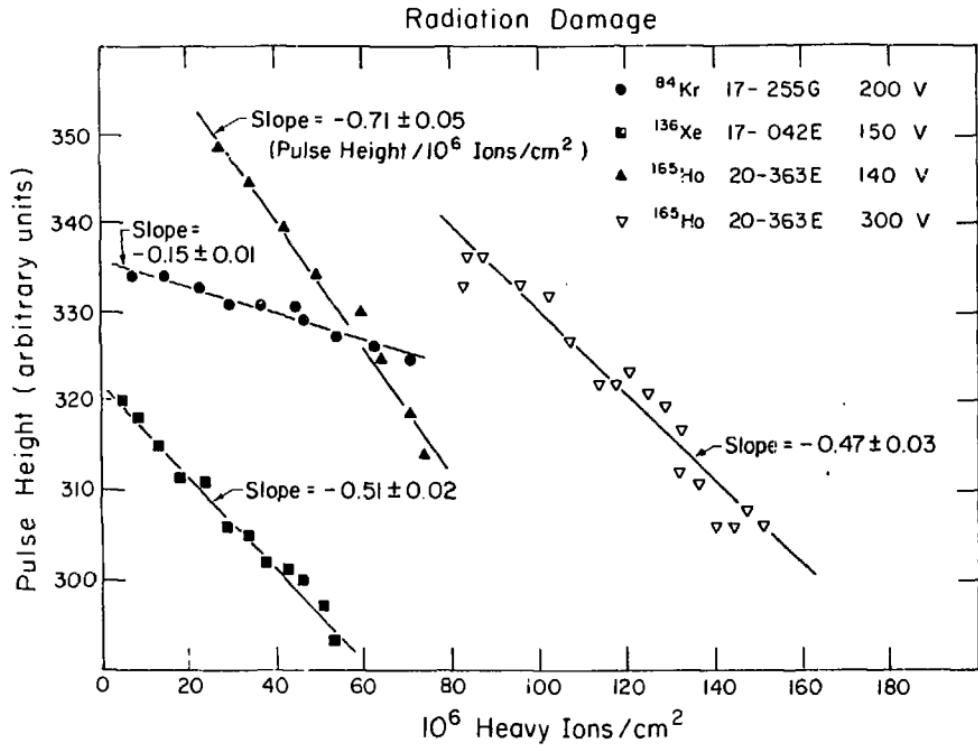
Fig. IV.5
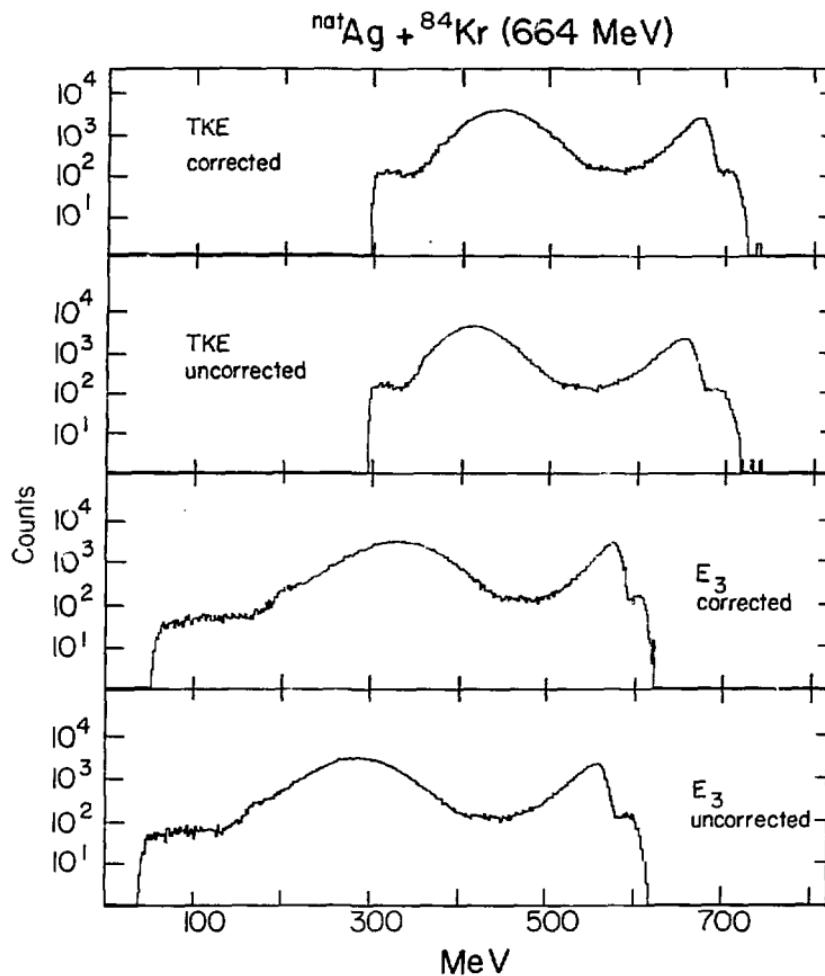
^{nat}Ag + ^{84}Kr (664 MeV)

XBL 8010-2232

Fig. IV.6

xBL822-4459

Fig. IV.7

Fig. IV.8

XBL 815-2299

^{181}Ta + ^{165}Ho (1354 MeV)

XBL 818-2457A

Fig. V.1

^{181}Ta + ^{165}Ho (1354 MeV)

30° (×10³)

45° (×10²)

60° (×10)

70° (×1)

75° (×10³)

85° (×10²)

100° (×10)

115° (×1)

$d^3\sigma/d\Omega_\alpha \, d\Omega_{HI} \, dE$ (arbitrary units)

E_α^{Lab} (MeV)

XBL 818-2462

Fig. V.2

^{181}Ta + ^{165}Ho (1354 MeV)

0°
(×10^4)

15°
(×10^3)

30°
(×10^2)

45°
(×10)

60°
(×1)

E_α^{Lab} (MeV)
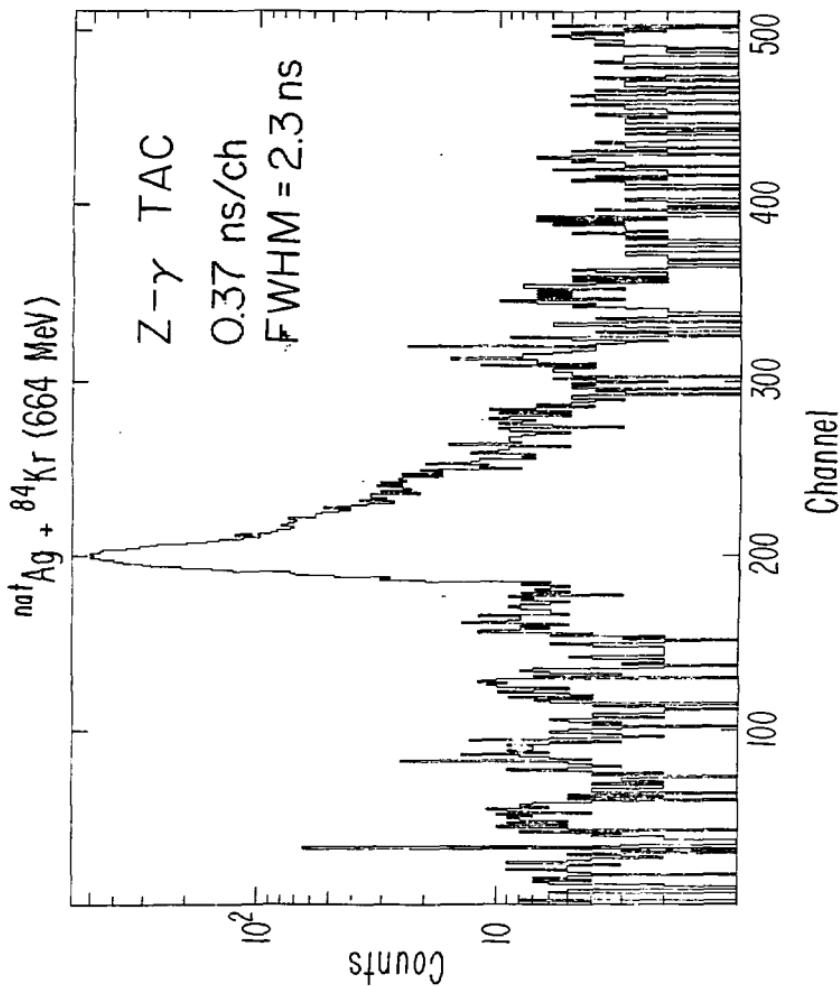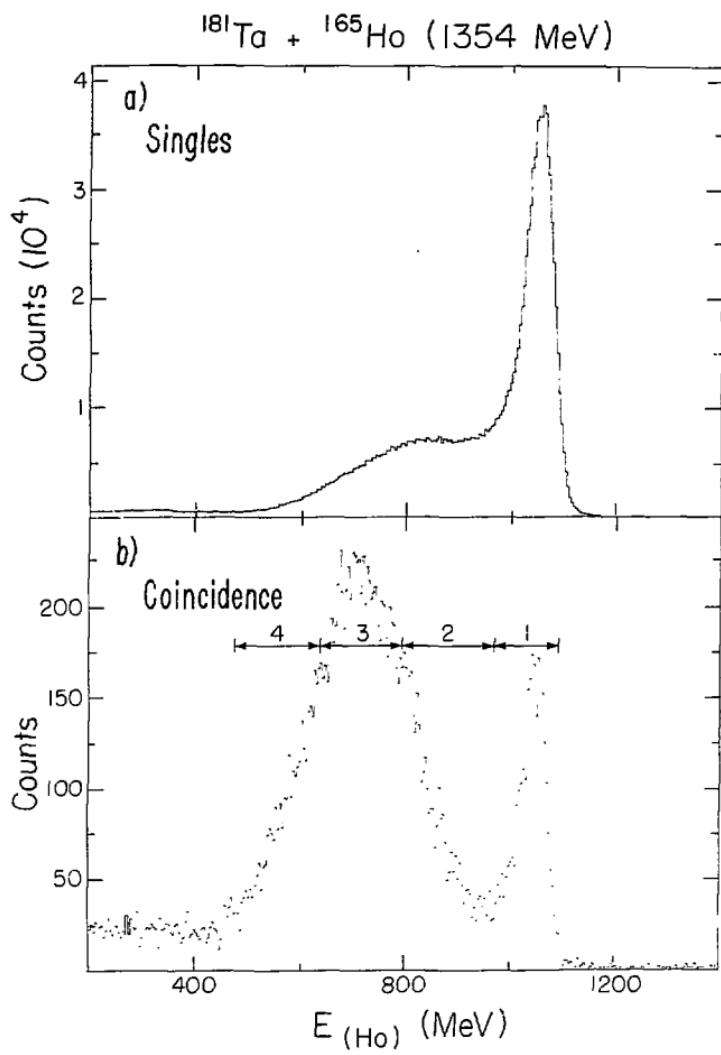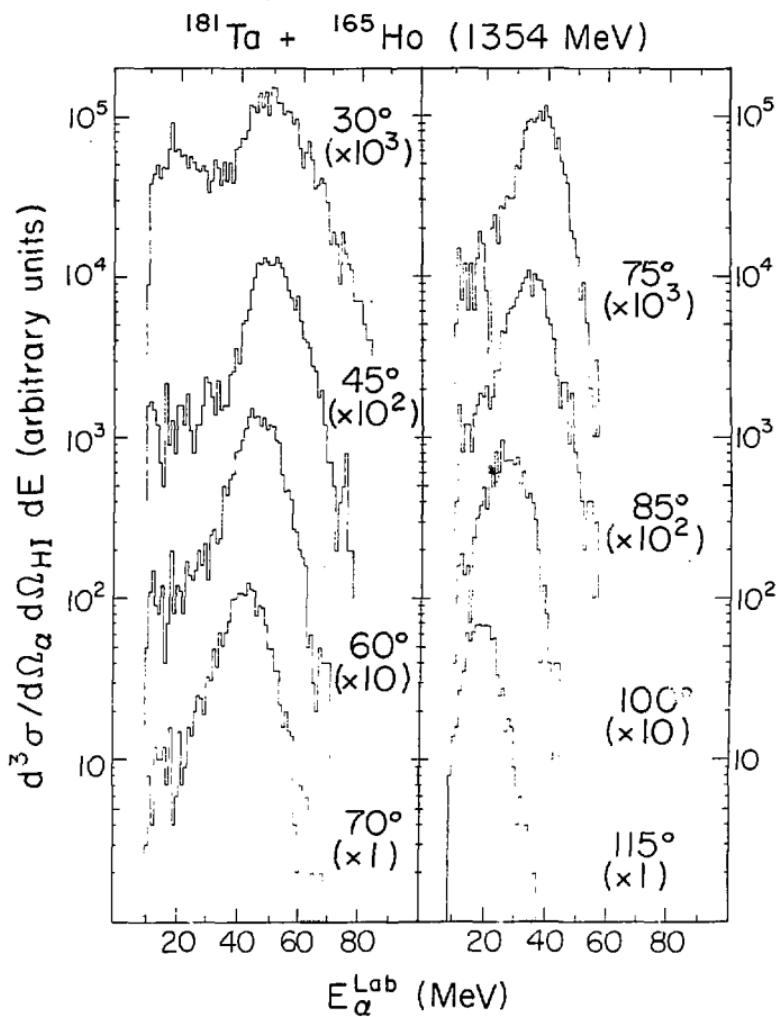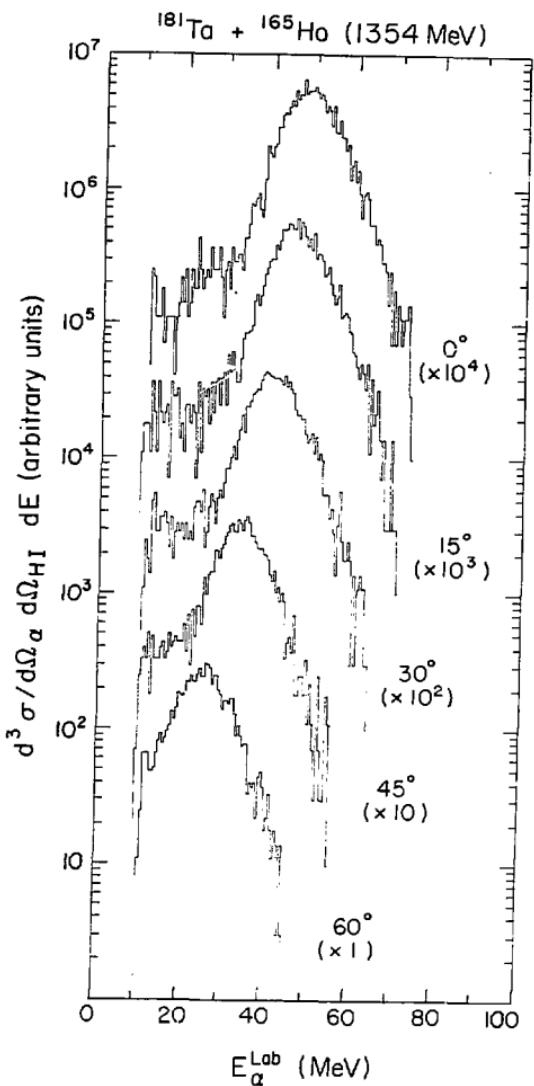
XBL 8110-7355

Fig. V.3

^{181}Ta + ^{165}Ho (1354 MeV)

(a)

(b)
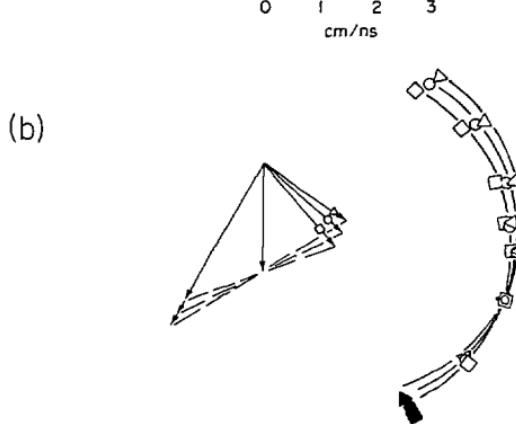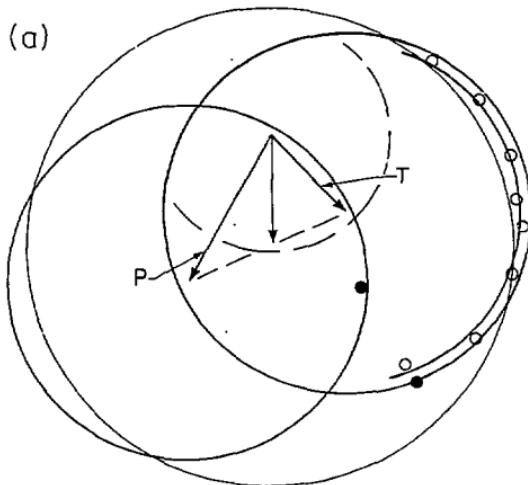
XBL 818-2456A

Fig. V.4
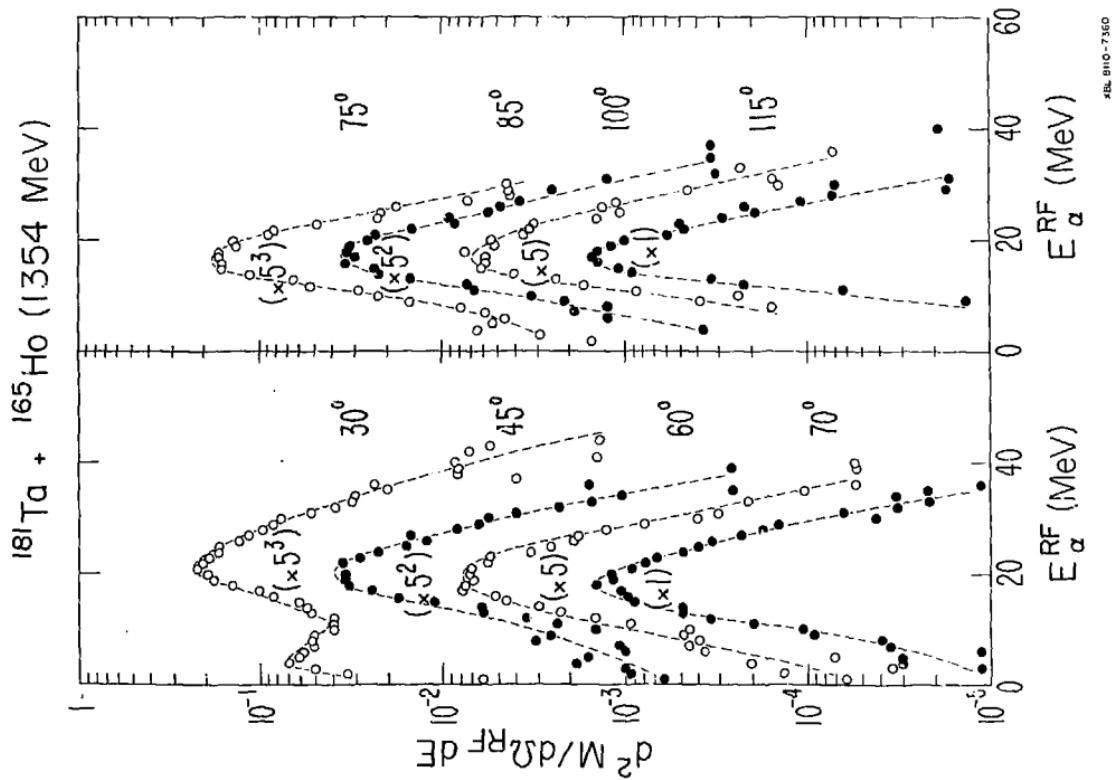
Fig. V.5
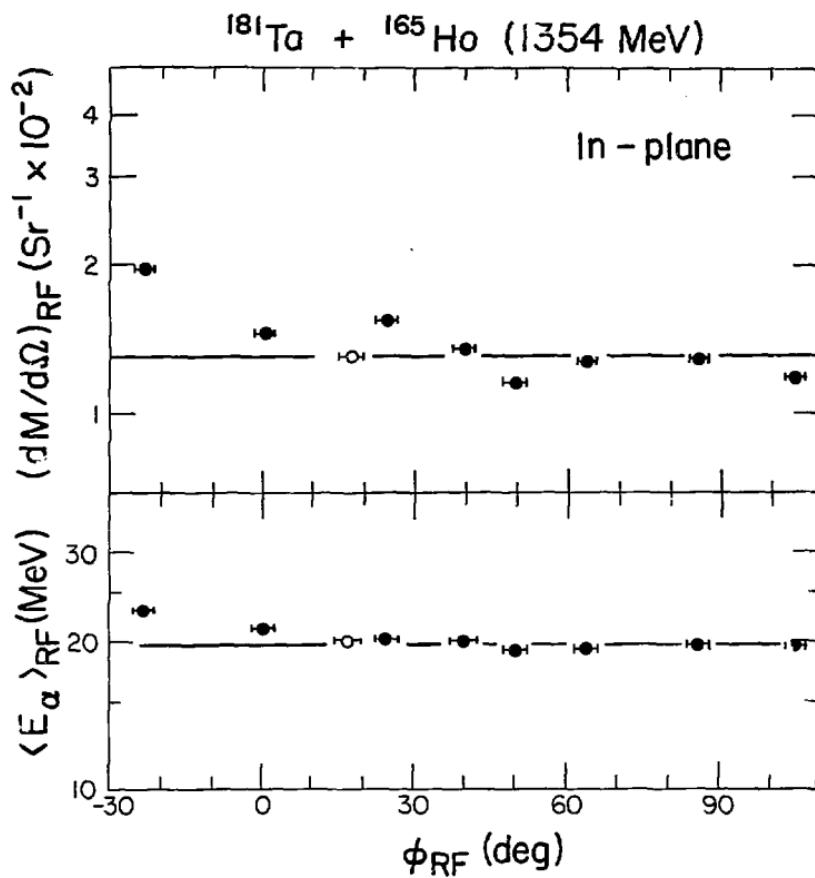
Fig. V.6

$^{nat}Ag + {}^{84}Kr$ (664 MeV)

XBL 8010-2229

Fig. V.7

^{nat}Ag + ^{84}Kr (664 MeV)

$\phi_L = 30°$

$\phi_L = 60°$

$\phi_L = 90°$

a)

b)

Counts

E_α (MeV)

XBL 8010-2230

Fig. V.8
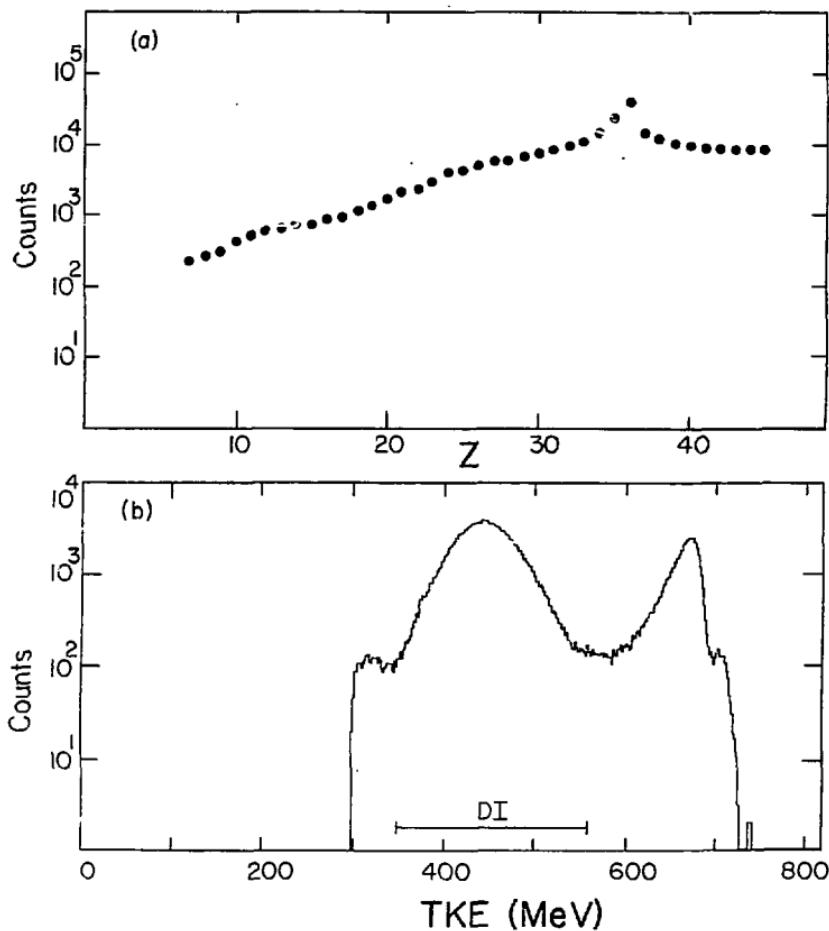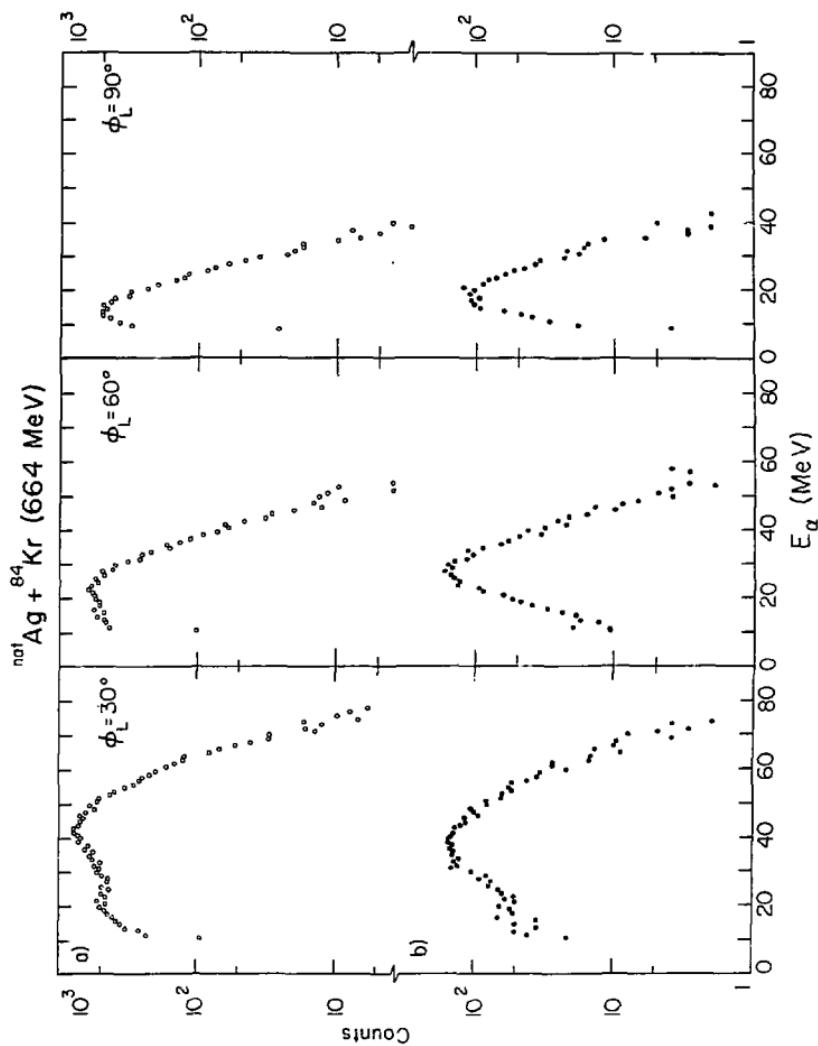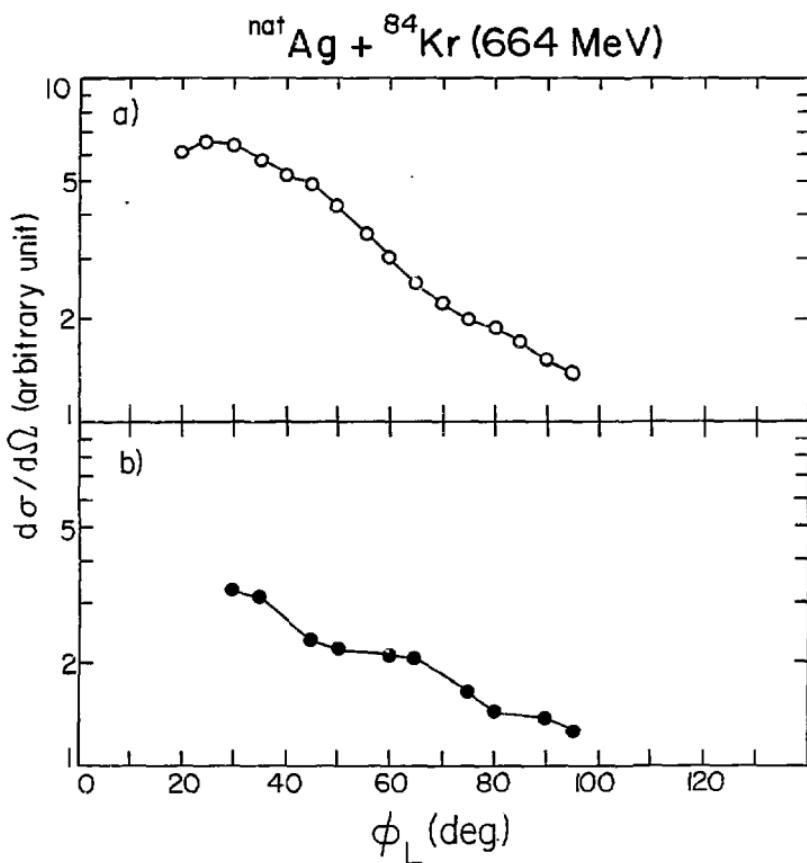
$$^{nat}Ag + {}^{84}Kr \ (664 \ MeV)$$

XBL 8010 - 2231

Fig. V.9

$^{nat}Ag + {}^{84}Kr$ (664 MeV)

0   1   2   3
cm/ns
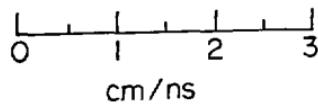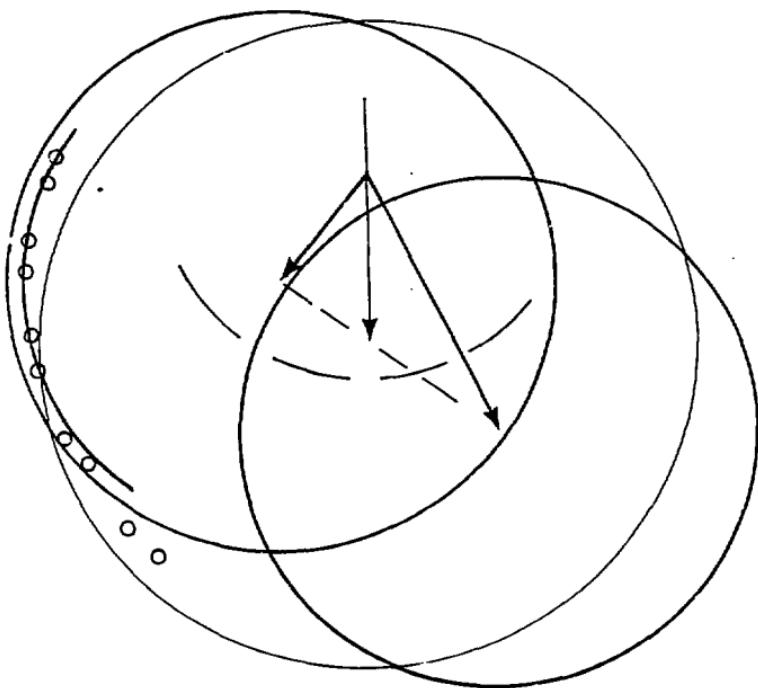
XBL 818 - 2451

Fig. V.10

$^{nat}Ag + ^{84}Kr$ (664 MeV)
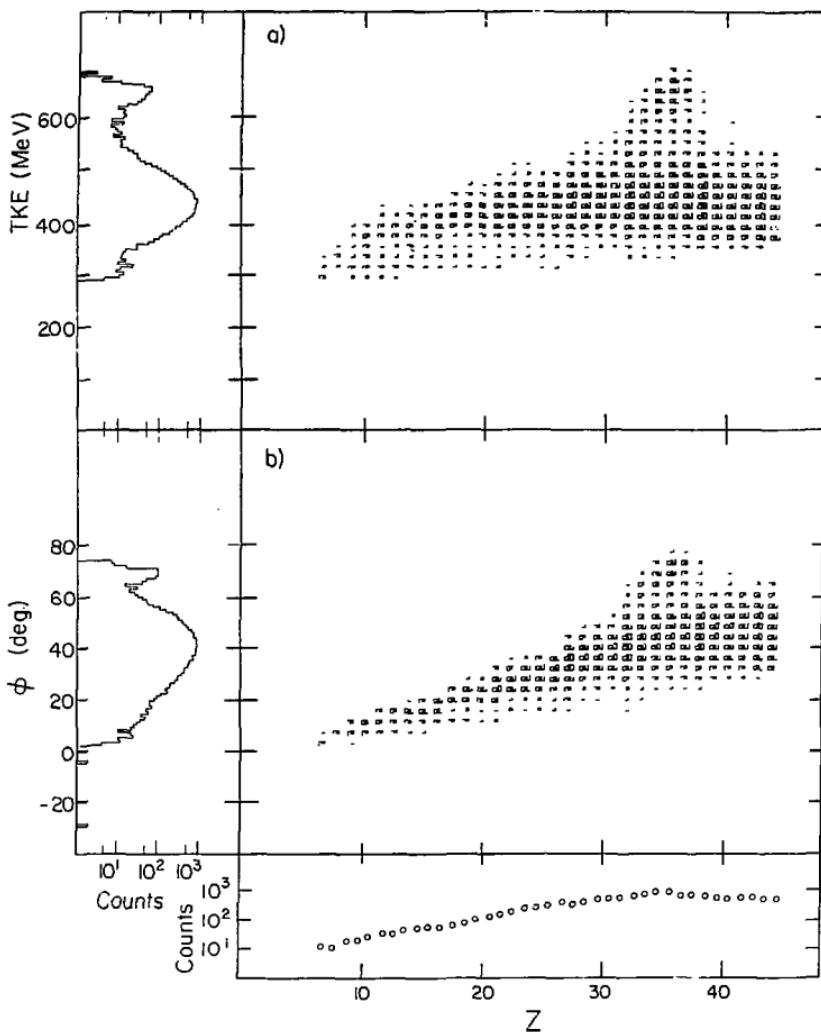
XBL 8010-2234

Fig. V.11
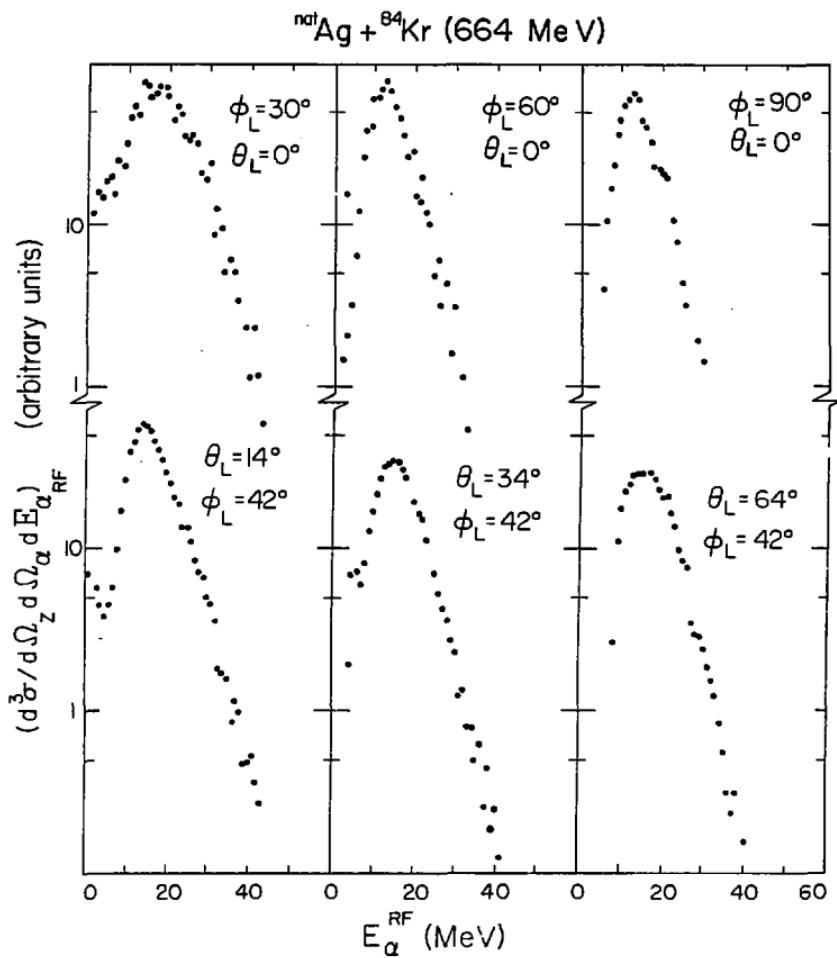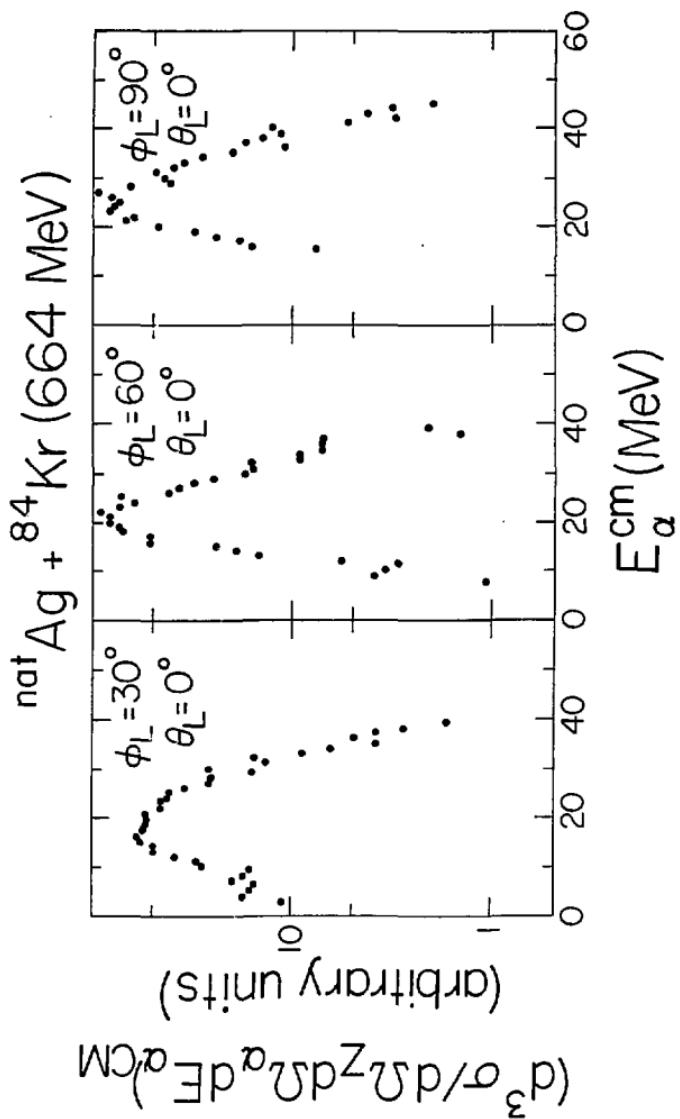
^{nat}Ag + ^{84}Kr (664 MeV)

$\phi_L = 30°$
$\theta_L = 0°$

$\phi_L = 60°$
$\theta_L = 0°$

$\phi_L = 90°$
$\theta_L = 0°$

$\theta_L = 14°$
$\phi_L = 42°$

$\theta_L = 34°$
$\phi_L = 42°$

$\theta_L = 64°$
$\phi_L = 42°$

(arbitrary units)

$\left(d^3\sigma / d\Omega_z \, d\Omega_\alpha \, dE_\alpha \right)_{RF}$

E_α^{RF} (MeV)

XBL 8010-2235

Fig. V.12

$^{nat}Ag + {}^{84}Kr$ (664 MeV)

$\phi_L = 30°$
$\theta_L = 0°$

$\phi_L = 60°$
$\theta_L = 0°$

$\phi_L = 90°$
$\theta_L = 0°$

E_α^{cm} (MeV)

$(d^3\sigma/d\Omega_Z d\Omega_\alpha dE_\alpha)_{CM}$
(arbitrary units)

XBL 811 - 2110

Fig. V.13

Fig. V.14

$^{nat}Ag + {}^{84}Kr$ (664 MeV)

Fig. VI.1

Fig. VI.2

^{181}Ta + ^{165}Ho (1354 MeV)

Out-of-plane distribution

$(dM/d\Omega)_{RF}$ (Sr^{-1} $\times 10^{-2}$)

θ_{RF} (deg)
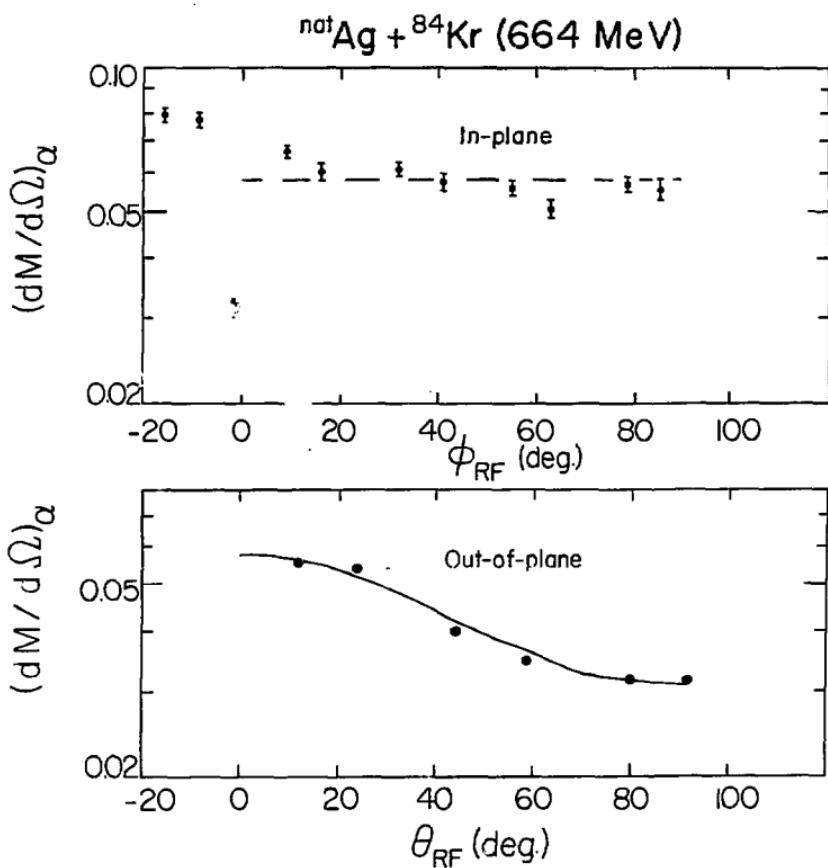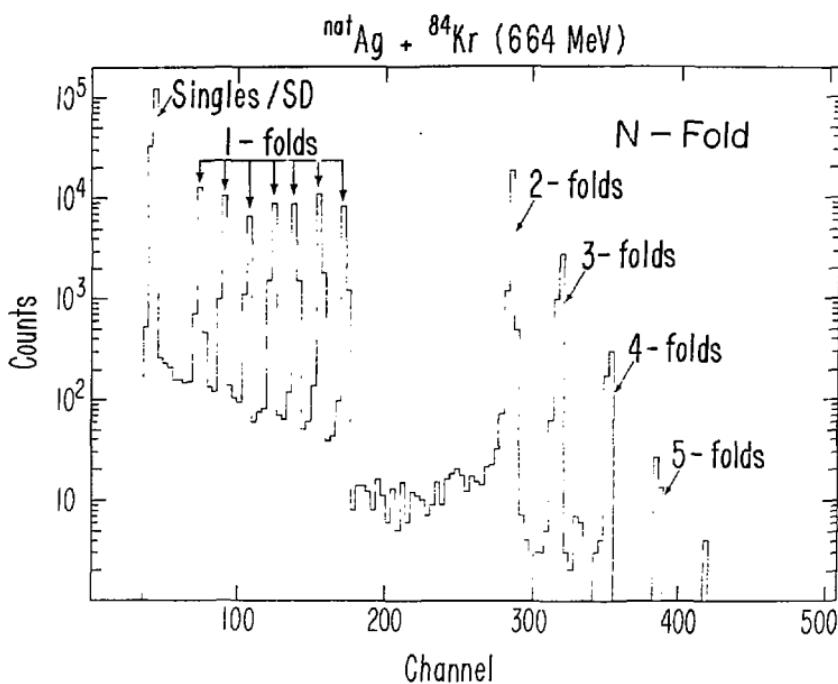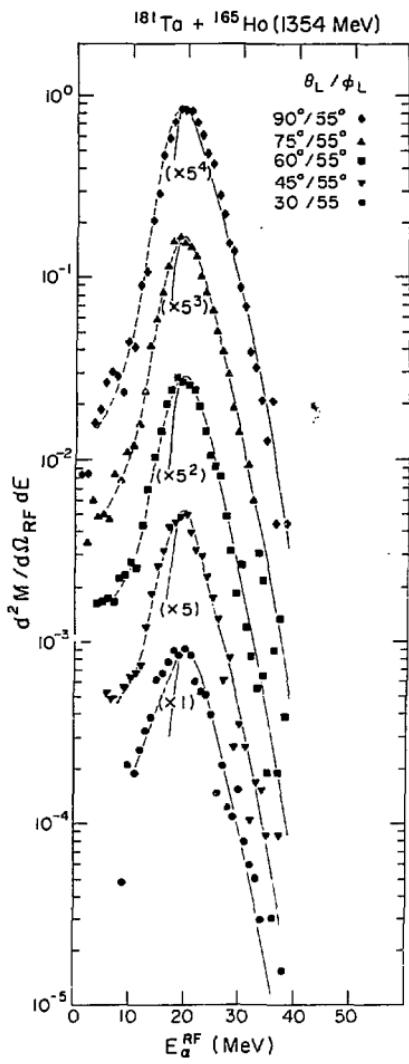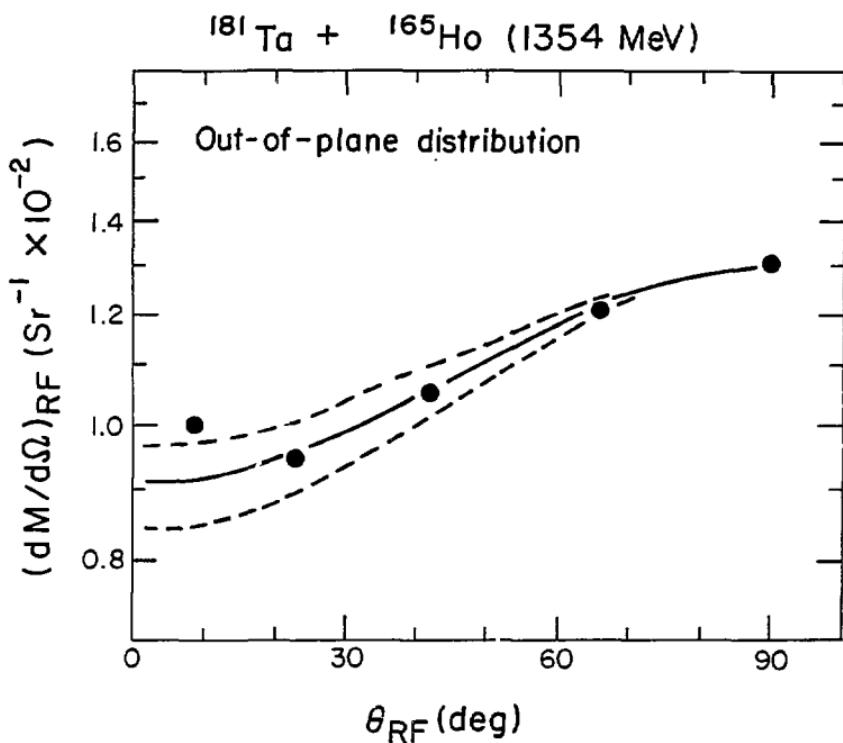
XBL822-4458

Fig. VI.3
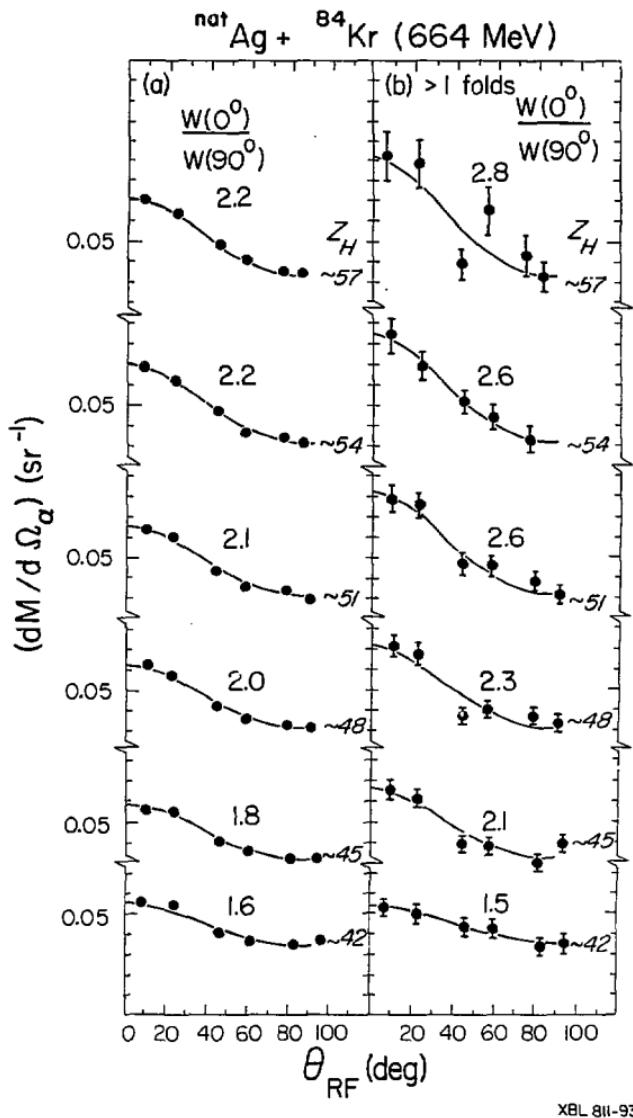
^{nat}Ag + ^{84}Kr (664 MeV)
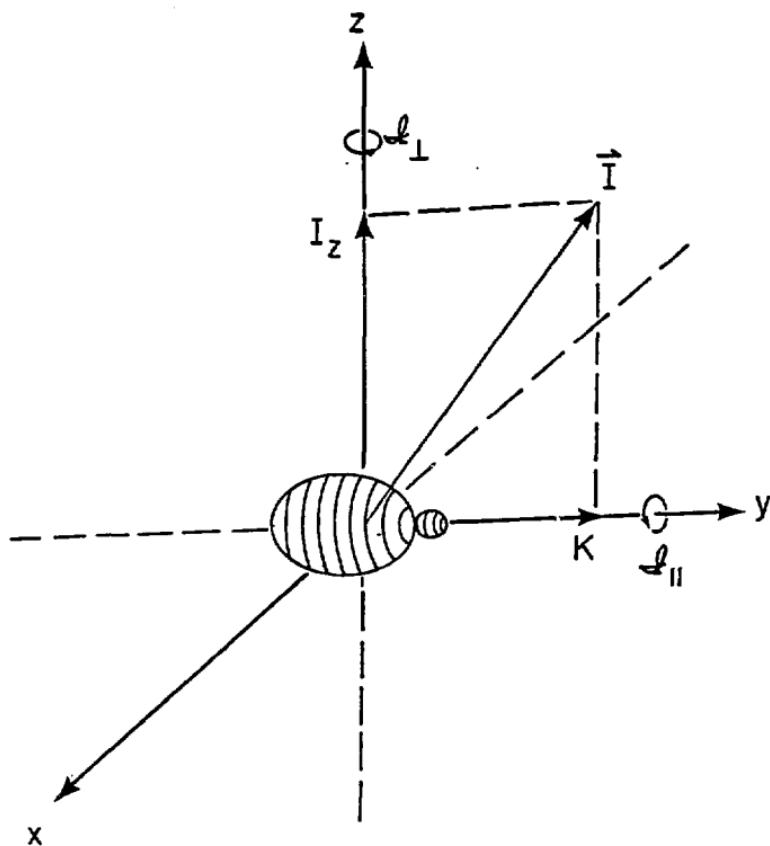
Fig. VI.4

XBL 811-93

XBL 8110-7356

Fig. VI.5
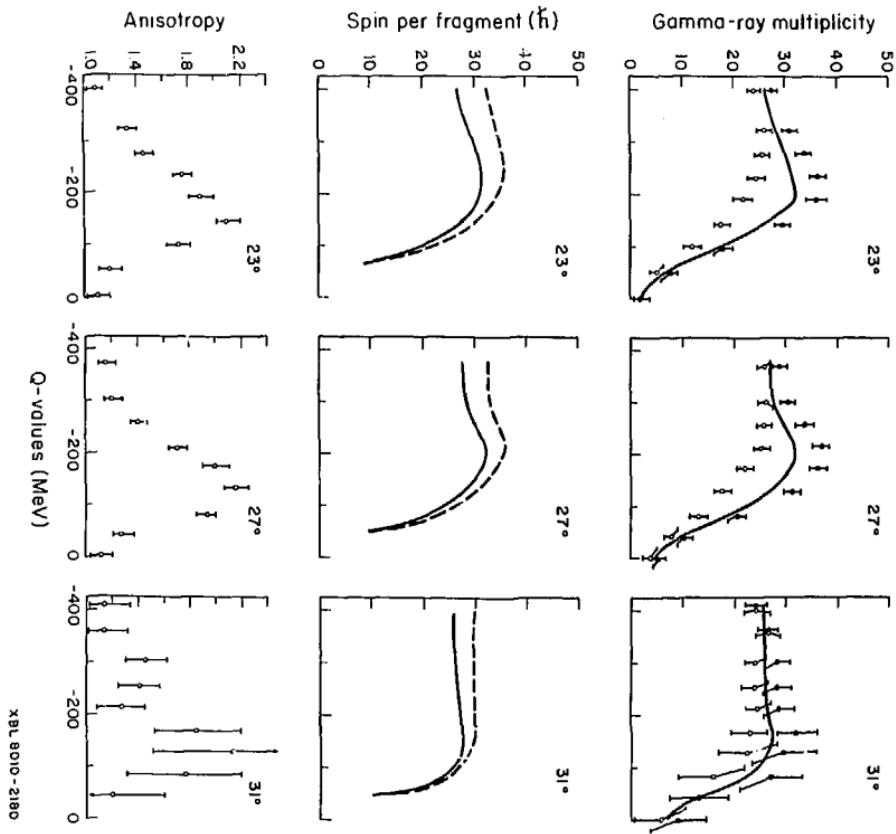
Fig. VI.6

XBL 8010-2180

^{nat}Ag + ^{84}Kr (664 MeV)
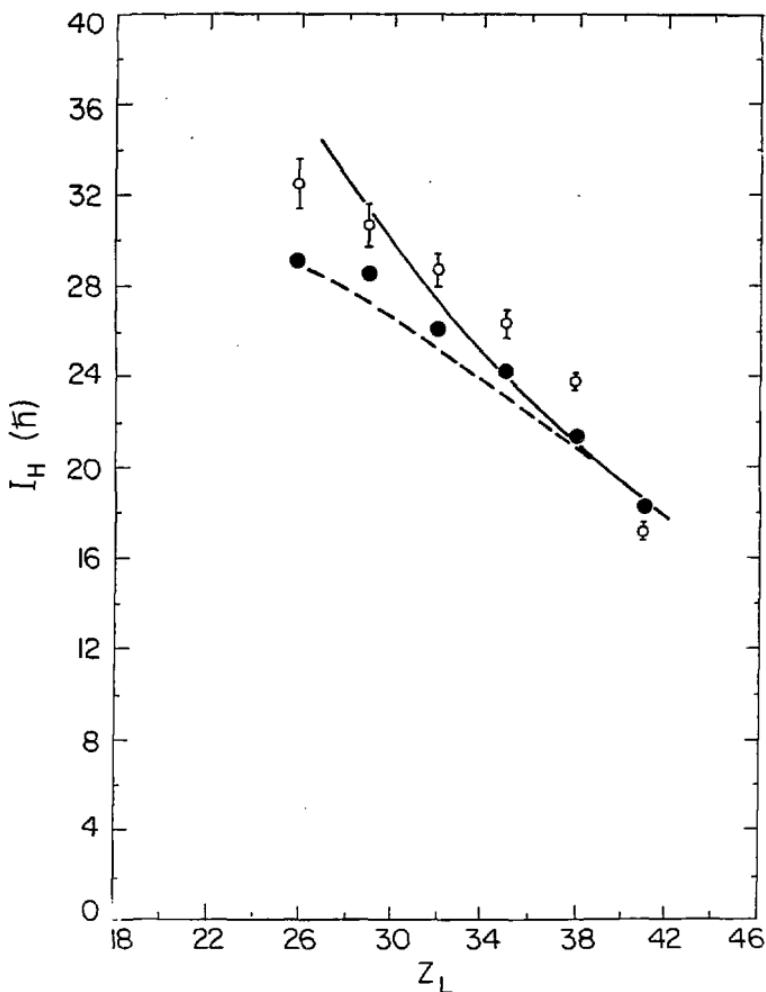
XBL 8010-2228 A

Fig. VI.7
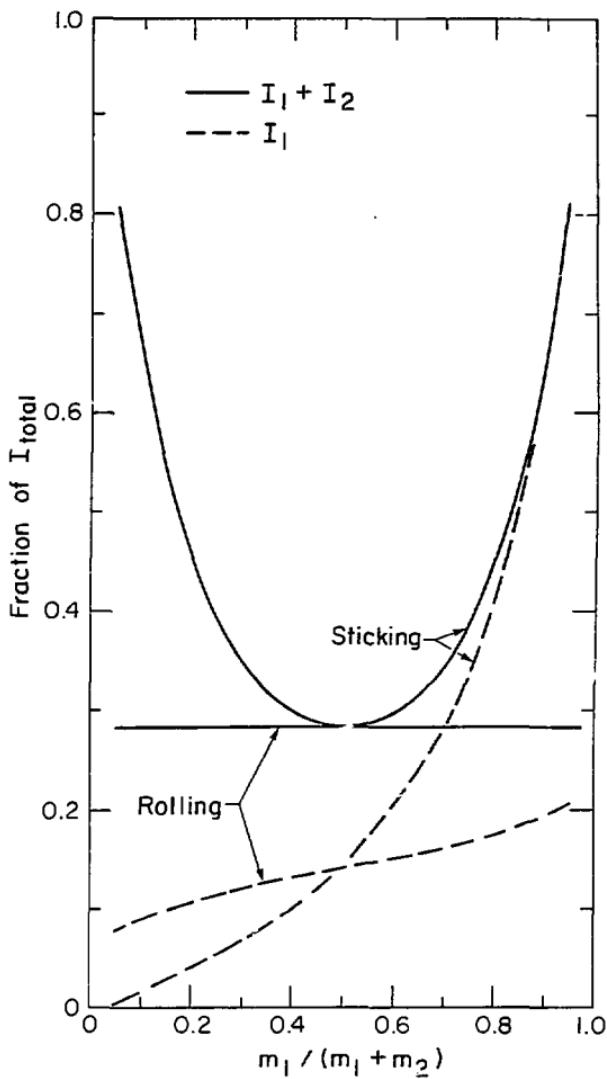
XBL822-4457

Fig. VII.1

Fig. VII.2

XBL 8110-7354

Fig. VII.3

$^{nat}Ag + ^{84}Kr$ (664 MeV)

Fig. VIII.1